Dissertation
submitted to the
Combined Faculties for the Natural Sciences and for Mathematics
of the Ruperto-Carola University of Heidelberg, Germany
for the degree of
Doctor of Natural Sciences

presented by

Master of Science	Maria Danner
born in	Neuhaus am Rennweg
Oral examination:	7th of November 2016

Marker-free T cell phenotyping – towards a label-free diagnostic and prognostic platform

Referees: Prof. Dr. E. Pollerberg

Prof. Dr. J. P. Spatz

List of Abbreviations

APC	allophycocyanin
APCs	antigen-presenting cells
BSA	bovine serum albumin
CCRx	cluster of chemokine receptor
CD-x	cluster of differentiation (surface molecules)
CD25	cluster of differentiation 25, alpha chain of IL-2 receptor, expressed on regulatory T cells and resting memory T cells
CD28	cluster of differentiation 28, receptor providing co-stimulatory signals for T cell activation an survival
CD3	cluster of differentiation 3, subunit of theT cell receptor
CD4	cluster of differentiation 4, MHC Il co-receptor
CD45RA	isoform of cluster of differentiation 45, expressed on naive T cells
CD45RO	isoform of cluster of differentiation 45, expressed on differentiated T cells
CD54	cluster of differentiation 54, also known as LFA-1
CD62L	cluster of differentiation 62L, L-selectin
EDTA	ethylenediaminetetraacetic acid
FACS	fluorescent activating cell sorting
FBS	fetal bovine serum
FITC	fluorescein isothiocyanate
GVHD	Graft-versus-Host-Disease
His6-tag	hexa-histidine tag
ICAM-1	intercellular adhesion molecule 1
IFN-x	interferone (small signalling molecules released by cells)
IKVAV	amino acid sequence: I = isoleucine, K = lysine, V = valine, A = alanine, V = valine
IL-x	interleukin (peptide hormons, class of cytokines)
LFA-1	lymphocyte function associated antigen 1
MHC II	major histocompatibility complex class II
ml	mililiter
NTA	nitrilotriacetic acid
PBMCs	peripheral blood mononuclear cells
PDMS	polydimethylsiloxan
PE	phycoerythrin
PEG	poly(ethylene glycol)
PP	Peyer's Patches (lymphoid nodules in the small intestine)
PS	penicillin/streptomycin

RGD	amino acid sequence: R = arginine, G = glycine, D = aspartate
RICM	reflection interference contrast microscopy
RPMI	roswell park memorial institute medium, medium used for culturing lymhpoide cells
SLO	secondary lymphatic organ (lymph nodes, tonsils, spleen, Peyer's patches
TCL	cytotoxic T cell, also called CD8+ T cell
TCM	central memory T cell
TCR	T cell receptor
TEM	effector memory T cell
TFH	follicular helper T cells
TH	T helper cell, also called CD4+ T cell
TN	naive T cell

Acknowledgments

I thank Professor Dr. J. P. Spatz for giving me the opportunity to work on this interesting and interdisciplinary topic and for supporting me.

I also thank Professor Dr. E. Pollerberg for the fruitfull discussions we had and also for her support.

Special thanks go to Dr. Vera C. Hirschfeld-Warneken for supervising my work. I very much enjoyed the freedom she gave me during my PhD and I thank her for taking time for discussing my work.

I also thank Katja Ottmüller from our cooperation group for teaching me a lot about T cells. I very much appreciated working with her on a shared project and discussing our work. I also thank her for welcoming me at her institute and for introducing me to “her side” of the project.

I want to thank Dr. Seraphine Wegner and Franziska Schenk for giving me great advice, especially during the development of the functionalization approach, and also for the provision of chemicals. Many thanks to Dr. Tamás Haraszti for helping me with SEM and AFM measurements, and for always being available and very helpful when technical problems with the RICM occurred. I also thank him for helping me with my evaluation scripts and giving me new ideas about programming and problem solving. Also, I thank Dr. Rebecca Medda for answering every question I had regarding cell culture, and I thank her for her support in the lab and during the RICM measurements. I also thank Dr. Timo Maier for introducing me into RICM and teaching me the basics about fractal analysis.

Thanks also to Dr. Judit Guasch for showing me how to isolate $CD4^+$ T cells and for discussing my results. Many thanks also to Dr. Monika Langlotz from the FACS facility, who taught me how to do FACS measurements. I very much appreciated her advice while planning my experiments.

I also thank Martin Schröter and Isabelle Kirst, who have done an internship during their Master studies, for their work. I very much enjoyed supervising them and I very much appreciated their working attitude and ideas they had.

I also thank everyone from the “Spatz group” for the warm and welcoming working atmosphere, for helping each other and being supportive in others’ problems and challenges.

Last but not least, I want to thank my husband Simon Danner for all the support he gave me during my PhD.

Table of Contents

1 Summary

T cells are one of the key players in cell-mediated immunity. The peripheral blood consists of an intricate balance between various T cell subpopulations, which vary in their differentiation state and memory potential. Many of these T cell subpopulations are associated with diseases, and numerous studies highlight the importance of monitoring the frequencies of T cell subsets in peripheral blood for determining the immune competence status of a person. Particularly elderly persons show a wide spectrum of immunosenescence stages that need to be taken into account in targeted medicine.

Methods that are used up to date to identify T cell subsets are based on the expression of an enormous and increasing number of surface markers that depend on cells' differentiation and activation state. This is often insufficient since T cells display a great variety of differentiation states.

In this thesis, a novel marker-free, fast and low-cost approach for T cell subpopulation identification is presented that is based on changes in adhesion- and migration-related parameters during T cell differentiation. We hypothesized that these fine phenotype shifts can be visualized with Reflection Interference Contrast Microscopy (RICM) imaging and suffice to allow clear classification of T cell subpopulations.

To first prove the sensitivity of our approach we imaged $CD4^+$ T cells isolated from human peripheral blood at different time points during *in vitro* differentiation. Several morphological parameters correlated with memory T cell marker expression and were distinct from less differentiated states, e.g. an increased fractal dimension (Df) parameter that describes the cell´s membrane topology or increased projected and adhesion cell area.

In a next step we determined adhesion parameters and fractal dimensions from RICM images of T cell subsets that were differentiated *in vivo*. We separated naïve, central memory and effector memory $CD4^+$ T cells from human $CD4^+$ populations. For all determined parameters, naïve T cells showed significant lower values compared to memory cells. Using principal component analysis, the parameters that described the data variance of subsets best were identified to be area, adhesive area, excess perimeter and fractal dimension of contour/topology. These parameters were then used for generating cluster centres for each subpopulation with k-mean clustering. T cell subsets isolated from three different donors were then designated to these clustering points. With this approach, 80 % of T cells were assigned to their correct subtype.

In accordance to *in vitro* differentiation experiments, we found an increase in the complexity of membrane topology and an increase in cell area from naïve to central memory and to effector memory cells. These results suggest that all differentiation states of T cells may be continuously represented in adhesion maps. This visualisation approach will allow including T cell subsets that cannot be considered by conventional surface marker sets but are highly representative for distinct immune competence states.

To apply our concepts of a marker-free adhesion-based assay to discriminate between a healthy $CD4^+$ T cell "fingerprint" and one in disease state, we used an *in vitro* Graft-versus-Host-Disease (GVHD) murine model. In this approach we did not evaluate adhesion properties on static RICM images but tracked adhesion-dependent intestine T cell homing on migration chips. For this, the chemokine CCL25 was anchored to 2D gold nanoparticle distance gradients and ICAM-1 was covalently linked to functional PEG molecules in between. $CD4^+$ T cells with a GVHD phenotype were able to respond to decreasing CCL25 distances by increasing cell velocity, which was not observed for control $CD4^+$ T cells from healthy mice. Furthermore, GVHD phenotype $CD4^+$ T cells displayed a lower degree of complexity of cell trajectories than control cells.

Our approaches of imaging T cell adhesion and/or *in vitro* homing is very promising for future marker-free immunodiagnostics that read out the immune competence status of a patient within short time, which can be applied in therapy monitoring and advising primary personalised treatment.

2 Zusammenfassung

T-Zellen spielen eine zentrale Rolle in zellvermittelten Immunreaktionen. Im peripheren Blut sind verschiedene T-Zellsubpopulationen vertreten, welche sich in ihrem Differenzierungs- und Gedächtnis-Potential unterscheiden. Viele dieser Subpopulationen sind mit Krankheiten assoziiert. Außerdem geben die Häufigkeiten der T-Zellsubpopulationen im peripheren Blut Aufschluss über die Immunkompetenz von Patienten. Insbesondere ältere Personen weisen ein weit gefächertes Spektrum von Immunseneszenz auf, was in der gezielten medizinischen Behandlung berücksichtigt werden muss.

Heutige Methoden zur Identifizierung von T-Zellsubpopulationen basieren weitestgehend auf der Analyse von Oberflächenmarkern, deren Expression von den Differenzierungs- und Aktivierungsstadien der Zellen abhängig ist. Diese Methoden stellen oftmals eine große Herausforderung dar, da T-Zellen eine große Bandbreite an Differenzierungsgraden aufweisen und die benötigte Zahl der zu analysierenden Marker unüberschaubar ansteigt.

In dieser Arbeit wird eine neue markerfreie, schnelle und kostengünstige Methode zur Identifizierung von T-Zellsubpopulationen präsentiert, welche auf Veränderungen von adhäsions- und migrationsbezogenen Parametern während der Differenzierung von T-Zellen basiert. Die Hypothese wurde aufgestellt, dass diese geringen phänotypischen Änderungen mithilfe Referenz-Interferenz-Kontrast-Mikroskopie (RICM) visualisiert werden können, was ausreichend ist zur eindeutigen Klassifizierung von T-Zellsubpopulationen.

Um die Sensitivität unseres Ansatzes zu beweisen, wurden $CD4^+$ T-Zellen aus humanem peripheren Blut isoliert, *in vitro* differenziert und RICM-Bilder zu verschiedenen Zeitpunkten aufgenommen. Die erhöhte Expression von Gedächtnismarkern spiegelte sich in mehreren Morphologieparametern wider, wie z.B. in einer erhöhten fraktale Dimension, welche die Membrantopologie von Zellen beschreibt, oder in einer erhöhten projizierten Zellfläche und Adhäsionsfläche.

Im nächsten Schritt wurden Adhäsionsparameter und fraktale Dimensionen von *in vivo* differenzierten T-Zellen bestimmt. Hierfür wurden humane $CD4^+$ T-Zellen in naive, Effektor-Gedächtnis-T-Zellen und zentrale Gedächtnis-T-Zellen separiert. Für alle ermittelten Parameter wiesen naive T-Zellen im Vergleich zu Gedächtniszellen signifikant

niedrigere Werte auf. Mit Hauptkomponentenanalyse wurden die Parameter identifiziert, welche die Datenvarianz am besten erfassen konnten. Diese waren Zellfläche, Adhäsionsfläche, Überschussperimeter und fraktale Dimension der Kontur und Topologie, welche anschließend zur Berechnung von Clusterpunkten für jede Subpopulation durch K-mean-clustering verwendet wurden. Anhand dieser Clusterpunkte wurden anschließend T-Zellen von drei verschiedenen Spendern klassifiziert. Mit diesem Ansatz gelang es uns, 80 % der T-Zellen ihrer richtigen T-Zellsubpopulation zuzuordnen.

In Übereinstimmung mit unseren *in vitro* Differenzierungsexperimenten wurden eine erhöhte Komplexität der Membrantopologie und eine erhöhte Zellfläche von naiven zu Zentral- und Effektor-Gedächtnis-T-Zellen gefunden. Diese Ergebnisse legen nahe, dass alle Differenzierungsgrade von T-Zellen kontinuierlich in Adhäsionskarten dargestellt werden können. Diese Visualisierungsmethode ermöglicht es T-Zellsubpopulationen einzuschließen, welche mithilfe gängiger Oberflächenmarker nicht erfasst werden können, die jedoch sehr repräsentativ für bestimmte Immunkompetenzstadien sind.

Um unsere Konzepte der markerfreien adhäsionsbasierten Analysen zu Unterscheidung zwischen gesunden und kranken $CD4^+$ T-Zell „Fingerabdrücken“ anzuwenden, wurde hier ein *in vitro* Graft-versus-Host-Disease (GVHD) Mausmodell eingesetzt. Hierbei wurden nicht die Adhäsionseigenschaften von statischen RICM-Bildern analysiert, sondern die adhäsionsabhängige Migration von T-Zellen auf Migrations-Chips untersucht. Dazu wurde das darm-spezifische Chemokin CCL25 auf 2D Abstandsgradienten von Goldnanopartikeln verankert und ICAM-1 wurde kovalent über funktionelles PEG an die Zwischenräume gebunden. $CD4^+$ T-Zellen mit einem GVHD Phänotyp reagierten auf erhöhte CCL25-Präsentation mit erhöhter Migrationsgeschwindigkeit, während dies bei gesunden Kontrollzellen nicht beobachtet wurde. Zudem wiesen die Trajektorien der Zellen mit dem GVHD Phänotyp eine geringere Komplexität auf als die der Kontrollzellen.

Unsere Ansätze zur Abbildung von T-Zell-Adhäsion und/oder *in vitro* -Migration sind vielversprechend für zukünftige markerfreie Immundiagnostiken, welche innerhalb kürzester Zeit den Immunkompetenzstatus eines Patienten ermitteln und in der Überwachung von Therapien oder der Planung personalisierter Behandlungen eingesetzt werden können.

3 Introduction

Our bodies are constantly exposed to pathogens that are present in the environment. Protection from these infectious agents largely results from the coordinated and highly complex interaction of cells and molecules of the mammalian immune system. One of the key cellular components of the adaptive immune system are T lymphocytes.

T lymphocytes can be divided into helper T cells (CD4$^+$ T cells) and cytotoxic T cells (CD8$^+$ T cells). The latter are responsible for destroying host cells infected with intracellular pathogens. CD4$^+$ T cells aid other immune cells in their immune response, e.g. by secreting molecules that promote B cell maturation or activation of cytotoxic T cells and macrophages. Besides, they are essential in maintaining self-tolerance by inhibiting immune reactions that could damage the host. This is of special importance during long-term antigen exposure. CD4$^+$ T cells therefore play an essential role in adaptive immunity (Murphy, 2011).

A fundamental feature of T cell mediated immunity is the ability of antigen inexperienced (naïve) T cells to become activated upon antigen recognition and undergo a program of proliferation and functional differentiation. This results in a large pool of effector and memory cells. Many of these cells enter the blood and migrate into tissues, where they control and eventually clear the infection. Subsequently, many of these cells die, but some subtypes that have the ability to create immunological memory remain. Compared to naïve T cells, memory cells produce a greater variety of immune molecules and in larger quantities, and they can respond to re-infection without further differentiation. A dynamic reservoir of these antigen-experienced memory T cells accumulates over the lifetime of an individual and ensures rapid response and protection upon re-infection (Murphy, 2011; Russ, Prier, Rao, & Turner, 2013).

Two main subsets of circulating memory T cells exist that can be distinguished by their effector function, proliferation capacity and migration potential.

Central memory T cells (T_{CM}) have no or little effector function but proliferate extensively (Cyster, 1999). Also, they give stimulatory feedback to other immune cells and therefore promote immune responses. Effector memory T cells (T_{EM}) have little proliferation capacities but immediate effector functions. They express distinct chemokine receptors and adhesion molecules that enable them to migrate into inflamed tissues (Sallusto, Geginat, & Lanzavecchia, 2004).

Thus, the peripheral blood comprises circulating T lymphocytes that vary in their activation and differentiation states and also in their effector and memory status. Each T cell subset fulfils specific tasks and is essential for T cell mediated immunity.

The composition of circulating T cell subpopulation is dependent on age and acute pathogen exposure and is therefore correlated with the immune status of an individual (Gabriel, Schmitt, & Kindermann, 1993; Pepper & Jenkins, 2011). During the last years, T cell subpopulations have also been associated with various diseases, and an increasing number of studies highlight the importance of monitoring the frequencies of T cell subsets in peripheral blood during infection and treatment.

For example, Magenau et al. identified the frequency of regulatory T cells as a potential biomarker for diagnosis and prognosis of acute Graft-versus-Host-Disease (GVHD) (Magenau et al., 2010). Also, the percentage of T_{EM} in peripheral blood correlates with the severity of this disease (Yamashita, 2004) and patients that received organ transplants show altered ratios of T_{EM} to T_{CM} (Segundo et al., 2010). Peguillet et al. found that frequencies of differentiated effector $CD4^+$ T cells correlates with tumor size regression during chemotherapy (Peguillet et al., 2014), and the frequency circulating T_{EM} cells isassociated with atherosclerosis and coronary artery disease (Ammirati et al., 2012). Also, the number of distinct T cell subsets in peripheral blood increases during bacterial or viral infection (Nair et al., 2011; Wagner et al., 2008).

Therefore, monitoring T cell subsets in patients' blood is a highly promising tool for determining the immune competence status of a person and the severity of diseases. Furthermore, observing the alterations of T cell frequencies has great potential for monitoring the success of therapies and therefore leads the way to highly effective, targeted and personalized medicine.

Up to date, the conventional method used to identify T cell subsets is flow cytometry. It employs fluorescent antibody labelling of surface molecules that are differentially expressed on T cells, depending on their differentiation and activation state. This approach of phenotypic characterisation displays difficulties and experimental challenges, e.g. many surface molecules need to be analysed in order to accurately assign T cells to their specific subset (Okada, Kondo, Matsuki, Takata, & Takiguchi, 2008). Additionally, fluorophore instability, bleaching and phototoxicity may lead to false results. Furthermore, expression of surface markers is often very heterogeneous within a T cell population (Chao, Jensen, &

Dailey, 1997; Kishimoto & Jutila, 1990; Sallusto et al., 2004), and stages of intermediate differentiation stages can therefore not be recorded. This method is therefore very laborious for e.g. determining immunosenescence states (Aw, Silva, & Palmer, 2007; Goronzy & Weyand, 2013). Another challenge displays T cell exhaustion, which occurs during high-grade chronic infections and gradually leads to functional unresponsiveness of cells, whereas their effector phenotype remains (Wherry, 2011; Yi, Cox, & Zajac, 2010). Due to these reasons, accurate T cell phenotyping with flow cytometry is often inaccurate, labour-intensive, time-consuming and costly.

To overcome the drawn-backs of this method more and more work is currently put into the development of marker free cell phenotyping.

Some published work is based on spectroscopic analysis of cells, e.g. Raman spectroscopy that was used for discriminating between neural and invading glioblastoma cells (Koch et al., 2013) or FTIR, which was used to identify and distinguish B and T cells as well as for detecting lymphocyte activation (Krafft, Salzer, Soff, & Meyer-Hermann, 2005) (Wood, Tait, & McNaughton, 2000).

Other techniques use distinct physical properties of cells as parameters for phenotyping. For example, real-time deformability cytometry was employed for mechanical phenotyping of human hematopoietic stem cells and progenitor cells (Jacobi et al., n.d.; Otto et al., 2015), and a microfluidic approach was used to isolate rare circulating tumor cells from blood samples (Karabacak et al., 2014).

Other methods that do not require costly equipment and experimental setup as the above-mentioned examples have also been presented in the last years. Klein et al. used fractal analysis for marker-free phenotyping of tumor cells (Klein, Maier, Hirschfeld-Warneken, & Spatz, 2013), and Sekhavati et al. monitored the differentiation of hematopoietic progenitor cells by Brownian motion analysis from phase-contrast time-lapse images (Sekhavati et al., 2015).

These and other approaches aim to improve conventional cell phenotyping techniques in order to realize them in large-scale clinical settings. To our knowledge, none of these methods focus on marker-free identification of T cell subsets. Thus, an improvement in T cell subpopulations identification is needed since these cells have great implications in health and disease. In this study, we therefore aim to establish a method for T cell phenotyping that is marker-free, fast and of low cost.

Our approach is based on the fact that T cell subpopulations exhibit different degrees of effector status and differentiation. These are reflected in cells' phenotype, e.g. in altered proliferation capacities, cytokine production and plasticity. We hypothesize that these changes affect morphological parameters of cells, such as structure of cell membrane, adhesion patterns and migration characteristics, which contain sufficient information for marker-free T cell subset identification (Figure 1).

In the first part of this thesis, we extract adhesion parameters and fractal dimensions of T cells from Reflection Interference Contrast Microscopy (RICM) images. This technique resolves ultrafine cell outlines and reveals cells' adhesion topologies that are expected to reflect their differentiation states. To prove the sensitivity of our approach, we investigate how these morphologic parameters change during *in vitro* differentiation of human CD4$^+$ T cells. In a next step, we determine how these parameters vary between conventional T cell subpopulations that have differentiated *in vivo* and whether they are suitable for T cell subset identification.

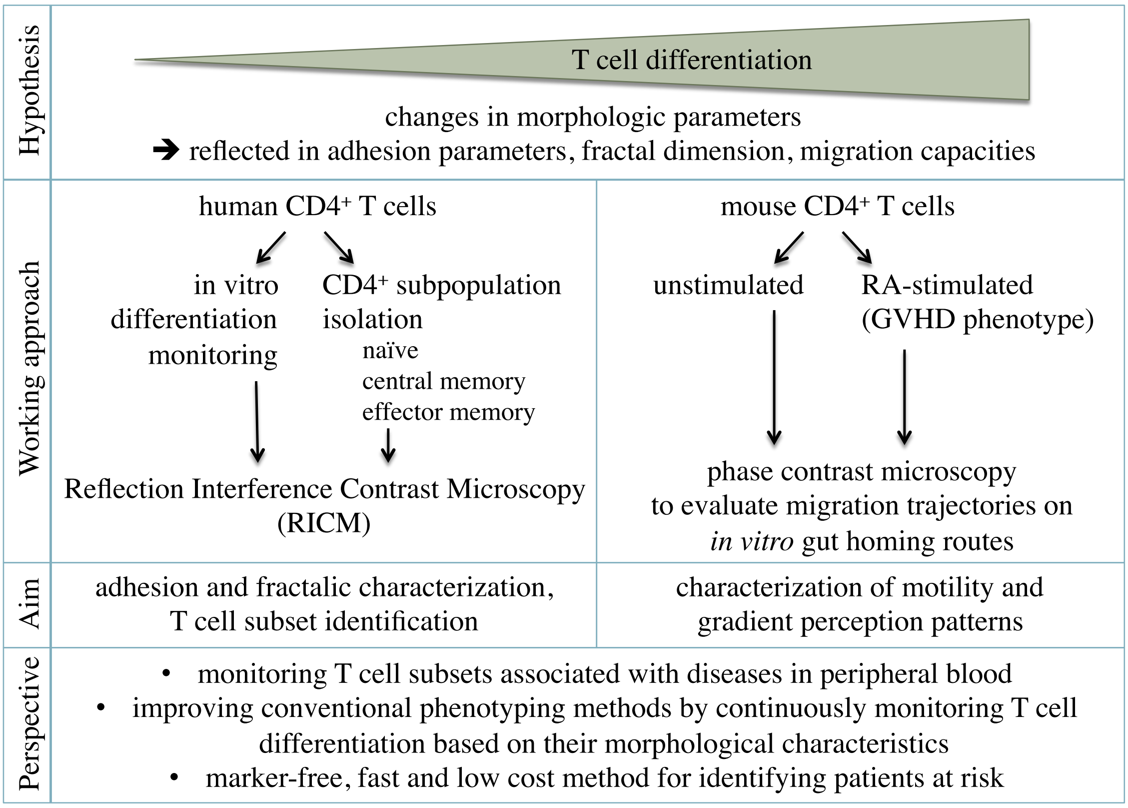

Figure 1 Marker-free T cell phenotyping: hypothesis, working approach, aim and perspective of this thesis.

According to our hypothesis, T cell differentiation and therefore their effector function is also reflected in their migratory behaviour, since T cell subsets have distinct abilities to respond to chemokines and chemokine gradients that enable them to invade into inflamed tissues (Mora & Andrian, 2006). We therefore expect that changes in the migration pattern of mixed CD4$^+$ T cell populations reveal alterations in subset composition, which could result from an infection or inflammatory disease. To discriminate between a healthy CD4$^+$ T cell "fingerprint" and one in disease state, we here use a murine *in vitro* Graft-versus-Host-Disease (GVHD) model.

In the second part of this thesis, we therefore fabricate migration chips that mimic native homing routes to the small intestine, which is one of the main manifestation sites for tissue damage in GVHD (Shlomchik, 2007)3. CD4$^+$ T cells isolated from mice are then seeded on these *in vitro* homing routes and their ability to respond to presented chemokines and recognize chemokine gradients is evaluated. Comparing these results with CD4$^+$ T cells possessing a GVHD phenotype will reveal migration patterns that can be correlated with diseases.

The approach presented here leads the way to identifying T cell subsets by their adhesion, fractalic and migratory signatures that reflect their differentiation states and that are correlated with their functional properties. In the future, our method can be used for generating adhesion maps that allow determining the constitution of T cell subpopulations in peripheral blood. These adhesion maps are also highly promising for identifying T cell subsets of intermediate differentiation states that cannot be accounted for with conventional phenotyping methods but are highly representative for distinct immune competence states or disease severity (Peguillet et al., 2014). Interpreting patterns of T cell distributions has therefore high potential for being applied in clinical settings for diagnosis and therapy monitoring of a variety of diseases that are associated with changes in T cell subset composition.

4 Theoretical Background

4.1 T cells

T cells or T lymphocytes are a type of white blood cells that are essential in cell-mediated immunity. They mature in the thymus and circulate through the body, searching for their cognate antigen, e.g. viral or bacterial structures, presented by other cells. Various signals lead to T cell activation, differentiation and proliferation into various types of effector and memory cells. After the infection is cleared, most lymphocytes die, but some subtypes that have the ability to create immunological memory remain. The memory T cell pool ensures a fast and targeted immune response upon re-infection. It is a dynamic reservoir of antigen-experienced T lymphocytes that accumulate over the lifetime of an individual (Murphy, 2011).

Two main types of conventional T cells[1] exist: T helper (T_H) cells and cytotoxic T cells (TCLs). TCLs are responsible for destroying cells infected with intracellular pathogens, e.g. viruses, and tumor cells. They express the surface molecule CD8 and are therefore called $CD8^+$ T cells. T_H cells express CD4, are known as $CD4^+$ T cells and aid other white blood cells in their immune response, e.g. by B cell maturation or activation of TCLs and macrophages. Besides, they are required to maintain self-tolerance and inhibit immune reactions that could damage the host. They therefore play an essential role in adaptive immunity (Seder & Ahmed, 2003).

The focus of this thesis lies on $CD4^+$ T cells, since many subtypes have been identified in being involved in various diseases and are therefore potential markers for therapy monitoring. The content of the following chapter therefore focuses on T_H cells, but many concepts can also be applied to $CD8^+$ T cells.

---

[1] Conventional T cells express an $\alpha\beta$ T cell receptor (TCR). Unconventional T cells express a $\gamma\delta$ TCR and reside in epithelial environments where they recognise infectious agents and cancer cells and regulate inflammatory responses. Other unconventional T cells are natural killer T (NKT) cells that play a role in allergy, autoimmunity and defense against infection and cancer.

4.1.1 T cell activation and differentiation

Once T cells have completed their maturation in the thymus, they enter the bloodstream. When they reach a peripheral lymphoid organ, they leave the blood circulation and migrate through the lymphoid tissue, and return through the lymphatics to the bloodstream. By this circulation between blood and lymphoid tissues they search for their specific antigen. The T cell response is initiated in T cell areas of secondary lymphatic organs (SLOs) where they encounter antigen-loaded dendritic cells and co-stimulatory signals. They then proliferate and differentiate into effector cells that help to clear the pathogen by acting on other host cells. These cells can also enter the circulatory systems and are able to migrate into infected tissues. At the same time, memory T cells are generated (Murphy, 2011).

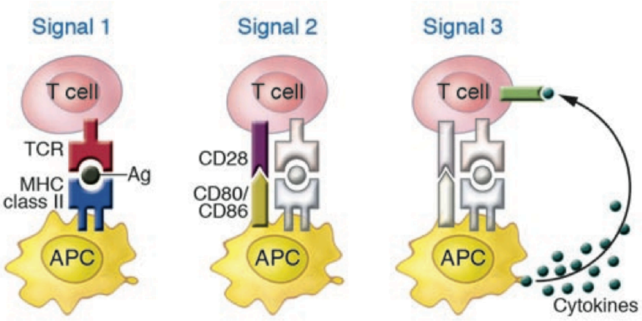

Figure 2 Antigen-specific CD4$^+$ T cell activation depends on three signals. The first signal results from binding of the T cell receptor (TCR) to the matching antigen (Ag) presented on MHC class II molecules on an antigen-presenting cell (APC). Co-stimulatory molecules cause signal 2, which also includes stabilization of the formed immune synapse by adhesion molecules, whereas other molecules generate inhibitory signals (not shown). Signal 3 results from the secretion of cytokines by APCs that lead to lineage-specific differentiation of T cells into various types of subsets. (image: (Gutcher & Becher, 2007))

Differentiation of CD4$^+$ T cells into effector and memory cells is based on three signals that the cells encounter during an infection (Figure 2).

The first signal is derived from binding of the T cell receptor (TCR) to complexes of the foreign peptide and major histocompatibility complex class II (MHC II) on antigen-presenting cells (APCs) in SLOs. Thanks to their large TCR repertoire T cells are potentially able to recognize the whole spectrum of presented antigens. As a second signal, APCs generate co-stimulatory signals, such as binding of APCs' cell-surface protein CD80 and CD86 to the surface receptor CD28 of T cells. This event triggers the naïve cell to divide and become effector lymphocytes (Pepper & Jenkins, 2011)

Naïve CD4$^+$ T cells differentiate into many T helper cell subsets, depending on the cytokines secreted by APCs, e.g. IL-12 leads to T$_H$1 cells or IL-4 to T$_H$2 cells. This is the third signal T cells encounter (Gutcher & Becher, 2007).

Up to date, five principal helper T cell subsets have been identified (Figure 3). T$_H$1 and T$_H$2 cell immune response target intracellular and extracellular pathogens, respectively. T$_H$17 cells are responsible for generating acute inflammation at sites of infection by recruiting other immune cells. Regulatory T cells (Tregs) maintain self-tolerance and follicular helper T cells (T$_{FH}$) provide help to B cells for antibody production (Abrignani, 2015).

T cell subsets can be distinguished by the expression of transcription factors that regulate and maintain their lineage-specific effector functions. Differentiation of T cells also involves chromatin remodelling by posttranslational histone modifications. This ensures the expression of specific surface molecules, called homing receptors, which enable these effector cells to migrate to non-lymphoid sites of inflammation where they secrete cytokines, e.g. IFN-γ for T$_H$1 cells, that control the pathogen (Reinhardt, Khoruts, Merica, Zell, & Jenkins, 2001). Epigenetic modifications ensure that the cytokine profile of T$_H$ cells remains upon cell division (Russ et al., 2013).

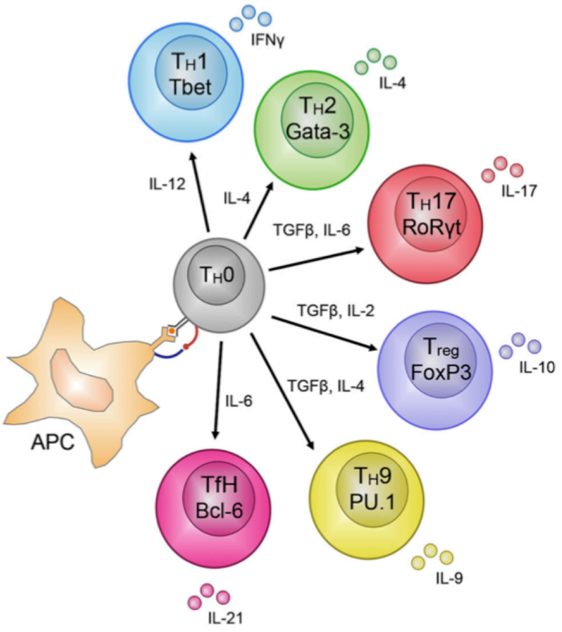

Figure 3 Differentiation of CD4$^+$ T helper cells. Naïve T cells have a very high plasticity and can differentiate into many different subsets, depending on cytokines secreted by the antigen-presenting cell (APC). The different subsets can be distinguished by transcription factors that maintain lineage-specific effector functions. The subsets also secrete cytokines that help controlling the pathogen. (image: (Russ et al., 2013))

Compared to naïve T cells, these differentiated antigen-experienced T cells lost their stem-cell-like property and are less flexible. Nonetheless, subsets exist that retain some plasticity. Upon antigenic re-stimulation, they are able to secrete additional cytokines or even change from helper to regulatory functions (Abrignani, 2015).

The number of effector cells increases up to one week into the response. During the following 1 – 2 weeks of contraction phase, about 90 % of the effector cells die, but a population of long-lived memory cells remain (Pepper & Jenkins, 2011).

4.1.2 Models for memory T cell differentiation

Memory is a characteristic of the acquired immune system. It results from the clonal expansion and differentiation of antigen-specific lymphocytes that leads to a dynamic pool of memory cells. They accumulate over the lifetime of an individual and ensure rapid response upon re-infection (Sallusto et al., 2004).

Naïve and memory T cells can be distinguished by their differential expression of CD45 isoforms, resulting from alternative splicing of three exons encoding the extra-cytoplasmic domain. Naïve T cells are positive for CD45RA and negative for CD45RO, whereas memory T cells show a reciprocal expression of these surface proteins. (Michie, McLean, Alcock, & Beverley, 1992) Within the memory T cell pool, distinct subsets fulfil different tasks that are related to their capacities to migrate to specific organs, called homing, and effector function: central memory and effector memory T cells.

Central memory T cells (T_{CM}) mediate reactive memory and have no or little effector function. They express CCR7 and CD62L that enables them to home to T cell areas of SLOs through high endothelial venules. They possess a high sensitivity to antigenic stimulation and are only little dependent on co-stimulatory signals. Upon TCR triggering within SLOs, they produce mainly IL-2. Then they proliferate and differentiate into effector cells that produce IFN-γ and IL-4 (Cyster, 1999). Also, they give stimulatory feedback to dendritic cells and B cells and therefore promote immune response (Sallusto et al., 2004).

Effector memory T cells (T_{EM}) have immediate effector functions. They continuously circulate through the body and express distinct chemokine receptors and adhesion molecules that enable them to home to inflamed tissues. Within several hours of TCR stimulation they secrete microbicidal cytokines, e.g. IFN-γ, IL-4 and IL-5. They do not express CCR7, and they are mainly negative for CD62L. Other T_{EM} subsets express surface markers characteristic for T_H1 and T_H2 cells (Sallusto et al., 2004).

Since expression of chemokine receptors, adhesion and co-stimulatory molecules is very heterogeneous for both T_{CM} and T_{EM}, phenotypic characterisation of these subpopulations only applies to resting cells and those not involved in antigenic response. For example, after TCR triggering or lymph node immigration of T_{CM}, CD62L is rapidly shed (Chao et al., 1997; Kishimoto & Jutila, 1990). Also, they loose expression of CCR7 upon TCR triggering, express surface markers characteristic for T_H1 and T_H2 and therefore generate effector cells (Sallusto et al., 2004).

In general, differentiation of naïve T cells into effector and memory cells has been proposed to correlate with decrease in longevity, self-renewal and proliferative potential, and with memory potential (Kaech & Cui, 2012). Also, cells loose their plasticity upon differentiation (Sallusto et al., 2004). In recent years, several models have been proposed that explain differentiation of naïve T cells and postulate the formation of the T cell memory pool.

a) Signal-Strength Model

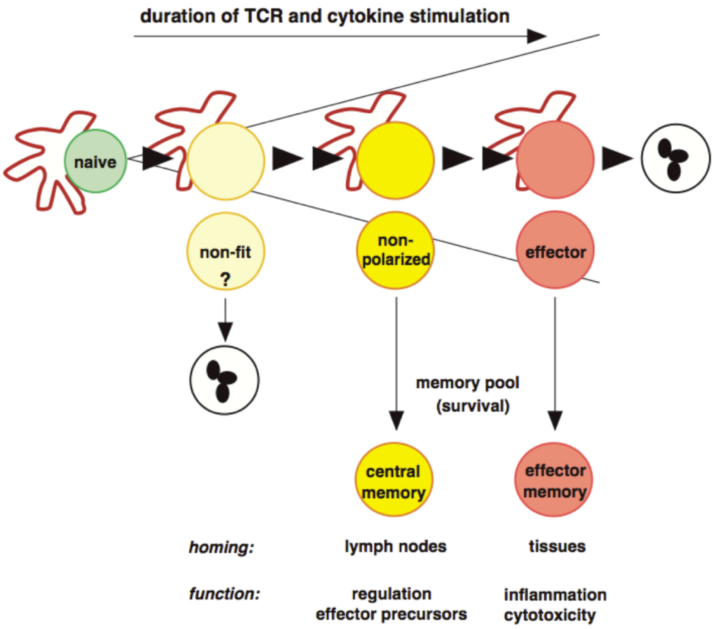

Figure 4 Model for linear T cell differentiation based on signal strength. Activated T cells undergo hierarchical levels of differentiation depending on the strength of TCR and cytokine signalling. Cells receiving excessive or insufficient stimulation die. High signal strength leads to effector cell formation, whereas intermediate signalling results in non-polarized cells. The fittest cells survive and create immunological memory as effector memory and central memory cells, respectively. (image: (Lanzavecchia & Sallusto, 2000))

One of the most popular models proposes linear T cell differentiation that is driven by the duration of TCR signalling (Figure 4) (Lanzavecchia & Sallusto, 2000). This signal is the main factor for T cell differentiation. Two additional events that can compensate each other are the duration of interaction, which can last from a few minutes to up to several hours, and the concentration of stimulatory molecules and antigens (Sallusto et al., 2004). Together with cytokine receptor signalling, T cells follow hierarchical thresholds of differentiation. Since all signalling events can be regarded as being stochastic, a T cell population with great variety of differentiation forms. Primed T cells can therefore form effector cells or arrest at intermediate levels of differentiation. According to this model, high levels of differentiation signals occur at early stages of infection due to high antigen presentation and cytokine production by immune cells. Proliferation of antigen-specific T cells drive them into effector cells, some of which persist as effector memory cells. Later during the infection, differentiation signals decrease which leads to the expansion of non-effector cells, of which some persist as T_{CM} (Lanzavecchia & Sallusto, 2000).

b) Model for simultaneous generation of T cell memory subsets

The model proposed by Pepper and Jenkins (Pepper & Jenkins, 2011) is based on the assumption that T_{EM} and T_{CM} display metastable non-convertible populations and are therefore simultaneously generated. They propose that lineage committed effector T_H1,

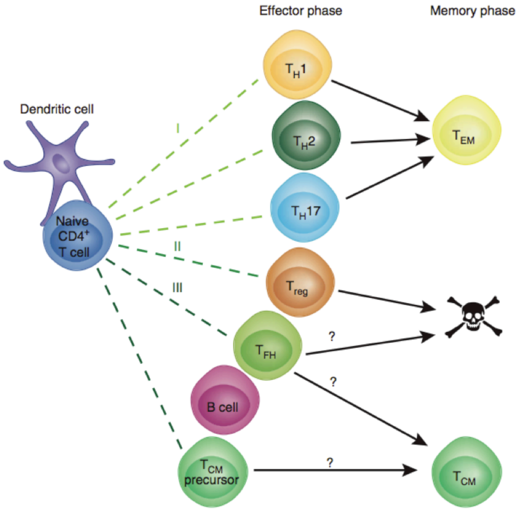

Figure 5 Model for simultaneous generation of T_{EM} and T_{CM} cells. This model suggests three pathways for memory T cell formation from naïve T cells. I) naïve T cells differentiate into effector cells that form T_{EM} cells during the contraction phase. II) Effector cells that lack the potential to create immunological memory die. III) T cells of the effector phase interact with B cells and become T_{CM} cells. (image: (Pepper & Jenkins, 2011))

T_H2 and perhaps T_H17 cells survive the contraction phase and form T_{EM} cells. Regulatory T cells and T_{FH} cells do not enter the memory pool. They either die during the contraction phase or they down-regulate their specific cell markers and become T_H1 effector memory cells or quiescent memory cells. In their model, T_{CM} cells form from T_{FH} and T_{CM} precursors after interaction with B cells.

c) Model for linear differentiation including conversion

Recent findings, reviewed by Abrigani et al., suggest that T cell subsets posses various degrees of plasticities that enables them to acquire new characteristics and functions in secondary immune responses (Abrignani, 2015). Thus, T_H cells are not lineage committed but can switch to other subtypes under certain cytokine exposure. In their proposed model, T_{CM} cells are at an intermediate stage of differentiation, being able to rapidly expand and produce high levels of effector cells. They are highly plastic and can switch to other subsets upon cytokine signalling. T_{EM} are more differentiated and less plastic but can become polyfunctional. Effector cells display highest degree of differentiation and less plasticity (Abrignani, 2015).

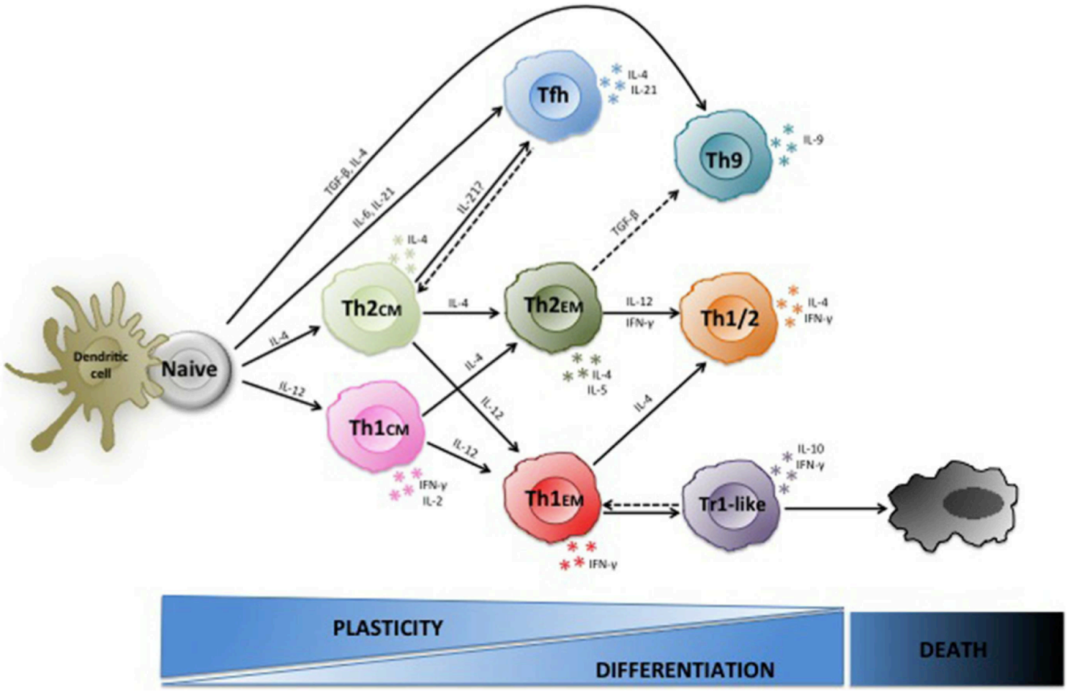

Figure 6 Model for T cell differentiation including interconversion. Naïve T cells differentiate into effector cells under the influence of cytokines. Central memory T cells are arrested at the early stage of differentiation. They are highly plastic and can switch T cell lineage. Effector memory T cells are more differentiated, less plastic but can still acquire other functionalities upon cytokine stimulation. Effector T cells are highly differentiated and might also acquire new characteristics and functions in secondary immune responses (not shown). (image: (Abrignani, 2015))

4.1.3 T cell adhesion

Recruitment of T cells into lymphoid organs and peripheral tissues is crucial for immune system function. To exit the circulatory systems and reach the site of inflammation, T cells of all differentiation states must first adhere to the extracellular matrix of vessels.

The extracellular matrix is composed of many structural and biologically active macromolecules, such as fibronectin, collagens, laminins and heparin sulphate proteoglycans (Dominguez & Hammer, 2014; Weeks et al., 1994). These structural elements are recognized by a great variety of receptors that T cells possess on their cell surface.

Integrins are important players in these binding events that mediate cell adhesion. They are composed of an α and a β subunit. Interaction of integrins with their ligands, e.g. vascular adhesion molecule-1 (VCAM-1) and fibronectin, do not only mediate adhesion and but are also important in signal transduction (Rose, Han, & Ginsberg, 2002).

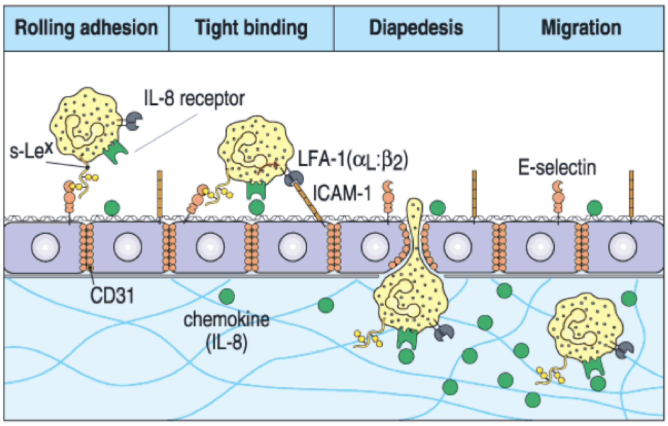

Figure 7 T cell adherence and traversing. Adhesion molecules expressed on endothelial cells of blood vessels capture T cells and cause their adherence. Important for tight arrest is binding of integrin LFA-1 to ICAM-1. Cells can than penetrate the endothelium and migrate under the influence of chemokines to the site of inflammation. (image: (Murphy, 2011))

The dominant integrin that is involved in lymphocyte homing to lymph nodes and peripheral tissues is Lymphocyte Function Associated Antigen 1 (LFA-1; αLβ2). This receptor recognizes Intercellular Adhesion Molecule 1 (ICAM-1, also known as CD54), a transmembrane glycoprotein that contains five extracellular domains (Yang et al., 2004). It is expressed at basal levels on endothelial cells and is up-regulated under inflammatory conditions (Springer, 1990). Expression of LFA-1 has been reported to depend on T cell differentiation (Sanders, Makgoba, & Sharrow, 1988) (see section 7.1) and its binding to ICAM-1 is a crucial step for the adherence of circulating T lymphocytes to endothelial cells of the vessels (Figure 7) (Murphy, 2011; Warnock, Askari, Butcher, & Andrian, 1998). Furthermore, downstream LFA-1 signalling leads to F-actin cytoskeleton remodelling and therefore strengthens T cell adhesion (Porter, Bracke, Smith, Davies, & Hogg, 2002).

LFA-1 binds preferentially to ICAM-1 cis-dimers by recognising an extracellular dimerization site (Yang et al., 2004). In contrast, many integrins do not recognize structural protein elements, but rather specific amino acid sequences within their ligands. One of those binding motifs is RGD, which is present in extracellular matrix proteins, e.g. fibronectin, vitronectin and collagen (Pfaff, 1997). Laminins are also ligands for integrins, but are also recognized by the 67 kDa laminin receptor 67LR (Nelson et al., 2008). The main adhesion-promoting sequence of laminin is IKVAV (Tashiro et al., 1989), located in the α chain of the protein (Nomizu et al., 1995).

Activation of integrins is often triggered by chemokines. These small protein molecules regulate lymphocyte trafficking during normal and inflammatory condition and play also a role in T cell maturation and migration (Bono et al., 2007).

4.1.4 T cell migration

Migration of T lymphocytes is a complex process that is regulated by adhesion receptors, cytokines and chemokines (Butcher & Picker, 1996).

Chemokines are a family of small, mostly secreted protein molecules that chemo-attract cells by G protein-coupled receptor signalling (Cyster, 2005). These highly basic proteins form stable gradients by binding to sulphated proteins and proteoglycans (Cyster, 1999). Specific arrangement of chemokines, cytokines and adhesion molecules regulates T cell migration and enables T cell homing into various tissues where they can fulfil their function.

Naïve T cells preferentially migrate to SLOs, including lymph nodes, Peyer's patches (PP, lymphoid nodules in the small intestine) and the spleen. Here, they recognize their cognate antigen and become activated (Figure 8). They then undergo extensive changes in their cytokine and homing molecule expression that enables them to travel to inflamed tissues and carry out effector functions. Thus, antigen-experienced T cells display more diverse adhesion and migratory properties compared to naïve T cells (Mora & Andrian, 2006).

T_{CM} express L-selectin and CCR7 that enable them to migrate to SLOs. In contrast, effector and effector memory T lymphocytes do not express these lymph node homing receptors but especially migrate to non-lymphoid sites of inflammation. (Sallusto, Lenig, Förster, Lipp, & Lanzavecchia, 1999)

Effector and effector memory T cells show remarkable migratory selectivity for certain organs. This is due to their expression of unique combinations of adhesion and chemokine receptors and is regulated by the spatial and temporal expression of respective ligands by tissue cells (Kunkel & Butcher, 2002).

Skin-homing T cells express E- and P-selectin ligands and the chemokine receptor CCR4 (Mora & Andrian, 2006; Sallusto et al., 2004). T lymphocytes that home to the gut do not express these molecules. Instead, they up-regulate integrin $\alpha4\beta7$ and the chemokine receptor CCR9 (Zabel, Agace, & Campbell, 1999). The respective ligands of these homing receptors, mucosal vascular addressin (MadCAM-1) and CCL25, are strongly expressed by epithelial cells in the small intestine and in lamina propria venules (Mora & Andrian, 2006) (Kunkel & Butcher, 2002) (Papadakis et al., 2000). Expression of these gut homing molecules is also highly dependent on the vitamin A metabolite, retinoic acid (RA), expressed by dendritic cells (Iwata et al., 2004).

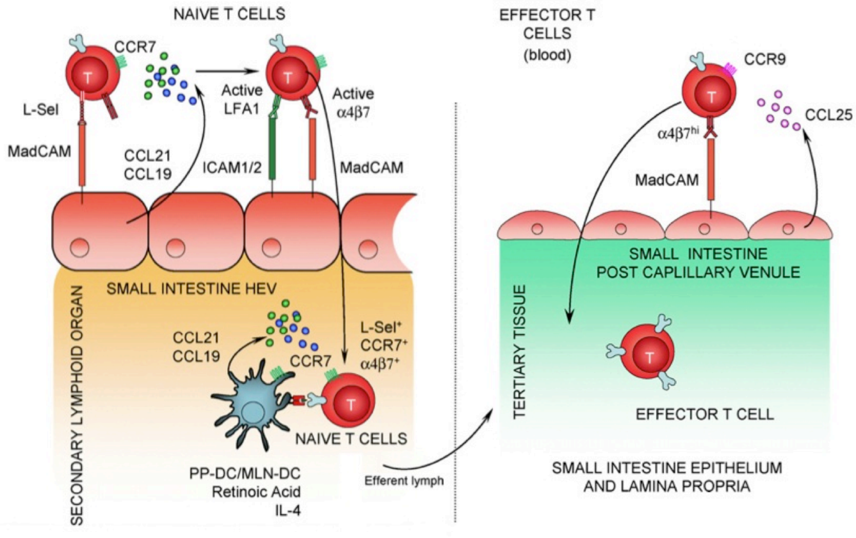

Figure 8 Role of adhesion and chemokine receptors in T cell homing. Naïve T cells enter SLOs through high endothelial venules. Secreted chemokines CCL19/21 attract naïve T cells that express CCR7. Adhesion is mediated by L-selectin and LFA-1 binding to MadCAM and ICAM, respectively. These interactions enable naïve T cells to arrest and transmigrate to the T cell zones in SLOs. Here, they encounter their cognate antigen and remodel their homing receptors. For homing to the small intestine, T cells up-regulate $\alpha4\beta7$ and CCR9. The corresponding ligands MadCAM and CCL25 are expressed by cells in the small intestine. Other factors like retinoic acid and IL-4 also contribute to targeting T cells to the small intestine. (image: (Bono et al., 2007))

The homing potential of activated T lymphocytes depends on the lymphoid tissue environment during their activation and their contact with dendritic cells. For example, T cell activation by intestinal dendritic cells from PP induces gut-homing capacities. Upon re-stimulation by dendritic cells from a different SLO T cells can also be reprogrammed and change their homing capacities (Mora & Andrian, 2006).

In contrast to tissue-specific homing proteins, several surface molecules expressed on T cells have a general role in T cell trafficking, such as CD44 and LFA-1. Due to their broad expression patterns, they do not serve as selective markers for migration into specific tissues (Woodland & Kohlmeier, 2009).

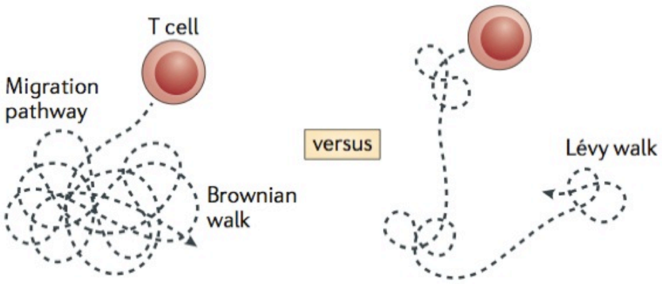

Figure 9 Migration patterns of T cells. Naïve T cells have been reported to migrate in SLOs by random Brownian walk. In contrast, T cells in non-lymphoid tissues have been suggested to migrate by Lévy walks. This covers more territory than Brownian walks. (image: (Masopust & Schenkel, 2013))

Within both SLOs and peripheral tissues T cells must efficiently migrate in order to fulfil their function in immunosurveillance and pathogen control. The locomotion and trafficking of naïve $CD4^+$ T cells in SLOs has been described by Miller et al. (Miller, Wei, Cahalan, & Parker, 2003). They observed a robust motility with an average velocity of ~ 11 μm/min. Cells switched between states of low and high motility (> 25 μm/min, up to 40 μm/min) and described a migration pattern analogous to Brownian walk. Since cells did not migrate collectively but on independent trafficking path, they suggested that contact of T cells with antigen-presenting cells is a stochastic process (Miller et al., 2003).

In contrast to naïve T cells in SLOs, effector T cell velocity in non-lymphoid tissues has been reported to be much lower, ranging from ~ 4 to 10 μm/min (Masopust & Schenkel, 2013). Also, effector $CD8^+$ T cells that have entered the central nervous system do not migrate by using Brownian walk, but rather scan the infected brain in patterns known as Lévy walks (Figure 9) (Harris et al., 2013). By this, they cover more territory and thereby increase the probability of encountering their cognate antigen, which is required for maintaining the effector T cell population in the brain and ensure efficient immune response.

Thus, trafficking signals finely control the movement of distinct T cell subsets to specific tissues for ensuring protective immunity. Nonetheless, tissue inflammation can also lead to chronic pathological conditions and diseases. The current challenge is to further identify tissue specific trafficking molecules and the key subsets that drive these disease processes (Luster, Alon, & Andrian, 2005).

4.1.5 T cells in Graft-versus-Host-Disease

Dysregulation of T cell functions are associated with various diseases. One of these diseases is (acute) Graft-versus-Host-Disease ((a)GVHD).

Acute GVHD is the primary cause for morbidity and mortality after allogenic hematopoietic stem cell transplantation. This therapy is a widely used for curing haematological malignancies (e.g. leukaemia and lymphomas) and inherited or acquired non-malignant disorders of blood cells, e.g. sickle-cell anaemia and aplastic anaemia (Shlomchik, 2007). Mature T cells from the donor reconstitute T cell immunity and eradicate malignant cells in the host. As a great drawback of this therapy, T cells might recognize the recipient as non-self and attack host tissue, e.g. skin, liver and the gastrointestinal tract. GVHD affects about 60 % of recipients of allo-HSCT (Leisenring, 2006) and is the major barrier of this therapy to become a successful and widespread application in clinical settings (Paczesny, 2013).

Many studies have addressed the mechanisms and especially the role of T cells in GVHD. One cause for diseases initiation has been found to be MHC-mismatching between donor and recipient. Interestingly, effector memory T cells do not cause GVHD for both MHC-matching and –mismatching (Shlomchik, 2007).

These findings could be confirmed by Brede et al. who monitored *in vivo* T-cell subset migration into Peyer's patches (PPs) during aGVHD (Brede et al., 2012). In their study, transgenic T cells were transplanted into irradiated allogeneic mice. They found that T_{EM} do not induce lethal GVHD and migrate most efficiently to peripheral tissues and not to SLOs and Peyer's patches. In contrast, T_{CM} and even more efficiently T_N home to PPs and to SLOs. Both subtypes were previously found to induce lethal GVHD after allogenic hematopoietic stem cell transplantation (Brede et al., 2012).

Nonetheless, the mechanisms by which T_{EM} fail to cause GVHD, how this is correlated with their migration characteristics and how they differ to other T cell subtypes remain unclear.

In the last years, T cell subpopulations have been identified as potential biomarkers for GVHD. Magenau et al. found that the amount of $CD4^{+}$ $CD25^{high}$ $FOXP3^{+}$ regulatory T cells (Tregs) in peripheral blood of patients predicts the occurrence and severity of the disease. Decreased frequencies of Tregs are associated with GVHD, and their amount linearly decreases with increasing grades of GVHD. Also, patients suffering from GVHD have a higher percentage of effector memory T cells than healthy persons (Magenau et al., 2010).

In addition, severity of GVHD can be correlated with an elevated frequency of T_{EM} in peripheral blood. Also, a preponderance of $CD4^{+}$ T_{EM} relative to T_{CM} has been found to be characteristic for severe GVHD (Yamashita, 2004).

Thus, T cell subpopulations in peripheral blood have great potential for serving as biomarkers for predicting the severity of (a)GVHD and improving disease interventions.

4.2 Adhesion analysis with Reflection Interference Contrast Microscopy (RICM)

Reflection interference contrast microscopy (RICM) is an optical method for studying interactions of dynamic living systems that are in proximity to a substrate. Image formation in RICM is based on the reflection of polarized light by an object. From the obtained interference image one can reconstruct the height profile of the object above the substrate. Compared to other techniques used for studying the interaction of two interfaces, e.g. total internal reflection fluorescent microscopy that allows studying fluorescently labelled objects, there is no need of a marker. RICM is a non-invasive method that allows investigations in real time over a chosen time span. It is often used in cell biology for studying cell adhesion and dynamics, and is highly suitable for visualising fine cell outlines, e.g. lamellipodia, and adhesion topologies of cells, which is not possible with conventional light microscopy (Abercrombie & Ambrose, 1958; Verschueren, 1985).

4.2.1 Image formation and height calculation

For RICM image formation, cells need to adhere to a surface that is illuminated from underneath. The incident light becomes reflected at different interfaces (Figure 10).

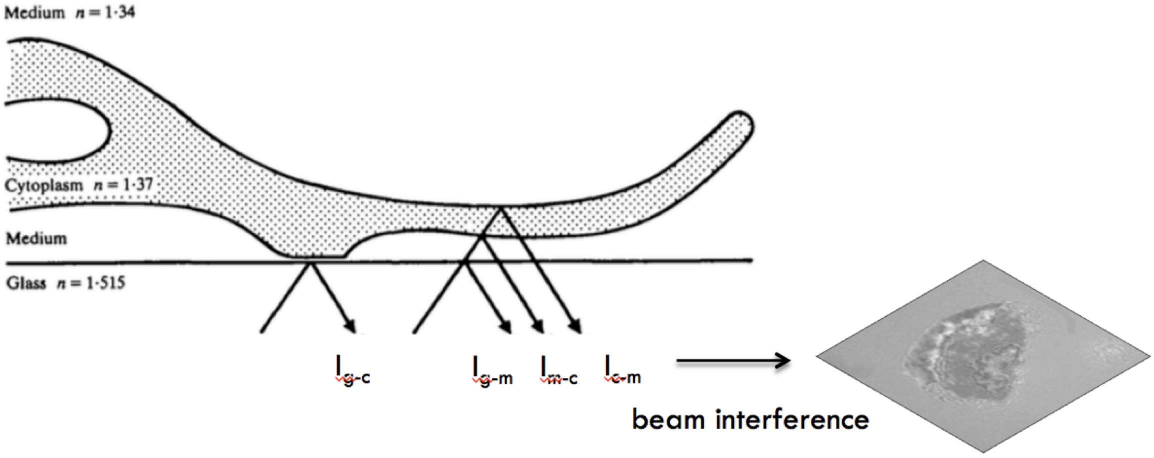

Figure 10 Principle of image formation in Reflection Interference Contrast Microscopy (RICM). Incident beams are reflected on the interfaces glass-cell (I_{g-c}), glass-medium (I_{g-m}), medium-cell (I_{m-c}) or cell-medium (I_{c-m}). The interference of reflected beams results in an interferogram in which intensity values on every pixel position correlate with the distance between the cell and the substrate. (image: (Verschueren, 1985))

When the cell is in direct contact to the glass surface, the beam is reflected at the glass-cell interface. Reflectivity is determined by the glass-cell transition ($I_{g\text{-}c}$). When the cell is not in direct contact with the surface, reflection occurs at the glass-medium ($I_{g\text{-}m}$) and medium-cell ($_{Im\text{-}c}$) interfaces.

Reflected beams can interfere since the distance between glass and cell is in the order of magnitude of the light's wavelength. The intensity of the interferogram at every (x,y) position can be calculated as follows:

$$I(h(x,y),\lambda) = I_1 + I_2 + 2\sqrt{I_1 * I_2}\, cos\left(\frac{4\pi n h(x,y)}{\lambda} + \phi\right)$$

with: $I(h(x,y),\lambda)$: intensity of pixel (x,y) of the interferogram

h: distance between object and substrate

λ: wavelength

I_1 and I_2: intensities of beams reflected on interfaces

n: reflective index of medium

ϕ: phase shift of the beam upon reflection on the interface ($\phi = \pi$ for $n_{object} > n_{medium}$)

Thus, the intensity values of the interference image correlate with the distance between the surface and the object. When the object is in direct contact with the surface, the cosine in the equation above is -1 and therefore corresponding regions appear dark in the image.

The interferogram allows for calculating the distance between substrate and object. This is done by the Min-Max-Method, that applies the maximal possible intensity I_M and the minimal intensity I_m, given that $n_{object} > n_{medium}$.

$$I_M = I_1 + I_2 + 2\sqrt{I_1 I_2}$$

$$I_m = I_1 + I_2 - 2\sqrt{I_1 I_2}$$

$$h(x,y) = \frac{\lambda}{4\pi n}\, arccos\left(\frac{2I(x,y) - (I_M + I_m)}{I_M - I_m}\right)$$

The intensities I_1 and I_2 of the reflected beams are dependent on the intensity of the incident beam as follows:

$$I_1 = r_{01}^2 I_0$$

$$I_2 = (1 - r_{01}^2) r_{12}^2 I_0$$

with r being the Fresnel refraction coefficient $r_{ij}^{\perp} = \frac{n_i \cos \Theta_i - n_j \cos \Theta_j}{n_i \cos \Theta_i + n_j \cos \Theta_j}$ (i,j = 0,1,2).

Light that is reflected from the interface between medium and cell membrane is of very low intensity compared to the incident beam ($I_{m\text{-}c} \cong 10^{-3} * I_o$). Therefore, the interference signal can be superimposed by scattered light, which can cause strong artefacts in image formation. This problem can be minimized by using the Antiflex technique (see section 4.2.2) (Gingell & Todd, 1979; Rädler & Sackmann, 1993).

The major disadvantage of the RICM technique is that the absolute phases of the reflected beams cannot be determined, due to the periodicity that occurs during beam interference. This can be overcome by using two different wavelengths. In dual-wavelength RICM the simultaneously obtained interferograms of two different wavelengths introduces additional periodicity and boundary conditions, which enables to measure absolute distances with high precision. (Schilling, Sengupta, Goennenwein, Bausch, & Sackmann, 2004)

4.2.2 RICM setup

As mentioned before, formation of the interference image in RICM can be distorted by scattered light. Image artefacts can be avoided by using the Antiflex technique, which employs a polarisator, the λ/4-plate and an analysator. The principle of the setup used in this thesis is shown in Figure 11. It was implemented on an inverted microscope.

The incident light passes the polarisator and is modified to approximately parallel illumination by a two-iris system (not shown). The linear polarized light is then directed

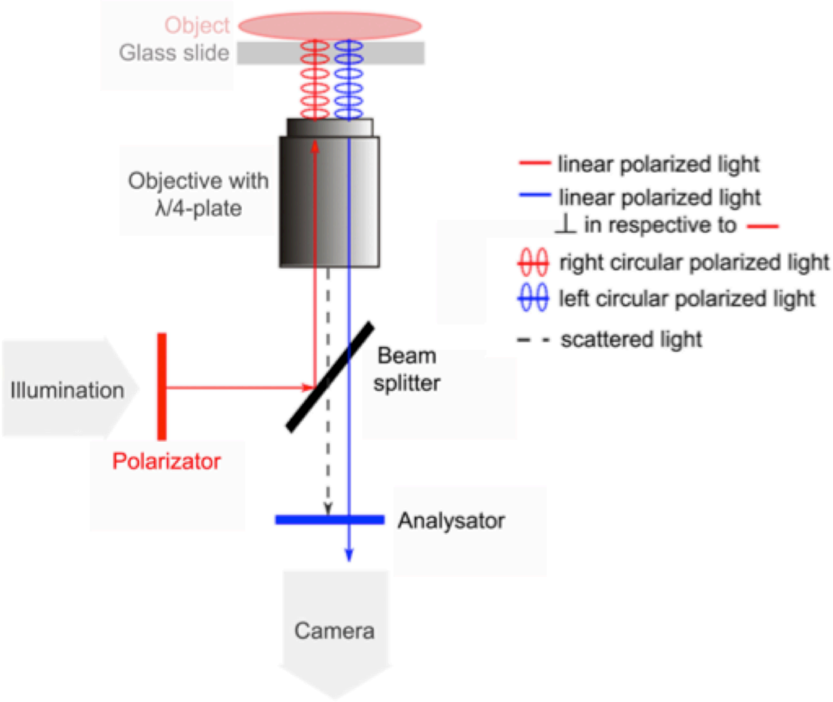

Figure 11 Sketch of the RICM setup with implemented antiflex technique. By including a polarisator, λ/4-plate and an analysator scattered light cannot contribute to image formation and therefore artefacts are reduced. (image accordingly to (Nolte, 2012))

though the objective to the object by a beam splitter. The objective is equipped with a λ/4-plate, which causes circular polarization (Limozin & Sengupta, 2009). Upon reflection on optically thin media, the electric field component of the circular polarized light is parallel to the incident plane and is phase shifted by π. The perpendicular magnetic component is not influenced. Upon reflection on optically thick media, the effect is opposite and the magnetic field component is phase shifted by π. Thus, the direction of polarization is inverted due to reflection on both interfaces. When the light passes the λ/4-plate again, it is again linear polarized, but now 90° rotated in respect to the incident light. The beam then passes the analysator, which is set at an angle of 90° to the polarisator. Scattered light cannot pass the analysator. This is due to the fact that scattering and reflection occur mostly before the light passes the λ/4-plate, and therefore the scattered light is perpendicular polarized compared to the light reflected on the object. Therefore, filtering out the scattered light greatly enhances interference signals of even weakly reflective objects (Limozin & Sengupta, 2009; Nolte, 2012). This imaging technique therefore allows studying interaction of various complex systems with the surface.

4.3 Fractal analysis

The complexity of systems can be characterized with fractal analysis. A fractals is a pattern that repeats itself at different scales (Mandelbrot, 1967). This property is called “Self-Similarity” and is occurring very frequently in nature, e.g. in mountains and coastlines, but also in biological systems such as branching of trees, vascular networks and cell topology. The mathematical description of these self-repeating patterns became particularly popular through the mathematician Benoit Mandelbrot who also coined the term fractal geometry (Mandelbrot, 1983).

4.3.1 Fractal dimension

Fractal dimension (Df) measures the complexity of objects that do not completely occupy the space they exist in and can therefore not be sufficiently described with Euclidian geometry. For example, a meandering coastline is a one-dimensional object, which is zigzagging in and out of a second dimension and thus has a space filling capacity with a Df between 1 and 2. A vascular network does not completely occupy a 3-dimensional space. Therefore, its Df lies between 2 and 3 (Meier et al., 2013).

Figure 12 shows the “Koch Curve”. It is created by repeatedly replacing one third of a straight line by an outline of an equilateral triangle. Thus, each line is replaced by four lines, each being one-third in length of the original. The total length of the curve increases with every iteration by one third, and after n iterations its lengths will be $(4/3)^n$ times the original triangle perimeter. Its Df is log4/log3, so Df = 1.26.

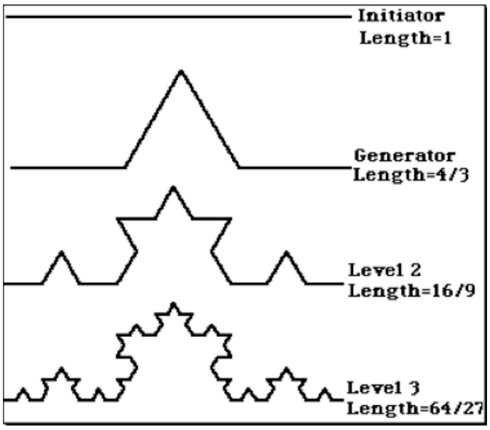

Figure 12 Fractal pattern of the “Koch Curve”. Every line is replaced by four lines, each being one-third in length of the original. The pattern becomes more and more complex but displays repetition independent of size and refinement level, called “self-similarity”. Fractal dimension (Df) quantifies the rate of addition of structural detail with increasing magnification and therefore serves as a measure of complexity. Df of this pattern is 1.26.

The most frequently used method for calculating the fractal dimension is the box counting method, defined by Russel et al. (Russell, Hanson, & Ott, 1980). The principal is shown in Figure 13, using a cell outline as an example. Briefly, a grid with box size s is overlaid onto the image and the number of boxes occupied by the pattern is determined. Then, the box size is sequentially decreased and the occupied boxes are also determined. The fractal dimension can than be calculated by the logarithmic ratio of the number of occupied boxes and the box size (Figure 13b). The fractal dimension therefore corresponds to the slope of the log-log plot (Lopes & Betrouni, 2009).

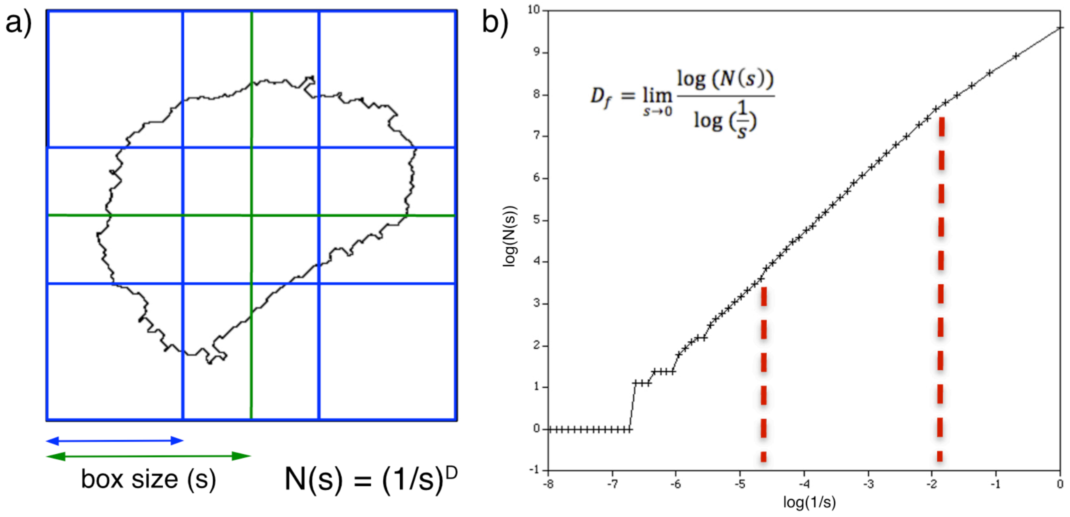

Figure 13 Principle of calculating the fractal dimension (Df). a) A grid with box size s is overlaid onto the image and the number of boxes occupied by the pattern is determined. The box size is sequentially decreased (indicated by green and blue colour). b) The fractal dimension can be determined by the logarithmic ratio of the number of occupied boxes and the inverse of the box size. Graphically, it corresponds to the slope of the log-log plot. Hereby, the interval for slope determination needs to be carefully chosen, indicated by dashed lines. Towards the left, s approaches the size of the object; towards the right, it approaches single pixel size.

4.3.2 Fractals in biology

In the past years, several biologic systems with complex spatial patterns have been shown to possess a fractal and self-similar structure. Examples are branching neurons and blood vessels, the structure of the bone marrow, protein structures and the distribution of protein aggregates on cell membranes, chromatin organization and even local nucleotide repetitions in DNA (palindromes) (Losa, 2011; Meier et al., 2013; Naeim, Moatamed, & Sahimi, 1996). Also, dynamic processes like signals derived from electrocardiography or the development of foetal brain blood vessels can be studied via fractal analysis (Lopes & Betrouni, 2009).

In biological systems, changes in Df describe complexities and irregularities that result from changes in structural organization and functional coordination. For example, cells can be seen as complex adaptive systems in which small disturbances such as genetic mutation can have an immense impact on the cell phenotype. (Mashiah et al., 2008) Thus, changes in Df reflect changes in cell phenotype under physiological and pathological conditions.

This has been shown in several studies. For example, Klein et al. imaged tumor cells by RICM and determined the Df of tumor cell outlines and their adhesion topology. They found that increased malignancy is correlated with increases in Df (Klein et al., 2013).

Furthermore, lymphatic and lymphoma cells were distinguished by the fractal dimensions of their nuclei ‘coastlines’ (Mashiah et al., 2008). The differentiation of glial cells has also been monitored with fractal analysis, whereby *in vitro* differentiated cells showed increased morphological complexity that correlated with larger Df values (Behar, 2001).

Meier et al have studied the fractal organisation of the human T cell repertoire. They compared healthy stem cell transplantation donors with recipients after transplantation and stated that fractal analysis of high-throughput TCR β sequencing data in a powerful tool for understanding immune reconstitution after stem cell transplantation (Meier et al., 2013).

Concluding, many studies have been reported that apply fractal analysis on single cells or even more complex biological systems (Losa, 2011; T. G. Smith, Lange, & Marks, 1996). This method is highly suitable for quantifying the complexity of these systems under non-linear changes, such as mutation or differentiation, in physiological and pathological conditions.

4.4 Mimicking T cell homing routes with biofunctionalized nanopatterned surfaces

in vitro cell migration analysis is a powerful research tool for studying adhesion and migration of cells in dependence on signalling molecules. Elucidating the ability of cells to respond to biomolecule gradients requires the generation of gradients that are quantifiable, controllable and mimic those presented *in vivo*.

Traditional methods for generating gradients *in vitro* are biological hydrogels, micropipette-generated gradients or transwell assays. These approaches have the disadvantages of not generating highly reproducible or controllable gradients, they also lack spatial and temporal gradient control of gradient formation (Keenan & Folch, 2008). More recently, microfluidic devices have been employed for e.g. studying T cell migration in response to chemokine gradients (Lin & Butcher, 2006; Wu et al., 2015). This approach can precisely configure gradient conditions, but it has the disadvantage that generated chemokine gradients are soluble, whereas *in vivo*, these signalling molecules very often form immobilized gradients (Cyster, 1999; Patel et al., 2001). This has been realised in some studies that employed e.g. protein adsorption or microcontact printing (Dominguez &

Hammer, 2014; Stachowiak, Wang, Huang, & Irvine, 2006; Woolf et al., 2007). However, these approaches do not realise covalent binding of chemokines to the surfaces, which causes uncontrollable changes in their concentrations due to dissociation or disruption from the surface caused by the cells.

Therefore, new approaches that employ stably immobilized chemokine gradients need to be developed. Since motility of T lymphocytes guided by chemokines is modulated by adhesive interactions *in vivo*, co-presentation of adhesion molecules on the substrates is of great interest and displays an additional challenge (Butcher & Picker, 1996; Mueller, Gebhardt, Carbone, & Heath, 2013).

One technique that realises protein immobilization on glass surfaces is block copolymer micellar nanolithography (BCML) that generates quasi-hexagonally arranged gold nanoparticles with defined spacings, which serve as anchoring points for proteins (Lohmüller et al., 2011; Spatz et al., 2000). Additional functionalization of the glass substrate between the gold particles with poly(ethylene glycol)-alkyne (PEG-alkyne) allows orthogonal functionalization with azide-containing ligands (Schenk, Boehm, Spatz, & Wegner, 2014).

This method realises chemokine presentation on surfaces either homogeneously or with gradient spacing, and also co-presentation of adhesion molecules with high specificity and stability. This allows generating surfaces that mimic T cell homing routes and studying migration of T lymphocytes under the influence of chemokines, chemokine gradients and adhesion molecules.

4.4.1 Block Copolymer Micellar Nanolithography (BCML)

BCML is a bottom-up approach, which allows the deposition of quasi-hexagonally arranged metallic nanoparticles on substrates with defined distances in the nanometre regime (Spatz et al., 2000).

The technique relies on the self-assembly of diblock copolymer micelles. The amphiphilic diblock copolymer polystyrene(x)-*block*-poly(2-vinylpyridine)(y), short PS(x)-b-P2VP(y), consists of a hydrophobic polystyrene (PS) block and a hydrophilic poly(2-vinylpyridine) block (P2VP) that are covalently linked; x and y determine the number of subunits (Figure 14A). When these copolymers are solved in toluene above a critical concentration, they self-assemble and form inverse micelles. (Aydin et al., 2009)

The polar cores of the micelles formed by the 2VP-units can now incorporate metal precursor salts and therefore serve as nano-reactors (Figure 14B). Added $HAuCl_4$ thus diffuses into the micelles and protonates the cores that are stabilized by the negatively charged Au(III) complex $AuCl_4^-$ (Figure 14C) (Spatz 2000).

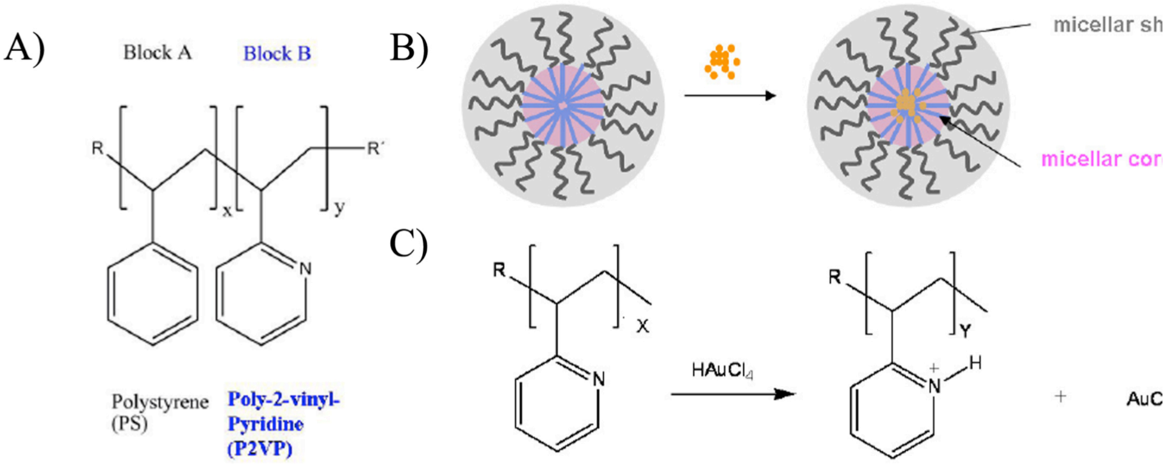

Figure 14 Formation of micelles from diblock copolymers and core neutralization. A) The diblock copolymer polystyrene(x)-*block*-poly(2-vinylpyridine)(y) consists of a hydrophobic PS-block and a hydrophilic P2VP-block (highlighted in blue). B) When toluene is used as a solvent, reverse micelles are formed that serve as nano-reactors. The polar 2VP-blocks form the core in which $HAuCl_4$ solubilises. C) In the polar core of the micelles pyridine units are protonated, $AuCl_4^-$ -Ions are bound as counterions. (adapted from (Hirschfeld-Warneken, 2009))

Depositing a monolayer of these gold-loaded micelles onto substrates can be achieved by dip-coating (Figure 15). For this, a cleaned flat substrate, e.g. a glass plate or mica, is immersed into the micellar solution. When retracting the substrate with a defined velocity, the micelles adsorb and assemble on the substrate at the air-solvent-substrate interphase. During subsequent film drying, micelles become hexagonally arranged. Following, the substrates bearing the micellar monolayer are exposed to reactive gas plasma. During this plasma etching process, the incorporated $AuCl_4^-$ -ions inside the micelles are reduced to form particles of elemental gold, and the particles' locations correspond to the pattern of micelles in the original film. At the same time, the polymer coating is completely removed (Spatz 2000).

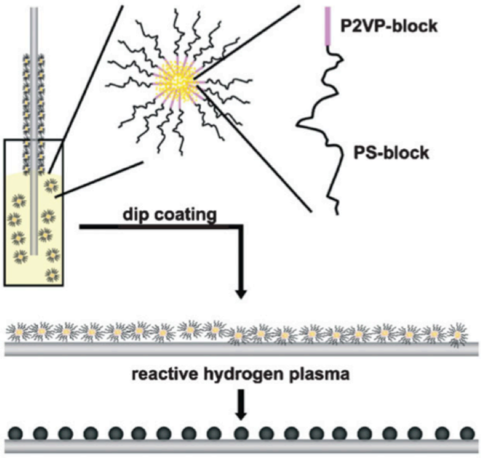

Figure 15 Deposition of hexagonally arranged gold nanoparticles on glass surfaces by dip-coating. A clean glass surface is immersed into the gold-loaded micellar solution and retracted with a defined velocity. The micelles adsorb to the surface and self-assemble in a hexagonal pattern. Reactive hydrogen plasma then removes the micellar shell and incorporated $AuCl_4^-$ -ions are reduced to form particles of elemental gold. (image: (Aydin, 2009))

The distance between the gold nanoparticles is dependent on several factor, e.g. the radius of the micelles and thus the size of the diblock copolymers used, the micellar concentration during the dip-coating process or the film height. The latter is defined by the retraction speed of the substrate from the solution. By continuously changing the retraction speed over a defined distance during dip-coating of a single substrate, gradient distances between the particles can be realized.

Thus, BCML allows the deposition of gold nanoparticles with not only homogeneous spacings, but also with gradient distances on the same substrate. These nanoparticles can be used as anchoring points for site-directed protein immobilization.

4.4.2 Co-functionalization of nanopatterned surfaces

Nanopatterned surfaces generated with BCML are highly suitable for dual functionalization with biomolecules (Figure 16). Since most synthetic biomolecules are

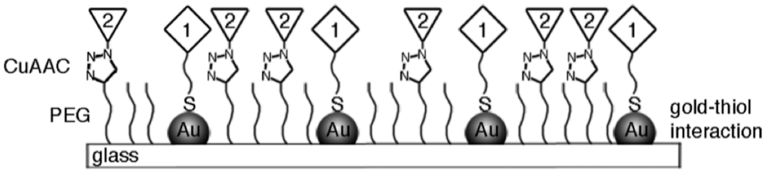

Figure 16 Dual functionalization of nanopatterned surfaces. Gold nanoparticles are functionalized with thiol chemistry (1), whereas the area between the gold particles is functionalized with copper(I)-catalysed azide alkyne cycloaddition on PEG-alkyne (2). (image: (Schenk, 2014))

available with a hexa-histidine-tag (His$_6$-tag), these surfaces can be used for orthogonal presentation of nitrilotriacetic acid (NTA), which forms complexes with His$_6$-tagged proteins with the aid of divalent cations.

In the first step of the functionalization process, the area between the gold nanoparticles is coated with PEG-alkyne (Figure 17a). The PEG layer prevents unspecific protein adsorption to the surface and therefore minimizes nonspecific interactions between the glass and cells (Blümmel et al., 2007). PEG-alkyne additionally contains terminal alkyne groups to which NTA-azide can be linked by using the copper(I)-catalysed azide alkyne cycloaddition (Figure 17b).

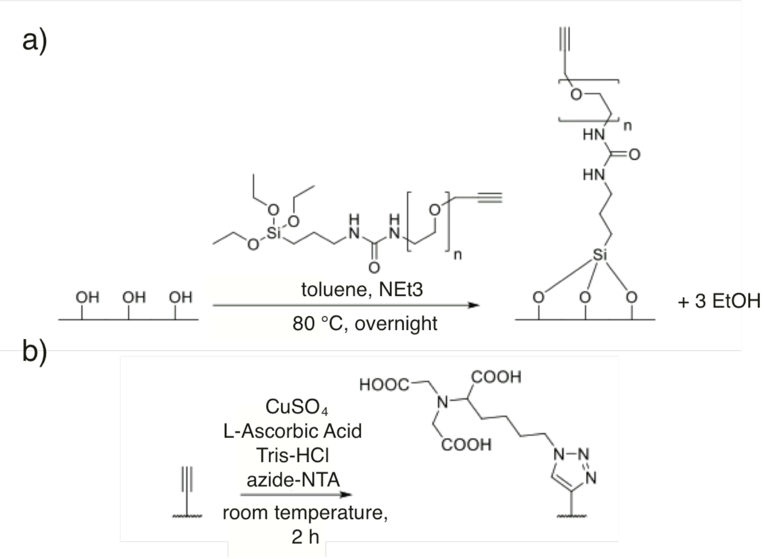

Figure 17 Functionalization approach of the glass surface. a) Immobilization of PEG-alkyne by silane group on glass substrates. b) Subsequent functionalization of PEG-alkyne with azide-NTA using the copper(I)-catalysed azide alkyne cycloaddition, also known as a click reaction.

In the second step, gold nanoparticles are functionalized using thiol chemistry. Incubating nanopatterned surfaces with thiol-(NTA) (Figure 18) leads to the formation of a covalent bond between gold and sulphur and thereby links NTA to the gold nanoparticles.

NTA present on both gold nanoparticles and on the passivated area allows anchorage of His$_6$-tagged proteins. NTA is a chelating agent that is widely used for selectively binding

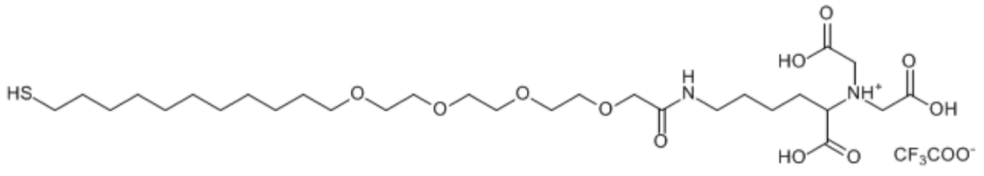

Figure 18 Structure of thiol-NTA (SH-(CH$_2$)$_{11}$-EG$_3$-NTA) used for functionalizing gold nanoparticles.

recombinant His_6-tagged proteins. This linkage requires divalent cations. Most often, Ni^{2+} is used, but also Co^{2+}, Cu^{2+} or Zn^{2+} are suitable mediators (Block et al., 2009). Nonetheless, the affinity between NTA and His_6-tags mediated by divalent cations is usually very low; the binding is kinetically labile and therefore undergoes fast ligand exchanges (Wegner & Spatz, 2013). These drawbacks can be overcome by using Co^{3+} ions as the mediator for ligand interaction, as published by Wegner et al. (Wegner & Spatz, 2013). The formed complex is highly stable and inert to ligand exchange. Since the formation of Co^{3+} complexes is very slow, it is recommended to use an indirect preparation method, in which the complex with the divalent ion is formed and subsequently oxidized, e.g. by incubation with H_2O_2 (Wegner & Spatz, 2013).

Thus, combining BCML and thiol chemistry with PEG-alkyne passivation and click reaction can be used for site-specific presentation of NTA. Using Co^{3+} as the complex-mediating ion between NTA and His_6-tagged proteins realises the fabrication of surfaces that present biomolecules that are stably bound. Nonetheless, for orthogonal site-specific protein immobilisation to surface-presented NTAs, the order of the functionalization steps need to be chosen very carefully.

5 Materials and Methods

This chapter describes surface functionalization methods to mediate cell adhesion, a prerequisite for RICM imaging. The isolation and *in vitro* differentiation of whole CD4$^+$ T cell populations are explained, including the extraction of T cell subpopulations. Also, the fabrication and characterisation of immobilized protein gradients with nanometre precision that mimic native homing routes is explained. Parameters for RICM and life cell imaging are given and methods and algorithms used for image analysis and data evaluation are depicted.

5.1 Surface functionalization

This section includes the description of different approaches for generating homogeneous surface coatings. They were used for adhesion screenings in order to determine which method is best suitable for mediating T cell adhesion to the surface. The fabrication of nanostructured (gradient) surfaces is explained. The co-functionalization of these surfaces is described and characterisation methods that prove the specificity of the functionalization approach are explained.

5.1.1 Surface pre-treatment

Glass slides (20 x 20 mm, Carl Roth GmbH, Karlsruhe, Germany) were cleaned with piranha solution, a 1:3 mixture of hydrogen peroxide (30 %, p.a., Merck KGaA, Darmstadt, Germany) and sulphuric acid (95 %, p.a., Carl Roth GmbH, Karlsruhe, Germany). After a minimum of 1 hour, glass slides were washed extensively in MiliQ water, ultrasonicated and dried under a stream of nitrogen. The surfaces were then clean and highly hydrophilic since all adsorbed organic compounds were oxidized.

5.1.2 Homogeneous coating of glass surfaces

Adsorption of proteins on surfaces

For protein adsorption, recombinant human ICAM-1 (R&D Systems GmbH, Abingdon, UK) was diluted in PBS to a concentration of 3 μg/ml. Collagen-1 (Life Technologies GmbH, Darmstadt, Germany) was diluted in PBS to 10 μg/ml. Protein solutions were added onto clean glass slides and incubation followed for 2 hours at 37 °C. Surfaces were carefully washed with PBS.

Peptide immobilization

For anchorage of peptides onto glass surfaces, glass slides were first passivated with either PEG-alkyne or PEG for negative control. Following, different azide-containing peptides were coupled onto the substrates by a copper(I)-catalysed azide alkyne cycloaddition, also known as click reaction.

Surface passivation

Briefly, cleaned glass slides were either used directly after piranha treatment or activated with oxygen plasma (TePla 100-E, PVA TePla GmbH, Munich, Germany) for 10 minutes at 0.4 mbar and 150 W. Hydrophilic glass substrates were put into a Schlenk flask containing 20 ml of dry toluene (p.a., dried over molecular sieves (3 Å), Carl Roth GmbH, Karlsruhe, Germany) under nitrogen atmosphere. 0.25 mM PEG-alkyne ($(CH_3CH_2O)_3$Si-PEG$_{3000}$-alkyne) or PEG ($(CH_3CH_2O)_2$Si-PEG$_{2000}$-$OCHH_3$) provided by F. Schenk (AK Spatz, Biophysical Chemistry, University of Heidelberg, Germany) were added, also a catalytic amount of triethylamine (p.a., Fluka, Buchs, Germany). Reaction was left at 80 °C over night under nitrogen atmosphere for at least 16 hours.

For removing physisorbed PEG, substrates were immersed into ethyl acetate (p.a., Merck, Darmstadt, Germany) and put into an ultrasonic bath for 5 minutes, followed by further 5 minutes of ultrasonication in fresh ethyl acetate and then in methanol (p.a., Merck, Darmstadt, Germany). Surfaces were then dried in a stream of nitrogen.

Coupling of azide-peptides to alkyne-PEG by copper(I)-catalysed cycloaddition

Azide-containing peptides were then covalently coupled to the PEG-alkyne layer by using the copper(I)-catalysed azide alkyne cycloaddition, also known as click reaction. For this, substrates were incubated with a freshly prepared solution of 100 mM L-ascorbic acid

(Sigma-Aldrich, Steinheim, Germany), 100 mM Tris HCl (pH 9.5), 150 μM azide-peptide and 1 mM $CuSO_4$ for 2 hours at room temperature under moisture atmosphere. Samples were then washed with 50 mM EDTA (Sigma-Aldrich, Steinheim, Germany) for removing Cu^{2+} ions. After washing with MiliQ water substrates were dried under a stream of nitrogen.

One of the peptides used here was the adhesion-promoting peptide sequence of Laminin, IKVAV (purchased from Peptide Speciality Laboratories GmbH, Heidelberg, Germany) that possessed an azide group on the N-terminally linked lysine.

Surfaces were also functionalized with cyclic RGD-azide (c-RGD) and linear azide-GRGDSP (l-RGD). RGD is the adhesion-mediating domain of fibronectin.

5.1.3 Protein co-immobilization on nanopatterned surfaces using BCML

Preparation of gold-loaded micellar solution

The diblock copolymer Polystyrene(1056)-*block*-poly(2-vinylpyridine)(495), short PS(1056)-b-P2VP(459), was dissolved in toluene (p.a., Merck KGaA, Darmstadt, Germany) with concentrations of 4.8 mg/ml at room temperature for a minimum of 24 h on a magnetic stirrer. Solid hydrogen tetrachloroaurate(III) trihydrate ($HAuCl_4*3H_2O$, Sigma-Aldrich, Steinheim, Germany) was weighted out into a clean scintillation vial that were previously filled with argon gas in order to prevent salt's reactions with air humidity.

The amount of added $HAuCl_4$ was calculated via following formula:

$$m(\mathrm{HAuCl_4} * 3\mathrm{H_2 0}) = \frac{\mathrm{m(Polymer)} * \mathrm{L} * \mathrm{M(HAuCl_4} * 3\mathrm{H_2O)} * 495}{\mathrm{M(Polymer)}}$$

L is the desired loading rate (ratio of $AuCl_4^-$ to P2VP units, here $L = 0.3$); m depicts the weight of the used polymer, the molecular weight M of $HAuCl_4*3H_2O$ is 393.8 g/mol. Diblock copolymer solution was added and stirred for 24 h under light protection.

Preparation of nanostructured surfaces

Gold nanopatterns were deposited on glass surfaces by dip coating. For this, a custom made dipping device was employed, which was connected to an adjustable power supply (Laboratory power supply unit series EA-PS 3032-10, Elektro-Automatik, Viersen, Germany). This power supply unit was connected to a terminal block (I/O – terminal block, CB 68LP, National Instruments, Munich, Germany), which was connected to a computer equipped with a PCI controller card (PCI-6052E Multifunctional I/O and NI DAQ board PCI/PXI/1394 Bus Computers, National Instruments, Munich, Germany). To control the voltage of the power supply unit the Software LabView (Version 7.0, National Instruments, Munich Germany) was used.

This setup allows to monitor the speed of surface retraction from solution during the dip coating process. Since retraction velocity influences particle distance, homogenous and gradient patterning over defined distances could be generated.

Prepared gold loaded micellar solution PS(1056)-b-P2VP(495) was filled into a glass container (22 mm diameter, Schott Duran Group, Wertheim, Germany). A cleaned glass surface was clamped into the custom made dipping device and two third of it was immersed into the solution at a constant speed of 30.9 mm/min (15 V).

For nanopattern gradient deposition, the surface was retracted for 3 mm at a high constant speed of 40 mm/min in order to obtain a homogeneous nanopattern with low interparticle distance (Figure 20 (I)). The retraction velocity was following decelerated to 8 mm/min over a gradient length of 2 mm (Figure 20(II)). The substrate was then retracted from solution at a low constant speed of 8 mm/min for obtaining a homogeneous nanopattern with large interparticle distances (Figure 20(III)).

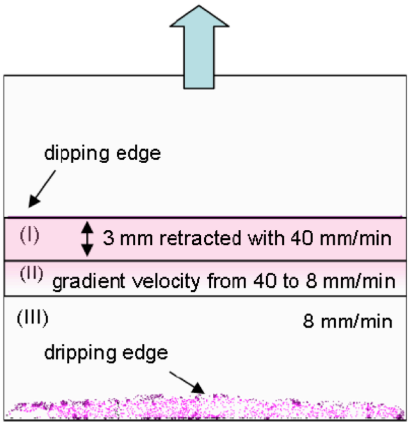

Figure 19 Scheme of obtaining a nanopatterned gradient surface via dip-coating. A cleaned glass cover slip is immersed into the micellar solution. I: The substrate is retracted at a constant velocity over a distance of 3 mm (homogenous nanopattern with low interparticle distance). II: Negative acceleration leads to increased interparticle distance (gradient nanopattern). III: The surface is retracted from solution at low constant velocity (homogenous nanopattern with high interparticle distance). (adopted from (Hirschfeld-Warneken et al., 2008))

For homogeneous nanopatterning, the surface was retracted from solution at constant speed of 8 mm/min or 40 mm/min for obtaining high or low interparticle spacing, respectively.

Glass surfaces were dried above the solution’s surface for 1 minute until the entire solvent on the glass surfaces had evaporated and following exposed to hydrogen plasma for 45 min at 0.4 mbar and 600 W (PVA TePla, Plasma System 210, TePla GmbH, Munich, Germany).

Surface passivation and co-functionalization

Nanopatterned surfaces were passivated with PEG-alkyne as described above. After removal of physisorbed PEG, surfaces were dried in a stream of nitrogen. Subsequently, surfaces were co-functionalized with ICAM-1 and CCL25. For all steps, incubation was performed in a moisture chamber at room temperature.

For functionalizing the PEGylated areas between the gold nanoparticles, NTA-azide was coupled to PEG-alkyne by using the copper(I)-catalysed azide alkyne cycloaddition, also known as click reaction,(Momburg et al., 1993) as described above, using 125 μM NTA-azide. Samples were then incubated with 100 mM $CoCl_2$ for 15 minutes and washed with MiliQ water. Following, surfaces were incubated with 5 μg/ml mouse ICAM-1 His_6 (Sino Biological, Beijing, China) diluted in 50 mM Tris buffer supplemented with 300 mM NaCl (pH 7.4). After 45 minutes incubation, samples were washed with Tris buffer and incubated for 30 minutes with 10 mM H_2O_2 (Sigma-Aldrich, Steinheim, Germany) diluted in Tris buffer. Surfaces were then carefully washed with Tris buffer.

For subsequent functionalization of gold nanoparticles, surfaces were incubated with thiol-NTA ($SH\text{-}(CH_2)_{11}\text{-}EG_3\text{-}NTA$, Prochimia, Sopot, Poland) for 20 minutes, washed with PBS and incubated for 15 minutes with 100 mM $CoCl_2$. After washing with PBS, His_6-tagged mouse CCL25 (Bioclone Inc., San Diego, USA) was diluted to a concentration of 10 μg/ml in PBS and given onto surfaces. After 45 minutes incubation, samples were washed and incubated with 10 mM H_2O_2 for 30 minutes and washed with PBS.

5.1.4 Characterization of co-functionalized surfaces

SEM (Scanning Electron Microscopy)

From each dipping batch a randomly selected surface was imaged with SEM for determining interparticle distance and order parameter

The sample was covered with a carbon layer using a sputter coater (Leica EM ACE200, Leica Microsystems, Wetzlar, Germany). Samples were imaged with a LEO 1530 field emission scanning electron microscope (FE-SEM) equipped with a Schottky cathode (LEO GmbH, Oberkochen, Germany). The chamber pressure during the imaging process was approximately < 5*10-6 mbar, the accelerating voltage was set at 5 kV.

SE micrographs of the nanopatterned surfaces were analysed using the freeware Fiji/ImageJ software (version 2.0.0-rc-30/1.49s) and the plug-in written by Dr. Philipp Girard, which calculates the average distance between particles and their nearest neighbours and determines the global order parameter according to Kansal et al. (Kansal, Truskett, & Torquato, 2000).

Bio-functionality studies of ICAM-1

To test whether oxidation of ICAM-1 influences the bio-activity of this protein, the murine T cell hybridoma cell line 3B11 (provided by J. Deeg, AK Spatz, Biophysical Chemistry, University of Heidelberg, Germany) was used. (Hosseini et al., 2009; Momburg et al., 1993) Surfaces were homogeneously coated with mouse ICAM-1 (Sino Biological, Beijing, China) as described above. Also, glass surfaces were passivated with PEG-alkyne as described, coupled with azide-NTA and functionalized with His_6-ICAM-1, using either Ni^{2+} (incubation with 100 mM $NiCl_2$) or Co^{3+} as complex-mediating ion. Also, surfaces functionalized with Co^{3+}/His_6-ICAM-1 were incubated in 250 mM imidazole (Sigma-Aldrich, Steinheim, Germany) in PBS and washed with 50 mM Tris buffer supplemented with 300 mM NaCl (pH 7.4). 3B11 T cells were seeded on respective surfaces and imaged with RICM. As negative control, surfaces passivated with PEG were used.

Immunogold labelling and SEM imaging

Passivated surfaces were functionalized with thiol-NTA, Co^{2+} and His_6-tagged mouse CCL25 and oxidized as described above. Surfaces were incubated with 1 % BSA (Biomol GmbH, Hamburg, Germany; filtered with 0.22 μm syringe filters, Carl Roth GmbH, Karlsruhe, Germany) solution in PBS for blocking unspecific protein binding. After washing with PBS, samples were incubated with anti-mouse CCL25 monoclonal antibody (rat IgG2A clone #89827, R&D Systems, Wiesbaden-Nordenstadt, Germany) at a concentration of 10 μg/ml for 45 minutes, followed by incubating with anti-rat IgG (whole molecule)-gold antibody (produced in goat, Sigma-Aldrich, Steinheim, Germany) at 1:10 dilution for 1 hour. For control, surfaces were functionalized in the same way, except CCL25 incubation.

SEM imaging of immunogold labelled surfaces and control was performed as described above.

AFM (Atomic Force Microscopy)

Passivated surfaces were functionalized with thiol-NTA, Co^{2+} and His_6-tagged mouse CCL25 as described above, followed by an oxidation step with H_2O_2. For negative control, passivated surfaces were used. AFM measurements of the surfaces were carried out in air and in intermitted contact mode with Nanowizard (JPK Instruments AG, Berlin, Germany).

QCM (Quartz-Crystal Microbalance) measurements

To prove ICAM-1 binding to surfaces, QCM measurements were performed, using sensors from Q-Sense (Västra Frölunda, Sweden) and a Q-Sense E4 System. The flow rate was set on 10 μl/min and measurements were performed at room temperature.

In the first approach, silica crystals that have been functionalized with PEG-alkyne and subsequently coupled with NTA-azide using the copper(I)-catalysed azide alkyne cycloaddition as described before were equilibrated with Tris buffer (50 mM, pH 7.4, supplemented with 300 mM NaCl). Then, they were incubated with 100 mM $CoCl_2$, followed by a washing step with Tris buffer. Sensors were then incubated with 5 μg/ml His_6-tagged GFP (provided by F. Schenk, AK Spatz, Biophysical Chemistry, University of Heidelberg, Germany) diluted in Tris buffer. Subsequently, surfaces were incubated with 10 mM H_2O_2 (Sigma-Aldrich, Steinheim, Germany) for 30 minutes and washed with Tris buffer. Following, 250 mM imidazole (Sigma-Aldrich, Steinheim, Germany) was added and crystals were again rinsed with Tris buffer.

In the second approach, gold crystals that have been functionalized with thiol-NTA as described above were used. After equilibration with Tris buffer, they were incubated with 100 mM $CoCl_2$, followed by a washing step with Tris buffer. Sensors were then incubated with 5 μg/ml mouse ICAM-1 His_6 (Sino Biological, Beijing, China) diluted in Tris buffer. Subsequent steps were carried out as described above.

Fluorescent labelling and imaging

Co-functionalized surfaces were incubated with 1 % BSA (Biomol GmbH, Hamburg, Germany; filtered with 0.22 μm syringe filters, Carl Roth GmbH, Karlsruhe, Germany) solution in PBS for blocking unspecific protein binding.

For fluorescent labelling of immobilized CCL25, surfaces were incubated with anti-mouse CCL25 monoclonal antibody (rat IgG2A clone #89827, R&D Systems, Wiesbaden-Nordenstadt, Germany) at a concentration of 10 μg/ml for 45 minutes. After blocking with

1 % BSA, samples were incubated with 10 μg/ml goat anti-rat IgG secondary antibody conjugated with FITC (Life Technologies, Darmstadt, Germany). For negative control, co-functionalized surfaces were incubated with the secondary antibody only.

For fluorescent staining of ICAM-1, surfaces were incubated with 10 μg/ml CD54 rat anti-mouse monoclonal antibody FITC conjugate (clone YN1/1.7.4., Life Technologies, Darmstadt, Germany) for 45 minutes. For control, a non-functionalized surface was blocked with 1 % BSA and incubated with this antibody in order to visualize unspecific protein binding.

Stained surfaces were washed with PBS and mounted on glass slides with Fluoromount (Sigma-Aldrich, Schnelldorf, Germany).

Fluorescently labelled surfaces were imaged with a Leica DM6000B microscope (Leica, Wetzlar, Germany) equipped with a 10 x objective.

5.2 Human T cell isolation and characterisation

This section describes the isolation of human peripheral blood monocytes (PBMCs) from human peripheral blood and subsequent expansion of T cells that were used for first adhesion experiments. Isolation of CD4$^+$ T cells by magnetic labelling is depicted. *In vitro* differentiation of whole CD4$^+$ T cell populations and monitoring of cells' differentiation state by flow cytometry is given in detail. Extraction of T cell subpopulations using magnetic labelling and fluorescent-activated cell sorting (FACS) are described.

5.2.1 Isolation of human peripheral blood mononuclear cells

Human peripheral blood was obtained from *DRK Blutspendedienste* from anonymous donors. Buffy coats were diluted at a 1:2 ratio with warm PBS (calcium free, Sigma-Aldrich, Steinheim, Germany) supplemented with 2 mM EDTA (Sigma-Aldrich, Steinheim, Germany). Diluted blood was then overlaid onto half of the volume of lymphocyte separation medium LSM 1077 (PAA Laboratories GmbH, Pasching, Germany) without mixing the two phases. Gradient centrifugation was performed at 300 g for 30 minutes at 20 °C without using the break.

After gradient centrifugation, a white layer was formed that contains peripheral blood mononuclear cells (PBMCs). These layers were harvested and diluted in PBS/EDTA. After centrifugation at 300 g for 10 minutes, another washing step followed and cells were centrifuged at 200 g for 10 minutes for removing platelets.

5.2.2 Expansion of T cells from PBMCs

Cells were cultured in RPMI 1640 medium (Life Technologies GmbH, Darmstadt, Germany) supplemented with 10 % FBS and 1 % PS at a density of $1*10^6$ cells/ml. Soluble CD3 antibody (clone OKT3, Biolegend, San Diego, USA) at a concentration of 0.05 μg/ml and CD28 antibody (clone CD28.2, BD Biosciences, Heidelberg, Germany) at a concentration of 0.5 μg/ml were added. On day 3 after isolation, medium was exchanged by fresh medium supplemented with 400 units/ml IL-2. Cell medium was replaced every 48 hours and IL-2 was added. Cells were cultured for a maximum of 10 days in total and used for adhesion experiments.

5.2.3 Isolation of $CD4^+$ T cells

Human PBMCs were isolated as described above. After removing platelets, cells were diluted in 5 ml PBS/EDTA and cell number was determined. The respective volume containing five times more cells than needed $CD4^+$ T cells was further diluted and centrifuged at 300 g for 10 minutes. The cell pellet was resuspended in 90 μl buffer (PBS/EDTA) supplemented with 0.5 % BSA (Biomol GmbH, Hamburg, Germany) per 10^7 cells.

Magnetic separation that is described in the following sections was performed using the $CD4^+$ T cell isolation kit (human), purchased from Miltenyi Biotec GmbH (Bergisch Gladbach, Germany). This included all mentioned antibody cocktails, beads, magnetic columns and magnets.

For depletion of non-$CD4^+$ T cells, cell suspension was supplemented with 10 μl $CD4^+$ T cell biotin-antibody cocktail per 10^7 cells and well mixed. Cells were then incubated at 4 °C for 5 minutes. Following, 20 μl anti-biotin microbeads per 10^7 cells were added, mixed and incubated at 4 °C for 10 minutes.

An LD column was placed in a magnet (MidiMACS) and rinsed with 2 ml buffer. Cell suspension was added and flow-through cells were collected. The column was washed twice with 1 ml buffer and flow-through cells were collected also. Non-labelled $CD4^+$ cells were counted and washed with RPMI 1640 medium (Life Technologies GmbH, Darmstadt, Germany) supplemented with 10 % FBS and 1 % penicillin/streptomycin (PS).

For purity control (see section 5.2.5), $2*10^5$ cells were diluted in culturing medium to a concentration of $1*10^6$ cells per ml and seeded in a 96 well plate. Cells were cultured over night but not more than 18 hours at 37 °C and 5 % CO_2 atmosphere.

5.2.4 Inducing and monitoring $CD4^+$ T cell differentiation

For inducing differentiation using Dynabeads® (Dynabeads® human T-activator CD3/CD28 for T cell expansion and activation, Life Technologies GmbH (Invitrogen), Darmstadt, Germany), remaining $CD4^+$ T cells were supplemented with 25 μl/10^6 cells/ml T cell activation beads according to manufacturer's protocol. Differentiation with MACSiBeads, (T cell activation/expansion kit, human, Miltenyi Biotec GmbH) was performed adding 12.5 μl beads per $2.5*10^6$ cells according to manufacturer's protocol.

Cells were cultured at 37 °C and 5 % CO_2 atmosphere.

The differentiation states of the $CD4^+$ T cell populations were determined by flow cytometry within 24 hours, also on day 3 and on day 7 of culturing. For this, either CD45RA or CD45RO antibody or their corresponding isotype controls (see **Table 5-1**) were added to the respective amount of cells. Volumes were filled up to 300 μl with RPMI/PS and cells were incubated in the dark for 30 minutes on ice.

Cells were washed and centrifuged at 300 g for 10 minutes. Samples were resuspended in RPMI/PS to a concentration of $2.5*10^5$ cells/ml.

Flow Cytometry was carried out in the "Zentrum für Molekulare Biologie Heidelberg" FACS Facility using the 3-laser BD FACSCantoTM II flow cytometer (BD Biosciences, Franklin Lakes, USA). For each sample, $1*10^5$ cells were analysed.

Table 5-1: Cell staining for monitoring differentiation by flow cytometry. Given are antibodies and corresponding isotype controls, used reagent volumes and numbers of incubated cells. All antibodies were purchased from eBioscience, San Diego, USA.

Surface marker	Isotype controls and antibodies	Volume	Cell number
Control	-	-	$1*10^5$
Isotype controls	mouse IgG2b kappa isotype control FITC (clone: eBMG2b)	2.5 µl	$5*10^4$
	mouse IgG2a kappa isotype control FITC (clone: eBM2a)	2.5 µl	
CD45RA and CD45RO	anti human CD45RA FITC (mouse IgG2b, kappa) (clone: HI100)	2.5 µ	$5*10^4$
	anti human CD45RO FITC (mouse IgG2a, kappa) (clone: UCHL1)	2.5 µl	

5.2.5 Purity control using flow cytometry

Isolated CD4$^+$ T cells were analysed for their purity by flow cytometry. For this, cells were stained with antibodies for CD4, CD3 or respective isotype controls (see **Table 5-2**). Volumes were filled up to 300 µl with RPMI/PS and cells were incubated in the dark for 30 minutes on ice.

Cells were washed, centrifuged at 300 g for 10 minutes and resuspended in RPMI/PS to a concentration of $2.5*10^5$ cells/ml. Flow cytometry was carried out as described above.

Table 5-2: Cell staining for purity control of the isolated T cell population by flow cytometry. Displayed are antibodies and corresponding isotype controls, used reagent volumes and numbers of incubated cells. All antibodies were purchased from eBioscience, San Diego, USA.

	Isotype Controls and antibodies	Volume	Cell number
Control	-	-	$1*10^5$
Isotype controls	mouse IgG1 K isotype control APC (clone: P3.6.2.8.1) mouse IgG1 K isotype control PE (clone: P3.6.2.8.1)	2.5 μl 2.5 μl	$5*10^4$
CD3 and CD4	anti human CD3 APC (mouse IgG1, kappa) (clone: SK7) anti human CD4 PE (mouse IgG1, kappa) (clone: RPA-T4)	2.5 μl 2.5 μl	$5*10^4$

5.2.6 Isolation of CD4$^+$ CD25$^-$ T cells

CD4$^+$ T cells were isolated from human peripheral blood as described above. For T cell subset isolation, CD4$^+$ T cells were depleted of cells expressing CD25 by magnetic labelling. This surface protein is expressed on regulatory T cells (Baecher-Allan, Brown, Freeman, & Hafler, 2001) and also resting memory cells (Triplett et al., 2012).

For magnetic labelling of CD25$^+$ cells, CD4$^+$ T cells were centrifuged at 300 g for 10 minutes and the cell pellet was resuspended in 90 μl buffer per 10^7 initial cell number. 10 μl CD25 microbeads per 10^7 cells were added and the suspension was incubated at 4 °C in the dark. After 15 minutes, 2 ml buffer were added and cells were washed, followed by centrifugation. Cells (< 10^8) were resuspended in 500 μl buffer.

Next, CD25$^+$ cells were depleted. An MS column was placed in a magnet (MiniMACS) and rinsed with 0.5 ml buffer. Cell suspension was added and flow-through cells (CD4$^+$ CD25$^-$) were collected. The column was washed three times with 0.5 ml buffer and flow-through cells were collected also. CD25$^+$ T cells were now trapped in the column.

For enhancing T cell population purity, a second column run was performed. The first column was removed from the magnet and replaced by a new MS column that has previously been rinsed with 0.5 ml buffer. The column containing CD25$^+$ T cells was held over the new column, 1 ml buffer were added and magnetically labelled cells were immediately flushed out by firmly pushing a plunger into the column. The column was washed three times with 0.5 ml buffer and flow-through cells were collected also.

5.2.7 Naïve, central memory and effector memory T cell isolation

CD4$^+$ CD25$^-$ T cells were then separated into naïve, effector memory and central memory cells by FACS. Cells were stained with antibodies for CD62L and CD45RA or respective isotype controls (see **Table 5-3**). For incubation, volumes were filled up to 300 μl (isotype control) and 700 μl (protein staining), respectively. Incubation was performed on ice for 30 minutes in the dark. Cells were washed, centrifuged at 300 g for 10 minutes and resuspended in RPMI/PS to a concentration of 2.5*10^5 cells/ml.

With a 4-laser BD FACSAriaTM IIIu (BD Biosciences, Franklin Lakes, USA), 10^5 cells were analysed and the percentage of naïve (CD45RA$^+$ CD62L$^+$), effector memory (CD45RA$^-$ CD62L$^-$) and central memory (CD45RA$^-$ CD62L$^+$) T cells was determined. Cells were then separated into respective subpopulations according to CD45RA and CD62L expression. The nozzle size was set on 100 μm.

Table 5-3: Staining for cell sorting. Given are antibodies and corresponding isotype controls, used reagent volumes and number of incubated cells. All antibodies were purchased from eBioscience, San Diego, USA.

	Isotype controls and antibodies	Volume	Cell number
Control	-	-	1*10^5
Isotype controls	mouse IgG1 K isotype control APC (clone: P3.6.2.8.1) mouse IgG2b kappa isotype control FITC (clone: eBMG2b)	2.5 μ 2.5 μl 1	5*10^4
CD62L and CD45RA	anti human CD62L APC (mouse IgG1, kappa) (clone: DREG56) anti human CD45RA FITC (mouse IgG2b, kappa) (clone: HI100)	5 μl 5 μl	<10^8

5.3 Imaging, image analysis and data evaluation

This section describes the setup for RICM and image analysis, including quantification of adhesive parameters and calculation of fractal dimensions. Algorithms used for data clustering and classification are also depicted. Also, parameters for life cell imaging and migration analysis of T cells are given.

5.3.1 Seeding human T cells on ICAM-1 coated surfaces and RICM imaging

Surface preparation and cell seeding

Glass surfaces were cleaned as described in 5.1.1. For imaging human T cell subsets, small volumes for cell seeding were needed. This was realized by a self-made stamp, which was prepared from polydimethylsiloxan (PDMS, Sigma-Aldrich, Steinheim, Germany). It contained four holes with a diameter of 0.5 cm each. This stamp was glued onto a glass surface and this setup was fixed in a petri dish with Twinsil (Picodent, Wipperfürth, Germany).

For imaging *in vitro* differentiated CD4$^+$ T cells, clean glass surfaces were glued to Nunc^{TM} Lab-Tek^{TM} Chamber (8 wells, 0.8 cm^2/well, Sigma-Aldrich, Steinheim, Germany) with Twinsil (Picodent, Wipperfürth, Germany).

Prepared samples were exposed to UV light for 30 minutes for sterilization. 12 μg/ml recombinant ICAM-1 (R&D Systems GmbH, Abingdon, UK) in sterile PBS were added to the surfaces and surfaces were incubated over night at 4 °C.

Human T cells were washed with RPMI/FBS/PS medium and centrifuged at 300 g. Cells were seeded into each small well at a density of 50 – 70 $*10^4$ cells/cm^2 and allowed to adhere for 30 minutes before imaging with RICM.

RICM imaging

The RICM setup has been implemented on an inverted microscope Olympus IX71 (Olympus, Münster, Germany) equipped with an antiflex 63x oil immersion objective (NA 1.25, NeofluarAntiflex, Zeiss, Jena, Germany). Samples were illuminated by a fiber-coupled Xenon lamp (R 100W/45C OFR, Osram, München, Germany). This was connected to the microscope through a cage system that was composed of a lens, an iris to minimize stray light, and a dichroic mirror. The RICM reflector cube located within the microscope contained a polarizer, a dichroic mirror and an analyser. A bandpass filter

(593/40; AHF Analysetechnik AG, Tübingen, Germany) filtered the orange light before imaging with a 12 bit CCD camera (Orca-R2; Hamamatsu, Hamamatsu City, Japan). A custom-built light protection system covered the cage system to ensure high contrast and good image quality. To allow life cell imaging, the microscope was enclosed in a heated and custom-built air-humidified chamber (37 °C, 5 % CO_2 atmosphere).

5.3.2 Extraction of adhesion parameters from RICM images

Image segmentation

RICM images were cropped to a size of 320 x 320 pixels with the freeware Fiji/ImageJ software (version 2.0.0-rc-30/1.49s) (Schindelin, Arganda-Carreras, Frise, & Kaynig, 2012), so each image contained only one cell.

Segmentation of RICM images was carried out with the software MATLAB (MATLAB_R2014a); the script is shown in section 10.

Briefly, a Sobel operator was applied onto an image and a binary gradient image was generated. By dilatation, segments close to each other became connected. Following, objects connected with the border were removed and holes within a contour's border were filled. Applying a diamond-structure element, the object was smoothened. Next, objects smaller than a defined size were removed. Last, the segmented image was generated by overlaying the contour onto the original image.

The original and segmented images were then compared. If the contour on the segmented image did not correspond to the cell's actual contour, the sensitivity for edge detection was adjusted.

In the algorithm, a binary image containing only the contour (in black) on white background was generated, also a segmented grey-scale image. This contained pixel values within the cell's contour of the original image, whereas the background was set on grey.

Based on the segmented image, adhesive parameters were extracted, such as area, perimeter, and eccentricity.

Calculation of adhesive cell area

A semi-quantitative method for analysing adhesive area of cells was applied (Limozin & Sengupta, 2009; Pierres, Benoliel, & Bongrand, 2002). This approach defines a threshold for pixel intensity values in the image based on minimum and maximum intensity values.

It is therefore a relative method that minimizes brightness fluctuations of the lamb and allows to distinguish between adhesive and non-adhesive areas.

Starting point for the calculation was the formula for calculating the intensity value of (x,y) on the image:

$$I(h(x,y),\lambda) = I_1 + I_2 + 2\sqrt{I_1 I_2}\cos\left(\frac{4\pi n h(x,y)}{\lambda} + \Phi\right)$$

By defining the phase shift Φ during reflection as π and the minimum and maximum intensity values, this formula can be rewritten as follows:

$$I_M = I_1 + I_2 + 2\sqrt{I_1 I_2}$$

$$I_m = I_1 + I_2 - 2\sqrt{I_1 I_2}$$

$$2I = I_M + I_m - \left[(I_M - I_m)\cos\left(\frac{4\pi n h(x,y)}{\lambda}\right)\right]$$

The wavelength used was 593 nm; the diffraction index of the medium was set to 1.3321. As a threshold value for h, 40 nm were chosen (P. F. Davies, Robotewskyj, & Griem, 1993; Pierres et al., 2002). Simplifying the equation above as indicated led the formula for threshold calculation:

$$\left(\frac{2I - I_m - I_M}{I_M - I_m}\right) = -\cos\left(\frac{4\pi n h(x,y)}{\lambda}\right)$$

$$x = \cos\left(\frac{4\pi n h(x,y)}{\lambda}\right)$$

$$I_G = \frac{I_M(1-x) + I_m(1+x)}{2}$$

For every position (x,y) on the segmented image, the pixel value was compared to the threshold pixel value. The respective position was defined as belonging to adhesive area if $I_{(x,y)} < I_G$. A new image was generated, in which these pixels were set to black. Pixels with $I_{(x,y)} > I_G$ were set to white. From these images, the percentage of adhesive cell area in respect to total cell area was determined.

Calculation of cells' excess perimeter

In order to make the perimeter independent of the area a new parameter was introduced: the excess perimeter. It describes the excess of the cell's perimeter compared to a circle's perimeter that has the same area as the cell.

The perimeter of a circle, which has the same area as the cell has, can be called hypothetical perimeter P_h. It was determined from the measured area A_m, the radius (with $A = \pi r^2$) and the perimeter of a circle (with $P = 2\pi r$):

$$P_h = 2\pi\sqrt{A_m/\pi}$$

The difference between the measured cell perimeter P_m and the hypothetical perimeter P_h was than calculated as follows:

$$\Delta P = P_m - P_h = P_m - 2\pi\sqrt{A_m/\pi}$$

Calculation of cells' eccentricity

Eccentricity describes the roundness of the cell and was also determined for adhesion characterisation. This parameter is defined as the ratio of the distance between the foci of an ellipse fitted to the cell and its major axis length.

5.3.3 Fractal analysis of RICM images

For determining the fractal dimensions (Df), the Fiji-Plugin "FracLac_2.5q" was used (Karperien, A. FracLac for ImageJ, 1999-2013)[2]. For calculating Df of contour and Df of contour/topology, box-counting methods were applied (see also section 4.3.1). Since different image types were used for fractal analysis, different box counting methods needed to be chosen.

Calculation of Df of contour was carried out on binary images containing cells' contour only. The background colour for the box counting method was set on white.

Briefly, a grid of boxes with decreasing size ε was overlaid onto the image and the number N(ε) containing object information was determined. The fractal dimension could then be calculated from the slope of the log-log-plot:

$$Df = -\lim_{\varepsilon \to 0}\left[\frac{\log\left(N_{(\varepsilon)}\right)}{\log(\varepsilon)}\right]$$

For determining the Df of contour/topology, a differential box counting method was applied. This evaluates differences in intensity values I in every box with size ε and position (i,j):

$$I_{(i,j,\varepsilon)} = I_{M(i,j,\varepsilon)} + I_{m(i,j,\varepsilon)}$$

The fractal dimension using this differential approach could than be determined as follows:

$$Df_{(differential)} = \lim_{\varepsilon \to 0}\left[\frac{\ln\left(I_{(i,j,\varepsilon)} + 1\right)}{\ln\left(\frac{1}{\varepsilon}\right)}\right]$$

---

[2] https://rsb.info.nih.gov/ij/plugins/fraclac/FLHelp/Introduction.htm

For both approaches, the standard box count was carried out using 12 grid positions. The minimum box size was set to 2 pixels, the maximal box size to 45 % of the image size.

5.3.4 Seeding and life cell imaging of mouse T cells

Surface preparation

For imaging mouse CD4$^+$ T cells, nanopatterned surfaces were passivated as described in section 5.1.3, dried and glued to a petri dish with a quadratic opening (20 x 20 mm) with Twinsil (Picodent, Wipperfürth, Germany). A self-made PDMS stamp (Sigma-Aldrich, Steinheim, Germany) surrounded the quadratic opening and thus created an incubation chamber. Surface functionalization inside this chamber was performed as described in section 5.1.3. Following, surfaces were carefully washed with sterile PBS.

Thawing and seeding of mouse CD4$^+$ T cells

Mouse CD4$^+$ T cells were provided by K. Ottmüller (AG Beilhack, Universitätsklinikum Würzburg, Germany), also CD4$^+$ T cells that were stimulated with RA *in vitro* in order to induce a GVHD phenotype. Cells were stored in liquid nitrogen. Vials (containing $4*10^5$ cells) were warmed up in a 37 °C water bath and immediately resuspended in 1 ml pre-warmed RPMI 1640 medium (Life Technologies GmbH, Darmstadt, Germany) supplemented with 10 % FBS and 1 % PS. Cell suspension was further diluted in 9 ml warm medium and centrifuged for 10 minutes at 300 g. Cells were resuspended in 200 μl medium and transferred to a 96 well plate. Cells were allowed to recover from unfreezing for 2 hours at 37 °C and 5 % CO_2.

Cell seeding and life cell imaging

Cells were washed in 4 ml warm medium, centrifuged at 300 g for 10 minutes and resuspended in 200 μl warm medium. Cells were added to the functionalized surfaces and allowed to attach to the surface for 1 hour before starting imaging.

Life cell imaging was performed with the Delta Vision RT and Spectris system (Applied Precision Inc., Issaquah, WA, USA) on an Olympus IX 71 inverted microscope (Olympus, Hamburg, Germany). The system was equipped with an incubation chamber (37 °C, 5 % CO_2 atmosphere). The objective used was 10x/0.3 Ph1 infinity/- (EC Plan-Neonfluar, Zeiss, Jena, Germany). Images were taken at a resolution of 1024 x 1024 pixels with a cooled CCD Coolsnap camera (Photometrix, Kew, Australia). Life cell imaging was performed over 1 hour with time intervals of 5 seconds.

5.3.5 Cell tracking

Migrating cells were manually tracked, using the Manual Tracking Plugin implemented in freeware Fiji/ImageJ software (version 2.0.0-rc-30/1.49s) (Schindelin et al., 2012). For this, the cell centre was chosen for representing the position of the cells. Output files were further analysed with the freeware statistic software R[3]. Directness and forward migration indices (FMI) were calculated by the freeware chemotaxis and migration tool (Ibidi, München, Germany). Fractal dimensions were determined by using the Fiji plugin “FracLac_2.5” (see section 4.3.1).

5.3.6 Data evaluation

If not else indicated, all data was evaluated with the free-ware statistic software R. It was used for all plots and calculations, including Mann-Whitney-U-Test, PCA, k-mean clustering and classification. Scatterplots were created using the package “scatterplot3d”[4] and “rgl”[5].

---

[3] R Core Team (2013). R: A language and environment for statistical computing. R Foundation for Statistical Computing, Vienna, Austria. ISBN 3-900051-07-0, URL http://www.R-project.org/

[4] Ligges, U. and Mächler, M. (2003). Scatterplot3d - an R Package for Visualizing Multivariate Data. Journal of Statistical Software 8(11), 1-20

[5] Daniel Adler, Duncan Murdoch and others (2014). rgl: 3D visualization device system (OpenGL). R package version 0.93.1098. http://CRAN.R-project.org/package=rgl

6 Results

6.1 T cell adhesion screening

Imaging cells with Reflection Interference Contrast Microscopy (RICM) allows visualising fine membrane outlines and adhesion topologies. This requires optimal adhesion of the cells to the surface. Therefore, adhesion of T cells to various surface coatings was tested in order to determine their suitability for RICM imaging.

6.1.1 T cell adhesion to surfaces functionalized with peptides

Adhesion of cells to proteins is often mediated by only a few amino acids within the protein sequence. Here, adhesion-mediating peptides were immobilized to surfaces and adhesion of *in vitro* expanded T cells was determined.

Glass surfaces were passivated with PEG-alkyne that minimizes unspecific interactions between cells and the glass (Blümmel et al., 2007). It also provides alkyne groups needed for the subsequent functionalization with azide-containing peptides. Using the copper(I)-catalysed azide alkyne reaction, the peptides were covalently linked to the surface.

This approach realizes peptide presentation on surfaces in a defined and oriented manner that is not given when surfaces are covalently coated with peptides or proteins. These surfaces are therefore highly suitable for interactional studies of cells with the immobilized peptides (Schenk et al., 2014).

For adhesion screenings peptides were chosen that correspond to sequences within proteins found in the extracellular matrix, which is an important structural element that T cells need to adhere to *in vivo* in order to reach the site of inflammation (see also section 4.1.4). One of the peptides used here was IKVAV. This is the adhesion-promoting sequence of laminin, a glycoprotein ubiquitously found in basement membranes (Tashiro et al., 1989) (Nomizu et al., 1995). The penta-peptide IKVAV used here possessed an azide group that was coupled to an N-terminally linked lysine.

The other peptide used for adhesion screenings was RGD, which is the adhesion-mediating domain of fibronectin, a glycoprotein also found in the extracellular matrix (Weeks et al., 1994). It is one of the most frequently used ligands to promote cell attachment to artificial materials, and adhesion of cells to both cyclic RGD (c-RGD) and linear RGD (l-RGD) has been shown (Pfaff, 1997) (Haubner, Gratias, & Diefenbach, 1996; Lagunas et al., 2012). Here, surfaces were functionalized with c-RGD and l-RGD that were coupled to an azide group.

For cell adhesion experiments, PBMCs were isolated from human peripheral blood and T cells were stimulated with CD3 and CD28 antibodies. After two days of culturing, soluble IL-2 was added in order to promote T lymphocyte expansion (K. A. Smith, 1988). Cells were then seeded on surfaces functionalized with IKVAV, c-RGD and l-RGD (Figure 20).

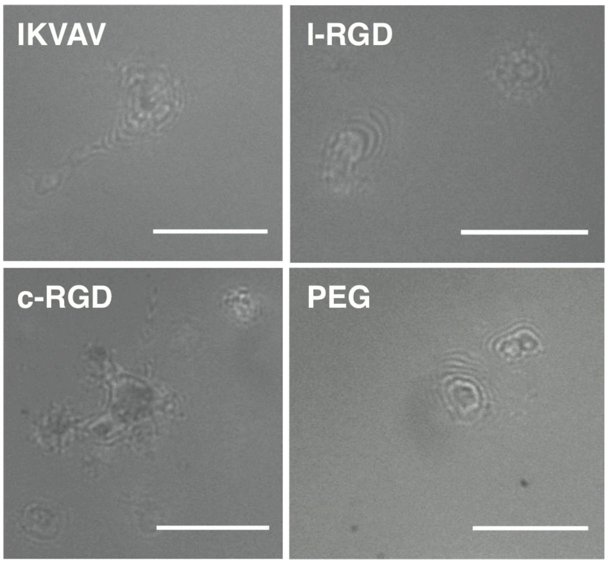

Figure 20 Adhesion of human T cells on surfaces functionalized with peptides. T cells were expanded *in vitro* from human peripheral blood mononuclear cells, seeded on functionalized surfaces and imaged with RICM. Substrates were passivated with PEG-alkyne and functionalized with peptides containing an azide group by copper(I)-catalysed azide alkyne reaction: IKVAV, the adhesion mediating sequence of laminin, and linear and cyclic RGD (l-RGD and c-RGD), which is the adhesion-promoting sequence of fibronectin. Negative control: PEG only. Scale bar: 10 μm

When seeded on control surfaces (PEG only) cells did not adhere. Here, only concentric rings were visible upon RICM imaging (Shlomchik, 2007). Compared to this, cells on IKVAV-presenting surfaces exhibited a more elongated phenotype. Nonetheless, concentric rings around a very small adhesion area were also observed. Therefore, IKVAV-presenting surfaces were not sufficient to promote T cell adhesion.

Cells were seeded on surfaces coated with either c-RGD or l-RGD. The latter mediated no adhesion, whereas improved adhesion was observed on surfaces presenting c-RGD. Here, adhesion areas were larger compared to the other conditions but cells lost surface contact very often.

Adhesion of T cells to surfaces functionalized with peptides was not sufficient for imaging with RICM and a better surface functionalization approach needed to be found.

6.1.2 T cell adhesion to surfaces functionalized with proteins

Since whole proteins promote better adhesion than small peptides (Takagi, 2004), Collagen-1 and Intracellular Adhesion Molecule 1 (ICAM-1) were used for adhesion experiments. Collagen is the main fibrous protein of the extracellular matrix and connective tissues. ICAM-1 is mainly expressed on endothelial cells and mediates T cell adhesion, which is associated with cell spreading and activation of integrin LFA-1 (Porter et al., 2002; Stewart, Cabanas, & Hogg, 1996). Here, we used homogeneous protein coatings for adhesion experiments.

When T cells were seeded on surfaces coated with Collagen-1, we observed improved adhesion with a more complex adhesion topology compared to peptide-functionalized surfaces(Figure 21). Still, cells were highly mobile. On homogeneous ICAM-1 coatings, cell adhesion could be further improved, characterized by larger adhesion areas and higher proportion of surface contact area, represented by low pixel intensity values.

Since ICAM-1 showed best adhesion mediation and has a crucial role in trespassing of T cells from blood circulation into peripheral tissue, this protein was chosen for following RICM experiments.

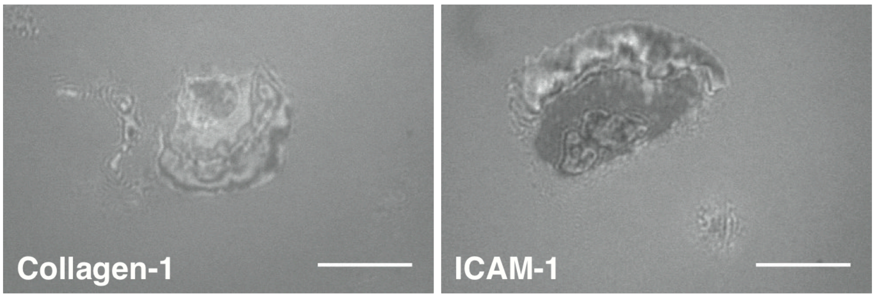

Figure 21 Adhesion of human T cells on surfaces coated with Collagen-1 and ICAM-1. Proteins were bound to surfaces by physisorption. T cells were expanded in vitro from human peripheral blood mononuclear cells, seeded onto the surfaces and imaged with RICM. Scale bar: 10 μm

6.2 Image analysis

RICM images of T cells were used for determining adhesion parameters and fractal dimensions. For this, cell contours needed to be extracted from these images by an automated segmentation algorithm.

Segmentation of images with low contrast is challenging. In RICM images, the object contains pixels with higher and lower intensity values compared to the image background and segmentation algorithms therefore need to meet special demands. In this section, image analysis for segmenting cells in RICM images is described, also the determination of adhesion parameters and fractal dimensions.

6.2.1 Image segmentation

Cells in RICM images needed to be detected and separated from the background. For this, an algorithm was applied that is based on edge detection: the Sobel operator. The steps of edge detection and image segmentation using this operator with the program MATLAB are shown in Figure 22, the algorithm is contained in section 10.

First, the original image (Figure 22a) that has been cropped to a size of 320 x 320 pixels (29.44 x 29.44 μm) was imported.

In the second step, the Sobel operator was applied. This discrete differentiation operator is based on a 2D filter mask that measures the gradient of pixel values on every pixel position and performs Gaussian smoothing at the same time. A binary gradient image was then generated (Figure 22b). On pixel positions where the change of intensity values on the original image was highest, the pixel values in the gradient image became 1 (white). Minor changes of intensity values on the original image were assigned to 0 (black) in the gradient image. The algorithm allows adjusting the represented gradient strength by defining a threshold.

In the third step, the gradient image underwent a dilatation step (Figure 22c). Segments close to each other became connected by applying a mask to the image. This changed pixels' value from 0 to 1 if at least one of the neighbouring pixels was 1. By this, segments became larger.

In the fourth step, objects that were connected with the border were removed and holes within the object's contour were filled if necessary (Figure 22d).

Fifth, the object was smoothened by using a diamond-structure element. This removed isolated pixels and let the object appear more natural. Next, objects that were smaller than a defined size were removed (Figure 22e).

In the last step, the segmented image was generated by extracting the object's contour and overlaying it onto the original image (Figure 22f). In case of the calculated contour not being in alignment with the cell's actual contour, the sensitivity for edge detection (step 2) needed to be adjusted.

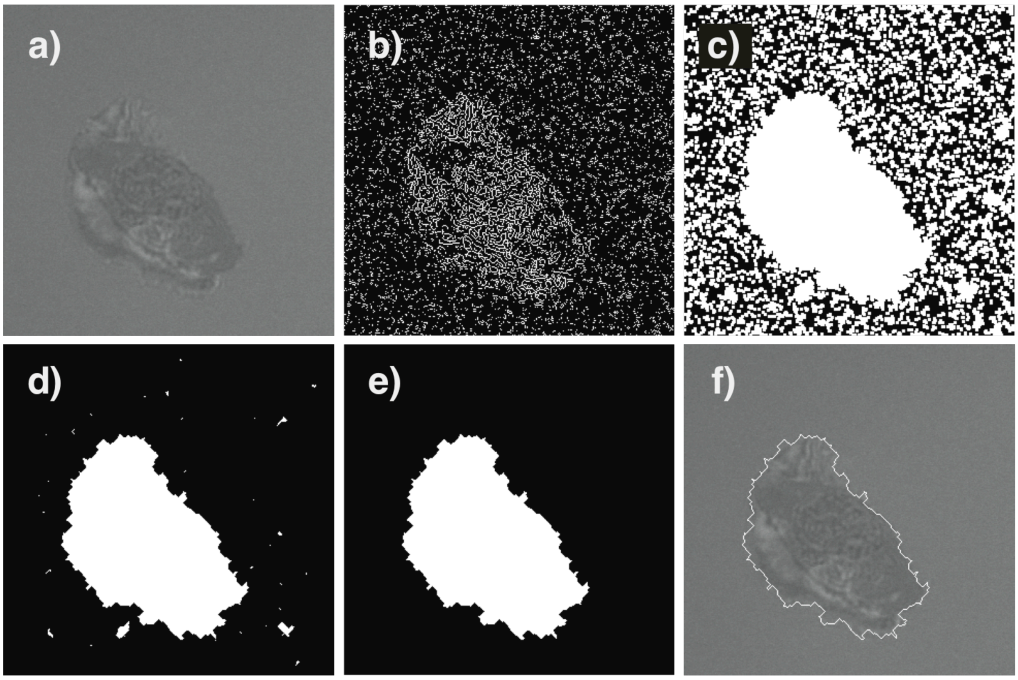

Figure 22 Processing steps of RICM image segmentation. Images were cropped to a size of 320 x 320 pixels (29.44 x 29.44 μm) and analysed with MATLAB. a) original image; b) applying the Sobel operator for intensity gradient detection; c) dilatation of image elements; d) removing objects connected with the border; e) object smoothening and deletion of small objects; f) overlaying object's contour onto the original image.

Based on the extracted cell's contour, several parameters could be calculated, such as area of the cell, its perimeter and eccentricity. Also, the minimum and maximum intensity values were determined for calculating the percentage of cell's adhesive area.

6.2.2 Calculation of adhesive cell area and fractal dimensions

Calculating the adhesive cell area was carried out by using a relative method as described by Pierres et al. (Pierres et al., 2002), which is based on the minimum and maximum intensity values within the cell's contour. Here, the intensity value that corresponds to a distance of 40 nm between the cell and the surface was set as threshold. Pixels within cell's contour with an intensity value below or above this threshold were assigned to adhesive areas or non-adhesive areas, respectively. An image was generated in which adhesive areas were coloured in black, whereas non-adhesive areas were coloured in white (Figure 23a). The percentage of adhesive cell area was calculated from ratio of black coloured pixels to the total pixel number within cell's contour.

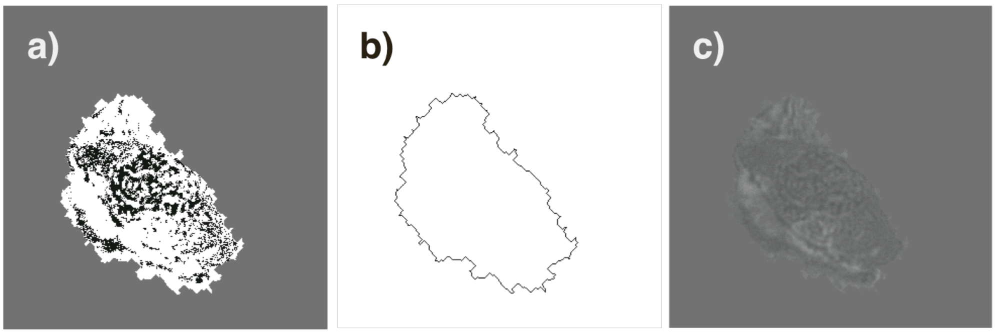

Figure 23 Images used for calculating adhesive cell area and fractal dimensions (Df). a) Adhesive cell areas: regions displaying contact areas are black, non-adhesive areas are white. b) binary image for calculating Df of contour. c) grey-scale image for calculating Df of contour/topology.

Calculation of fractal dimensions (Df) was carried out using the Fiji plugin FracLac, applying the box-counting method (see section 4.3.1).

For determining the Df of contour, binary images were generated that contained only cell's contour (Figure 23b). This parameter describes the complexity of the cell membrane.

The Df of contour/topology combines the complexities of the cell membrane with the inner topology of the adhesion area. This parameter was calculated based on gray-scale images Figure 23c), in which pixel intensities within the cell's contour correspond to the original image, whereas background pixels were coloured in grey.

6.3 *In vitro* T cell differentiation monitoring

T cell subpopulations exhibit different degrees of differentiation and effector states. These are reflected in cells' phenotypes, e.g. proliferation capacities, cytokine production and plasticity. We hypothesize that these changes affect morphological parameters of cells, such as complexity of cell membrane and adhesion patterns, which can be used for T cell subset identification. In a first step, *in vitro* differentiation of human CD4$^+$ T cell populations was monitored based on these parameters. This approach gives first insight about the suitability of RICM imaging, image evaluation and fractal analysis for distinguishing T cell subsets that have differentiated *in vivo*.

CD4$^+$ T cells were differentiated *in vitro* by using either Dynabeads® (Invitrogen) or MACSiBeads (Miltenyi Biotec GmbH). Results from flow cytometry concerning the purity of the populations and expression of differentiation markers are presented. The correlation of fractal dimensions and adhesion parameters with CD4$^+$ T cell differentiation states are shown.

6.3.1 Purity of isolated CD4$^+$ T cell populations

CD4$^+$ T cells were isolated from human peripheral blood mononuclear cells (PBMCs) by negative magnetic labelling and used for differentiation experiments. The purity of the extracted CD4$^+$ T cell population was determined with flow cytometry. For this, cells were stained with antibodies for CD3 and CD4 (Table 6-1).

Table 6-1: Expression of T cell markers. CD4$^+$ T cells were isolated from human peripheral blood and the purity of the population was analysed by flow cytometry. The percentage of cells expressing CD3 and CD4 was determined.

	CD3	CD4
donor 1	99.5 %	99.2 %
donor 2	99.1 %	98.6 %
donor 3	98.8 %	97.5 %
donor 4	98.6 %	98.5 %
donor 5	99.5 %	98.6 %

Expression of CD3 and CD4 by T cells was above 98.5 % for all donors. Only T cells from donor 3 expressed CD4 to 97.5 %.

Isolation of CD4$^+$ T cells by magnetic labelling therefore leds to a high purity of the T cell population that could be used for differentiation experiments.

6.3.2 Expression of differentiation markers CD45RA and CD45RO during *in vitro* differentiation

Incubating T cells with beads that are coated with anti-CD3 and anti-CD28 mimics *in vivo* T cell activation by antigen-presenting cells and induces T cell activation and differentiation. Naïve to memory T cell differentiation can be monitored by the expression of CD45 isoforms. The former are positive for CD45RA and negative for CD45RO, whereas memory T cells show a reciprocal expression of these surface proteins (Michie et al., 1992).

Isolated CD4$^+$ T cells were therefore incubated with beads coated with anti-CD3 and anti-CD28a. Here, beads from either Invitrogen or Miltenyi were used. Their activating capacities were compared by determining the expression of CD45RA and CD45RO of T cells on day 1, 3 and 7 after isolation with flow cytometry (Figure 24). The beads that induced best activation and therefore differentiation were used for further analyses.

T cells derived from donor 1 were incubated with Dynabeads® from Invitrogen. Expression of CD45RO that indicates differentiation increased from 30 % on day 1 to 82 % on day 3 and even to 94 % on day 7. The amount of naïve cells decreased from 49 % to 14 % within 7 days. Therefore, strongest differentiation occurred between day 1 and 3 of incubation.

When using beads from Miltenyi (donor 2 and 3), it was found that differentiation increased most between day 3 and 7 up to 91 % (donor 2) and 84 % (donor 3). Expression of CD45RA did not decrease for donor 2 within analysed time frame and only slightly for donor 3.

To confirm the results obtained with Dynabeads®, these beads were used for inducing differentiation of CD4$^+$ T cells from donor 4 and 5. It was found that CD45RO expression increased to almost 100 %, whereas expression of CD45RA decreased to 14 and 26 %, respectively.

Therefore, beads from the two suppliers were found to display different activating kinetics. Dynabeads® induced memory T cell marker expression to ~ 100 % within 7 days, which correlated with decreased expression of CD45RA. MACSiBeads were found to be less efficient in T cell differentiation induction within the analysed time frame.

Therefore, $CD4^+$ T cell populations incubated with Dynabeads® were used for RICM imaging and determination of fractal dimensions and adhesion parameters during differentiation.

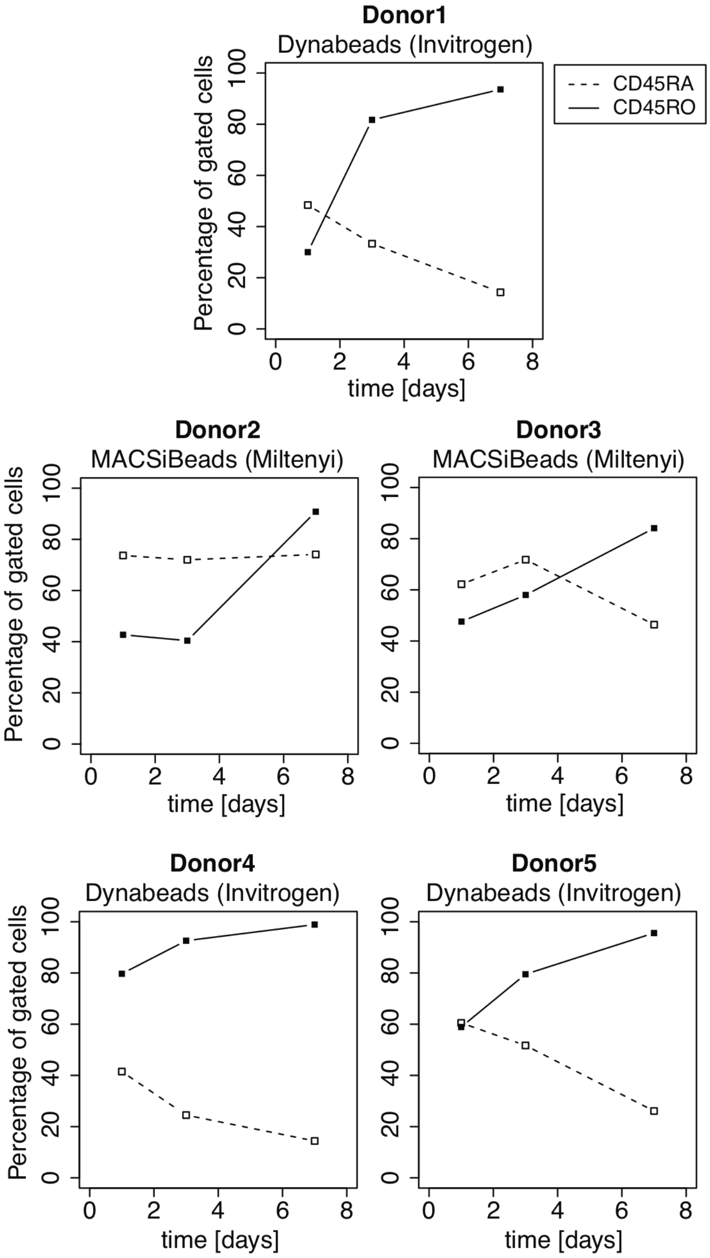

Figure 24 Expression of differentiation markers CD45RA and CD45RO of $CD4^+$ T cell populations during in vitro differentiation using different beads. T cells were isolated from peripheral blood of different donors and differentiation was induced with aCD3/aCD28 beads from Invitrogen (Donor1, Donor4 and Donor5) or Miltenyi (Donor2 and Donor3). Expression of CD45RA and CD45RO was determined on day 1, 3 and 7 of culturing with flow cytometry. On each time point, 10^5 cells were analysed.

6.3.3 Correlation of fractal dimensions with T cell differentiation

In vivo, antigen-experienced T cells display more diverse adhesion and migratory properties compared to naïve T cells (Mora & Andrian, 2006) which is expected to be reflected in their adhesion parameters and fractal dimensions. Here, it was evaluated whether fractal dimensions change during *in vitro* differentiation of T cells.

In parallel to the analysis of differentiation marker expression, CD4$^+$ T cells were seeded on ICAM-1 coated glass surfaces and imaged with RICM on day 1, 3 and 7. On day 1, only few cells adhered to the substrate and imaging a sufficient number of cells for statistical evidence displayed some difficulties. On day 3 and especially on day 7 of differentiation, adhesion of cells was highly improved. Images obtained on each time point underwent multi-step image processing and analysis (using Matlab, described in section 6.2.1) that resulted in images containing cell's contour or its contour including the inner topology. From these images, fractal dimensions (Df) of contour and Df of contour/topology were determined (see section 5.3.3).

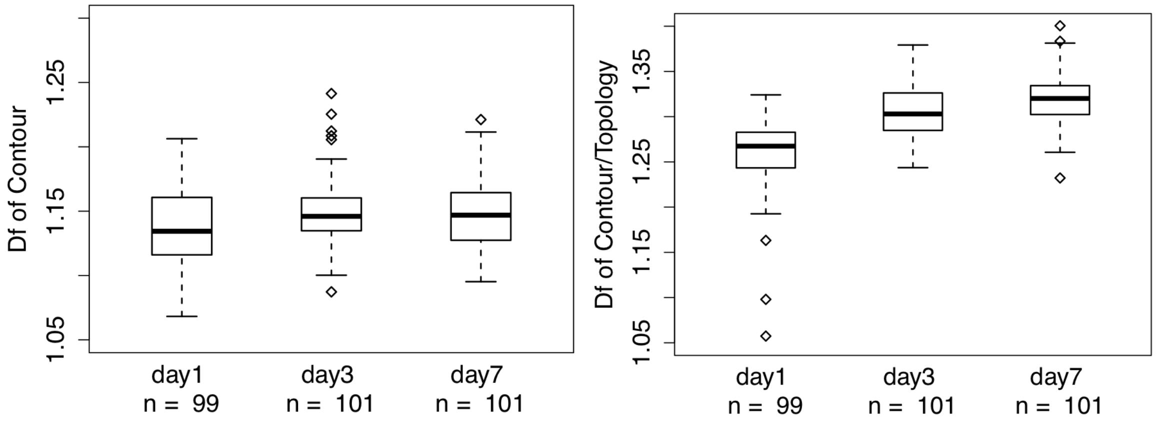

Figure 25 Change of fractal dimension (Df) of contour and contour/topology during differentiation. CD4$^+$ T cells were differentiated *in vitro* using aCD3/aCD28 beads (Dynabeads®, Invitrogen). Cells were seeded on surfaces coated with ICAM-1 and imaged with RICM on day 1, 3 and 7 after isolation. Fractal dimensions of cells were determined using MATLAB and the ImageJ Plug-in FracLac_2.5q. Results from donor 5 are exemplarily shown. The number of evaluated cells per time point is given with n.

For all samples Df of contour did not change during differentiation of CD4$^+$ T cell populations (Figure 25). Mean values were 1.14 on day 1 and 1.15 on day 3 and 7. The variances were higher on day 1 (0.001) than on the following time points (0.0006 and 0.0008, respectively).

In contrast, Df of contour/topology correlated with T cell differentiation; mean values increased from 1.26 on day 1 to 1.3 on day 3 and 7. Also, a decrease in data variance from 0.002 (day 1) to 0.0008 (day 3 and 7) was found. Mann-Whitney-U test revealed a significant difference in data variance of Df of contour/topology from day 1 to day 3 and 7 ($p << 0.0025$) and also between day 3 and day 7 ($p \sim 0.006$).

6.3.4 Correlation of adhesion parameters with differentiation

Next, the change of adhesion parameters during *in vitro* T cell differentiation was evaluated. For this, the area of the cell that adheres to the surface was determined, also the adhesive area, which was defined as the percentage of adhesion area that were closer than 40 nm to surface (see section 5.3.2).

Eccentricity, defined as the ratio of the distance between the foci of an ellipse fitted to the cell and its major axis length, describes the roundness of the cells. It was calculated by the ratio of the distance between the foci of a fitted ellipse and the cell's major axis length. Thus, values close to 0 describe a circle, values between 0 and 1 an ellipse. Another parameter, excess perimeter, describes the excess of the cell's perimeter compared to a circle's perimeter with the same area as the cell has (see also section 5.3.2).

Upon differentiation of $CD4^+$ T cells, an increase of cell area was observed (Figure 26). Also, the percentage of adhesive cell area increased with increasing differentiation.

Determined eccentricity of imaged cells showed that cells became more elongated upon differentiation, eccentricity values increased. The excess perimeter also increased significantly upon differentiation ($p << 0.0025$, determined by Mann-Whitney-U-Test).

Obtained results of both adhesion parameters and fractal dimensions were highly comparable between all *in vitro* differentiation experiments. In order to quantify this further, the variability of results depending on donors will be evaluated.

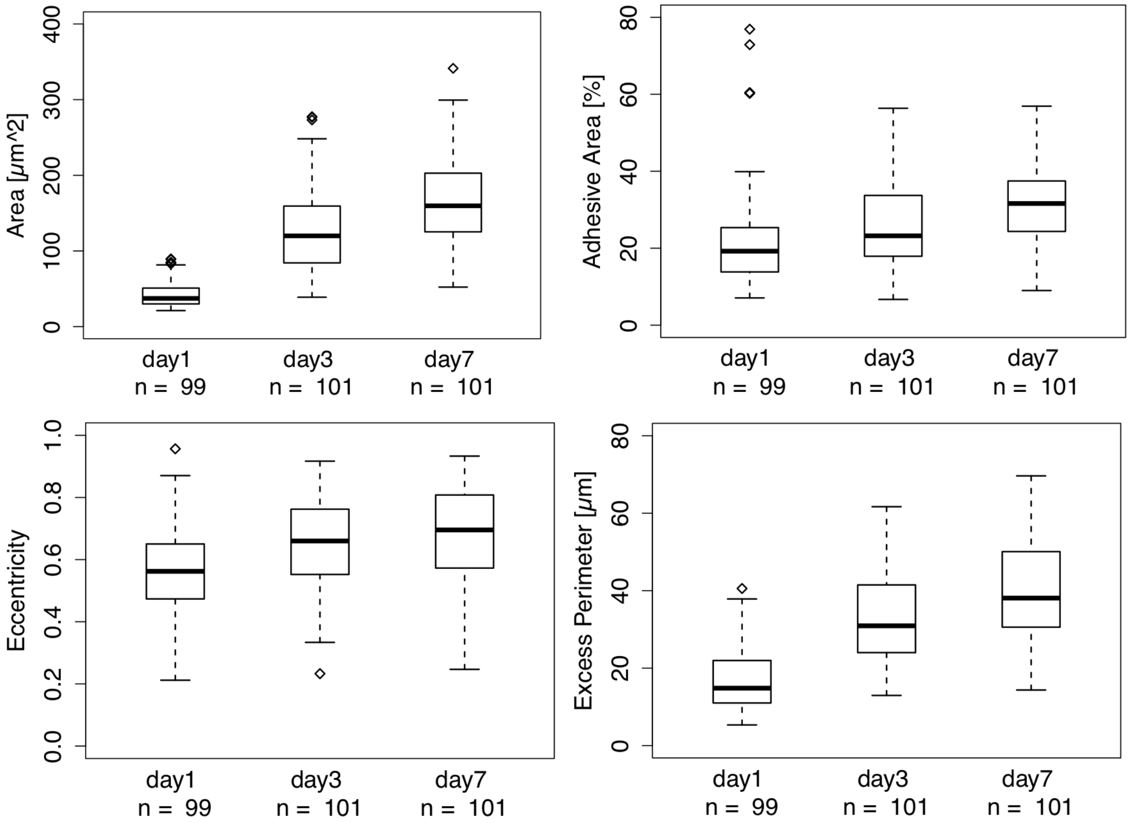

Figure 26 Area, adhesive area, eccentricity and excess perimeter in dependence on CD4$^+$ T cell differentiation. CD4+ T cells were differentiated *in vitro* using aCD3/aCD28 beads (Dynabeads®, Invitrogen). Cells were seeded on surfaces coated with ICAM-1 and imaged with RICM on day 1, 3 and 7 after isolation. Image analysis was carried out with MATLAB. Results from donor 5are exemplarily shown, n indicates the number of analysed cells on each time point.

6.3.5 Donor variability of CD4$^+$ *in vitro* differentiation monitoring

Next, it was evaluated how adhesion parameters and fractal dimensions of T cells varied between donors. For this, analysis results of RICM images of cells from donor 1, 4 and 5 were compared.

Figure 27 shows fractal dimension of contour of those three donors in dependence with time. Donor 1 and 5 showed highest data variance on day 1, whereas data of donor 4 varied most on day 3. This might be correlated with the initial percentage of differentiated and undifferentiated cells, which was below 60 % for donor 1 and 5 and above 60 % for donor 4. Altogether, fractal dimension of contour showed no obvious differences between donors.

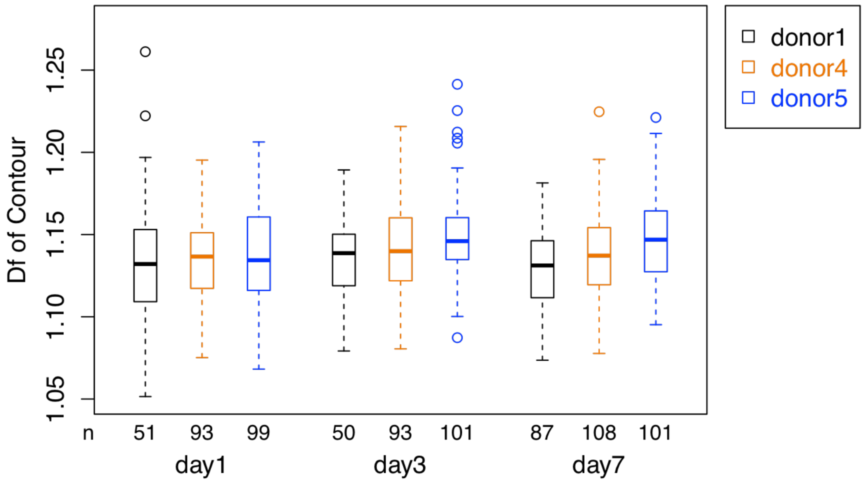

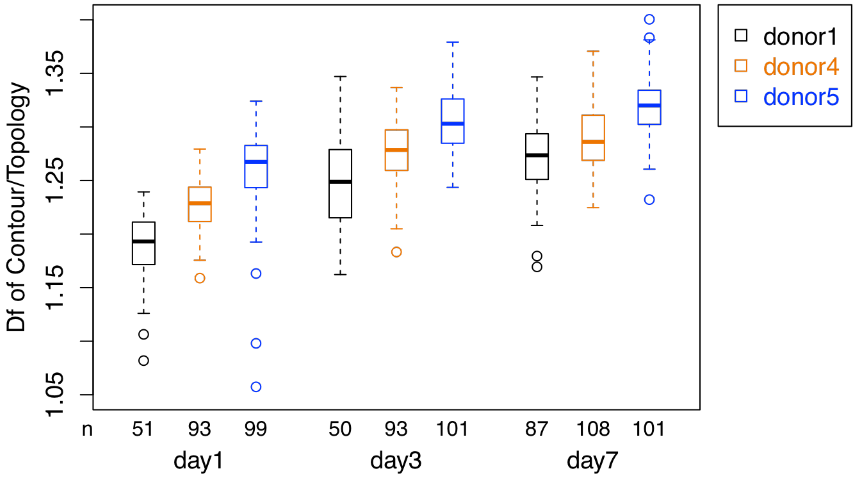

Figure 27 Fractal dimension of contour and of contour/topology of in vitro differentiated CD4$^+$ T cells isolated from different donors. Cells were isolated and incubated with aCD3/aCD28 beads for differentiation induction. On day 1, 3 and 7 cells were seeded on ICAM-1 coated surfaces, imaged with RICM and fractal dimensions were determined. The number of evaluated cells per time point is given with n.

For all donors, an increase of values for Df of contour/topology from day 1 to day 7 was observed. Compared to the other donors, donor 1 showed lowest Df values, highest values were obtained for donor 5. Interestingly, increasing Df values from donor 1 to donor 5 on same time points were obtained. In total, an increase in mean fractal dimension of contour/topology upon differentiation could be detected from day 1 (~ 1.23) to day 3 (~ 1.28), but not from day 3 to day 7 (~ 1.29).

Regarding cell area (Figure 28, upper), results between donors were comparable for all measured time points, showing an increase from day 1 to day 7. Initial starting value for donor 1 (27 μm^2) was smaller than for the other donors (43 μm^2), which correlates with the initial number of undifferentiated CD4$^+$ T cells. On day 7, measured cell area ranged from 158 μm^2 (donor 1) to 186 μm^2 (donor 4).

An increase in adhesive cell area upon differentiation for all donors was also observed (Figure 28, lower). Here, donor 1 showed highest values on day 1 and 3 compared to the other donors.

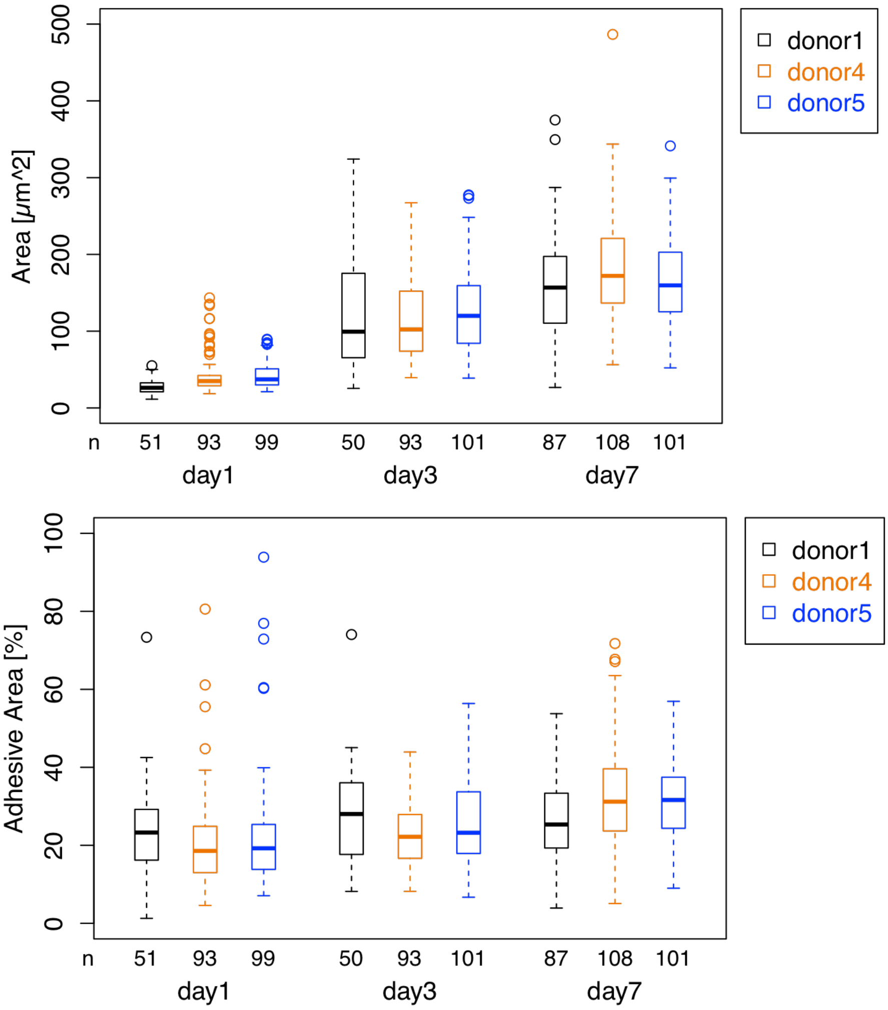

Figure 28 Area and percentage of adhesive area of in vitro differentiated CD4$^+$ T cells isolated from different donors. Cells were isolated and incubated with aCD3/aCD28 beads for differentiation induction. On day 1, 3 and 7 cells were seeded on ICAM-1 coated surfaces and imaged with RICM. The number of analysed cells per time point is given with n.

Excess perimeter and eccentricity were highly comparable regardless of the donor cells were derived from (Figure 29). The latter increased from ~ 0.6 on day 1 to 0.68 on day 3 and 7. On day 1 and 3, highest values were measured for donor 1. The excess perimeter also increased upon differentiation, from ~ 16 μm on day 1 to 31 μm on day 3 and further to ~36.8 μm on day 7.

In total, adhesion parameters obtained from RICM images of *in vitro* differentiated CD4$^+$ T cells were comparable between different donors. Although donor dependencies were still observed, the overall trend of parameter dependencies upon differentiation could be shown. Strongest donor variability was found for fractal dimension of contour/topology.

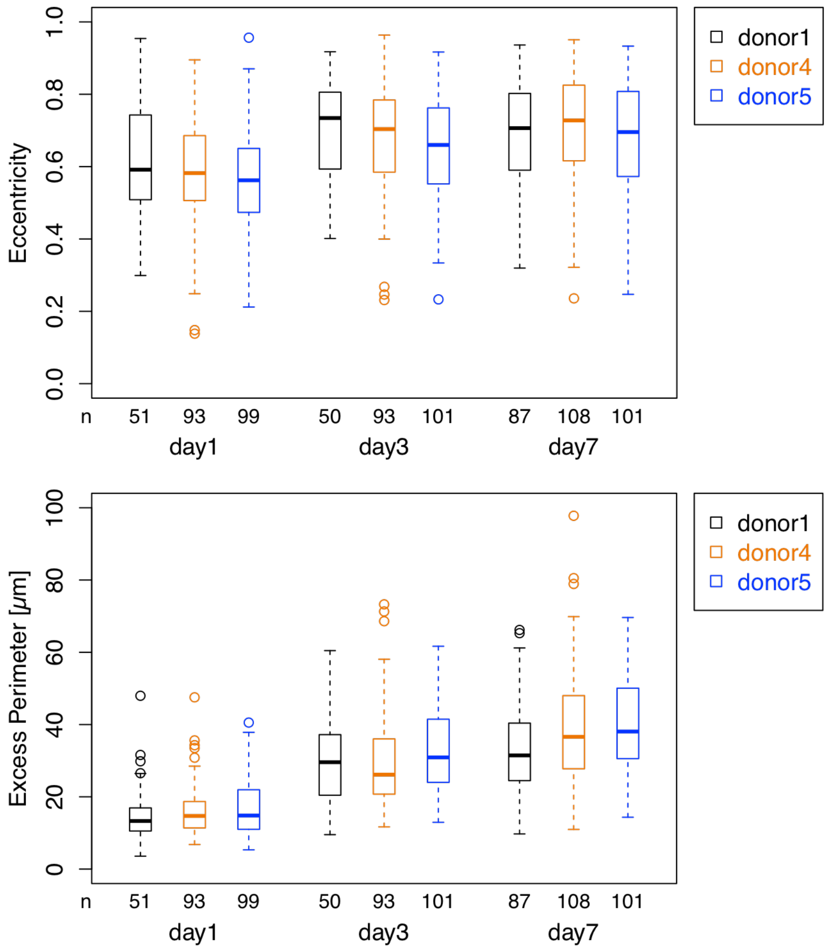

Figure 29 Eccentricity and excess perimeter of adhesive area of in vitro differentiated CD4$^+$ T cells isolated from different donors. Cells were isolated and incubated with aCD3/aCD28 beads for inducing differentiation. On day 1, 3 and 7 cells were seeded on ICAM-1 coated surfaces and imaged with RICM. The number of evaluated cells is given with n.

In summary, adhesion parameters and fractal dimensions of T cells were highly comparable between donors. Our results showed that RICM imaging of T cells and extraction of adhesion-related parameters is a highly suitable approach for maker-free monitoring of *in vitro* T cell differentiation.

6.4 T cell subtype isolation and identification

In the next step, it was evaluated whether adhesion parameters and fractal dimensions are suitable for characterising T cell subsets that differ in their *in vivo* differentiation states.
In this section the isolation of human T cell subpopulations is described, followed by the determination of their adhesion-related parameters as explained in the previous sections. The obtained T cell subpopulation characterisation was then used for marker-free T cell subset identification (Figure 30).

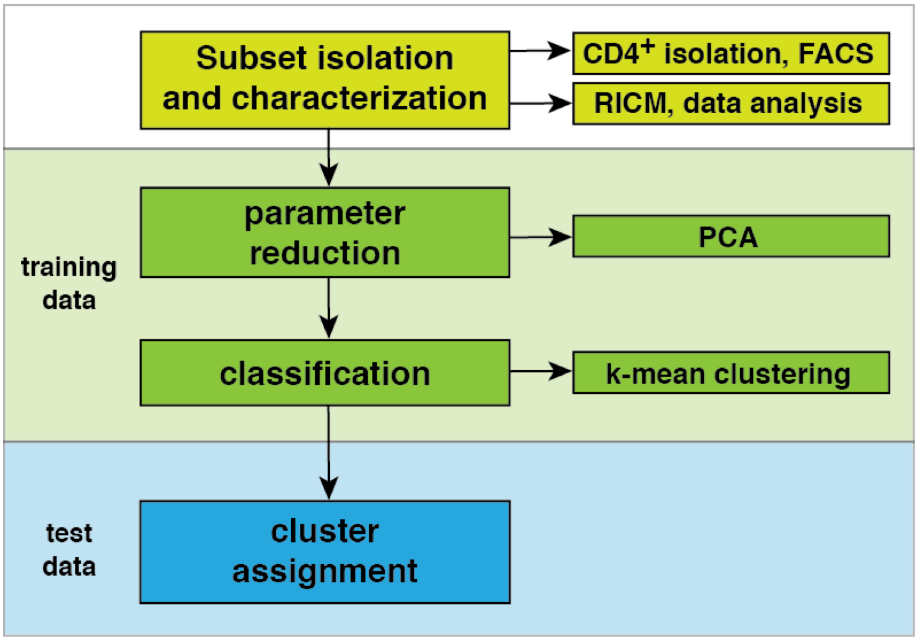

Figure 30 Workflow for T cell subset characterisation and identification. First, T cell subpopulations were isolated and imaged with RICM. Characterization was done determining adhesion parameters and fractal dimensions from the obtained images. Using training data, parameters that describe the data best were determined by principal component analysis (PCA). Based on these parameters, classification using k-mean clustering was done. Finally, cells of test data sets were assigned to the clusters for determining the goodness of T cell subset identification.

6.4.1 Sorting of human T cell subpopulations and purity control by FACS

T cell subpopulations that display different *in vivo* differentiation states were isolated from human CD4$^+$ T cells: naïve (T_N), central memory (T_{CM}) and effector memory T cells (T_{EM}). CD4$^+$ T cells isolated from six anonymous donors were analysed by flow cytometry regarding their CD4 and CD3 expression (Table 6-2). The purity of cells’ CD3 expression was > 98.5 % for all experiments. Lowest expression of CD4 was found for cells isolated from donor A (95.2 %).

Table 6-2: Isolation of naïve, effector memory and central memory CD4$^+$ T cells – FACS overview. Purity of CD4$^+$ T cells isolated from human peripheral blood was analysed by CD3 and CD4 expression. During the sorting process, the percentage of naïve (Tn), effector memory (Tem) and central memory (Tcm) T cells was determined based on the expression of CD62L and CD45RA.

	% of CD3	% of CD4	% of Tn	% of Tcm	% of Tem
donor A	98.6	95.2	70.91	15.6	3.9
donor B	98.7	97.9	69.1	16.0	6.6
donor C	99.6	98.9	63.6	17.1	5.5
donor D	99.5	97.0	13.74	39.5	25.3
donor E	99.7	99.7	30.86	30.88	17.4
donor F	99.5	98.6	51.5	15.35	11.5

CD4$^+$ T cell populations were depleted of cells expressing CD25 by magnetic labelling. The frequencies of subpopulations within these CD4$^+$CD25$^-$ T cells were evaluated (Table 6-2), which was based on expression of CD45RA and CD62L (Figure 31):

T_N (CD45RA$^+$ CD62L$^+$), T_{EM} (CD45RA$^-$ CD62L$^-$) and T_{CM} (CD45RA$^-$ CD62L$^+$). The percentage of T_N was above 50 % for 4 donors. Here, T_{CM} were 15 – 17 % and the amount of T_{EM} ranged from 4 to 12 %. For 2 donors, the percentage of T_N was lower, and the amount of memory subsets increased accordingly.

Subpopulation isolation with FACS was also based on the expression of CD45RA and CD62L (Figure 31).

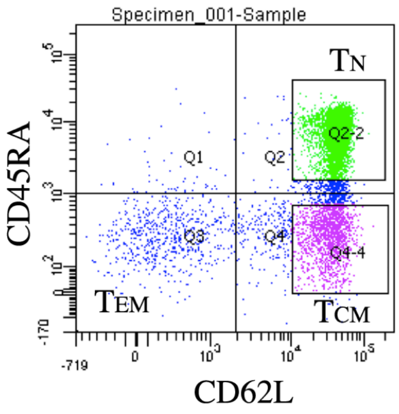

Figure 31 Sorting of human CD4$^+$ T cell subpopulations according to CD45RA and CD62L expression. T_N: naïve T cells; T_{EM}: effector memory T cells, T_{CM}: central memory T cells.

6.4.2 Characterization of T cell subpopulations: fractal dimensions and adhesion parameters

Isolated T cell subsets were seeded on ICAM-1 coated surfaces and imaged with RICM (Figure 32). We then determined fractal dimensions and adhesion parameters from the obtained images and evaluated their suitability for T cell subset characterisation.

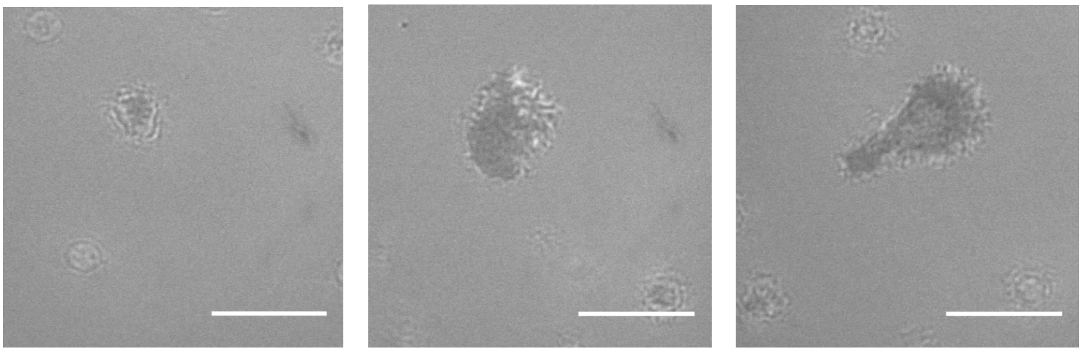

Figure 32 RICM images of naïve (left), central memory (central) and effector memory (right) CD4$^+$ T cells. CD4+ T cells were isolated from human PBMCs and separated into subpopulations according to CD45RA and CD62L expression. Cells were seeded on ICAM-1 coated surfaces and imaged with RICM. Scale bar: 10 μm.

Figure 33 shows representative results of Df of contour and of contour/topology derived from T cells isolated from donor B.

Df of contour did not show significant differences within subpopulations, but decreasing variance (Table 6-3), which was also true for Df of contour/topology. This parameter additionally showed significant increase from naïve to effector memory cells and from naïve to central memory cells ($p << 0.025$, determined with Mann-Whitney-U-Test). Decrease from effector to central memory cells was also significant ($p = 0.005$; see also section 10).

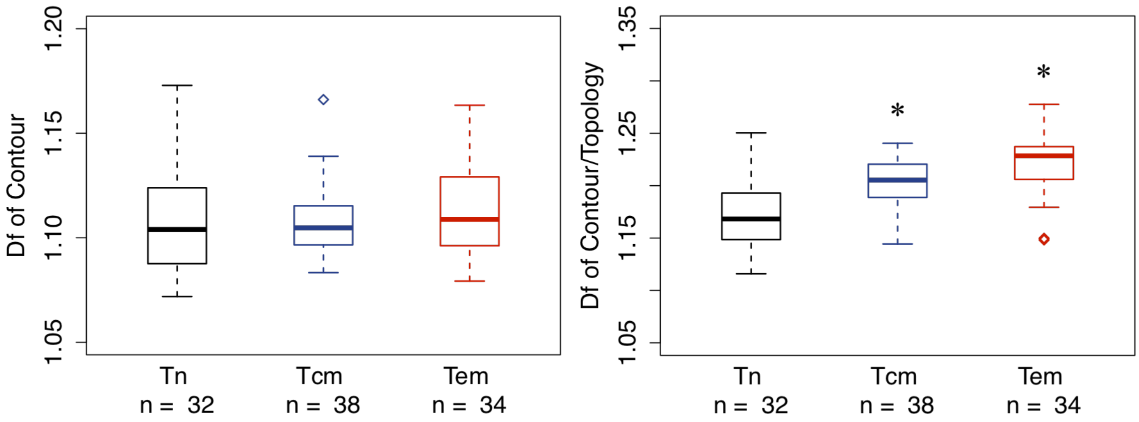

Figure 33 Fractal dimension (Df) of contour and contour/topology of naïve (Tn), effector memory (Tem) and central memory (Tcm) CD4$^+$ T cells. Subpopulations were separated from human CD4+ T cells (donor B) by FACS, seeded on ICAM-1 coated surfaces and imaged with RICM. Image processing was carried out with MATLAB and fractal dimensions were determined with the ImageJ Plug-in FracLac_2.5q. Mann-Whitney-U-Test comparing Tn with Tem and Tcm, respectively, was performed and p << 0.025 marked with an asterix; n indicates the number of cells.

Adhesion parameters from T cell subtypes derived from donor B are summarized in Figure 34. A significant increase from naïve to effector and also to central memory T cells in area, adhesive area, eccentricity and excess perimeter was observed (p << 0.025). Differences between effector and central memory T cells were only significant for eccentricity (p = 0.017).

Table 6-3: Variances of fractal dimensions and adhesion parameters of T cell subpopulations. Naïve (Tn), effector memory (Tem) and central memory (Tcm) CD4$^+$ T cells were isolated from donor B, seeded on ICAM-1 coated surfaces and imaged with RICM. Adhesion parameters and fractal dimensions were determined and variances were calculated. Tn: n = 32; Tem: n = 34, Tcm: n=38.

	Tn	**Tem**	**Tcm**
Df of contour	0.0006	0.0004	0.0003
Df of contour/topology	0.0012	0.0009	0.0005
area	356.0265	375.6921	306.6765
eccentricity	0.0362	0.0328	0.0157
perimeter	117.844	84.9861	51.9337
adhesive area	66.9298	49.7403	148.8617
circularity	0.0079	0.0057	0.0036
excessive perimeter	39.494	27.77	15.6259

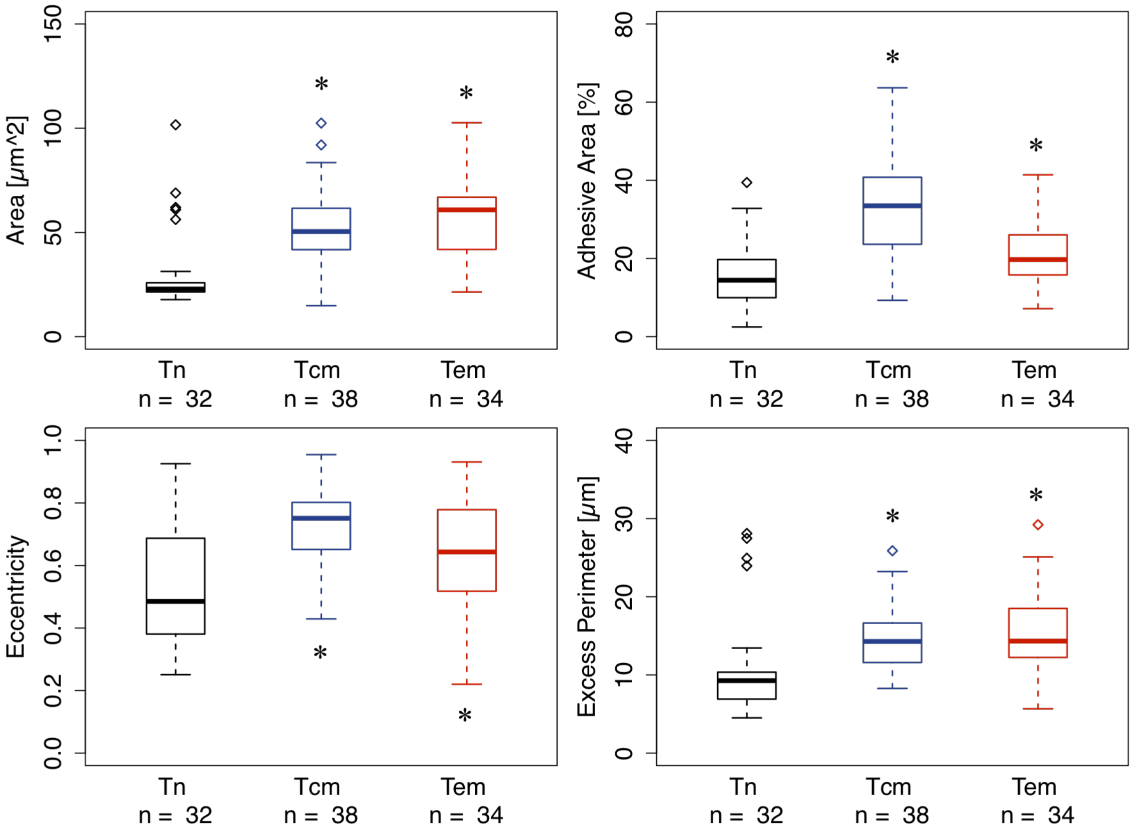

Figure 34 Adhesive parameters of naïve (Tn), effector memory (Tem) and central memory (Tcm) CD4^{+} T cells. Subpopulations were separated from human CD4+ T cells (donor B) by FACS, seeded on ICAM-1 coated surfaces and imaged with RICM. Image processing was carried out with MATLAB. Mann-Whitney-U-Test comparing Tn with Tem and Tcm, respectively, was performed and $p \ll 0.025$ marked with an asterix; n indicates the number of cells.

All evaluated parameters showed a decrease in variance from naïve to effector memory and to central memory cells (Table 6-3). The only exception was adhesive area. Here, central memory T cells showed highest data variance, followed by naïve and effector memory cells.

Our results showed that T_N are characterized by significant lower values of adhesion-related parameters compared to memory cells, and some parameters showed additional significant differences between central memory and effector memory T cells. Therefore, these parameters are suitable for characterising T cell subpopulations that display different *in vivo* differentiation states.

6.4.3 Subtype characterisation comparing different donors

Results presented above were derived from experiments using T cell subpopulations that were from donor B. For T cell classification it is essential to prove that these results are donor-independent. Therefore, adhesion parameters and fractal dimensions of cell subpopulations derived from all donors were determined. For each donor, the relative trends between subpopulations were determined by comparing mean values of respective parameters. Also, the Mann-Whitney-U-Test was performed and the p-value was evaluated. All results are summarized in section 10.

For donor B, E and F highest correspondences were found for all parameters. Results from these donors were only partially comparable with donor A, whereas Donor C and D showed higher conformities with donor A. Therefore, donor B, E and F were chosen for the following approach for T cell subset identification.

6.4.4 Parameter reduction: identification of parameter weights using PCA

The next step towards classification was to identify parameters that are most valid for describing and distinguishing T cell subsets. For this, PCA was performed using Df of contour, Df of contour/topology, area, adhesive area, eccentricity and excess perimeter. Data was plotted in principal component space, exemplarily shown for donor B in Figure 35a. Since PC1 covered 83 % of data variance, a histogram of subpopulations regarding PC1 only was generated (Figure 35b).

In both plots, naïve T cells clustered at low values for PC1, whereas effector and central memory cells were distributed at higher values, yet distinguishable since central memory cells peak at PC1 around 0, and effector memory at PC1 around 20.

The contribution of each parameter to the transformation was read out from the eigenvectors of the transformation matrix. Sorted parameters and their respective contribution are summarized in Table 6-4 for donor B, E and F. Parameters with highest contributions to data transformation were area and excess perimeter, followed by eccentricity.

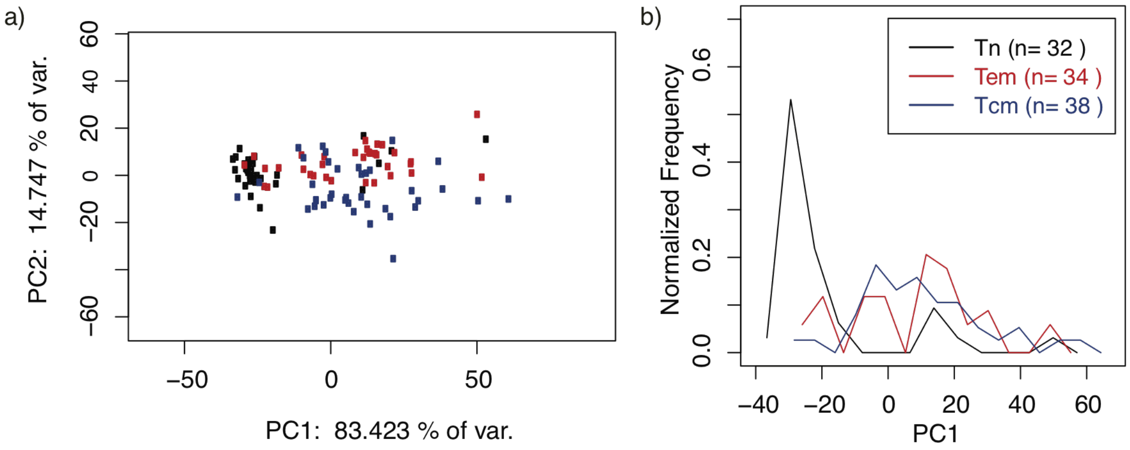

Figure 35 Principal Component Analysis of T cell subpopulations. PCA was carried out using Df of contour, Df of contour/topology, area, adhesive area, eccentricity and excessive perimeter. a) Principal component (PC) 1 was plotted against PC2 and data points were color-coded according to the subtype. Coverages of data variance by PCs are depicted. b) Histogram of subtypes regarding PC1; n indicates the total number of cells.

Comparing the consistencies of these parameters between experiments (section 10), we found that area and excess perimeter showed highly comparable trends for donor B, E and F, whereas adhesive area did not. Since Df of contour/topology showed very high consistencies for the majority of experiments, this parameter in addition to area and excess perimeter was chosen for T cell subtype classification described in the following chapter.

Table 6-4: Contributions of parameters to data transformation during PCA. T cell subpopulations were isolated from three independent donors and adhesion-related parameters were determined from RICM images of the cells, followed by PCA of the data obtained for each donor. The contribution of parameters to data transformation was read out from the eigenvectors. Listed are parameters and their respective contribution value. adh. area: adhesive area; e. perimeter: excess perimeter.

donor B		donor E		donor F	
area	0.977461	area	0.972033	area	0.930431
e. perimeter	0.165035	e. perimeter	0.194586	adh. area	0.322784
adh. area	0.131653	adh. area	0.131483	e. perimeter	0.173489
eccentricity	0.000891	eccentricity	0.000929	eccentricity	0.003162
Df of contour/ topology	0.000718	contour	0.000284	Df of contour/ topology	0.001122
Df of contour	0.000162	Df of contour/ topology	0.000213	Df of contour	0.000124

6.4.5 Cluster analysis and classification of T cell subsets from test data sets

Having identified four parameters that describe the data best, classification using these parameters could now be carried out. This section describes the optimization of the clustering approach and the correctness of subtype assignments are presented.

The approach used in this thesis was based on k-mean clustering of a training data set. Each subpopulation was thereby represented by clustering points within the data space. For classification, the Euclidean distances between a cell from a test data set and the clustering points were calculated. The clustering point with minimum distance was determined and the cell was assigned to that subtype which corresponded to this clustering point. Then, goodness of classification was determined by comparing the assigned subtype to cells' subtype of origin.

Donor B was chosen as the training data set. K-mean clustering was performed on this data and outliers were excluded in order to improve results.

First, it needed to be evaluated whether the chosen parameters are sufficient for classification and how many cluster points are needed on order to achieve best results.

In the first approach, clustering of the training data set was performed using the parameters area, excess perimeter and Df of contour/topology. Data from donor E was chosen as the test data set. Classification was carried out by randomly selecting 10 cells from the test data, repeating this 10 times and calculating the average correct cluster assignment for determining the classification accuracy. For one cluster, the correctness of classification was 67 %, increasing to 73 % when using 3 clusters (Table 6-5).

Table 6-5: Optimization of T cell subtype classification. Data of donor B was chosen as training data. K-mean clustering was performed using 1, 2 or 3 cluster points and depicted parameters. The minimum euclidean distances between data points of test data set (donor E) and cluster points were determined and accordingly assigned to the respective subtypes. The accuracy of T cell subtype classifications, comparing assigned subtype and actual subtype, are depicted. 10 cells of the test data set were randomly selected and the mean value of 10 iterations was determined.

parameters used for classification	**classification accuracy**		
	1 cluster	2 clusters	3 clusters
area, excess perimeter, Df of contour/topology	67 %	66 %	73 %
area, excess perimeter, Df of contour/topology, adhesive area	75 %	77 %	80 %

In order to improve these results further, adhesive area was added to the parameters used for clustering. Here, 80 % of cells from the test data set were correctly assigned to its subpopulation when using three clusters. Cluster points are shown in Figure 36 in 2D representation and in Figure 37 in 3D.

In the following, this approach was used to determine the correctness of classification with further test data sets.

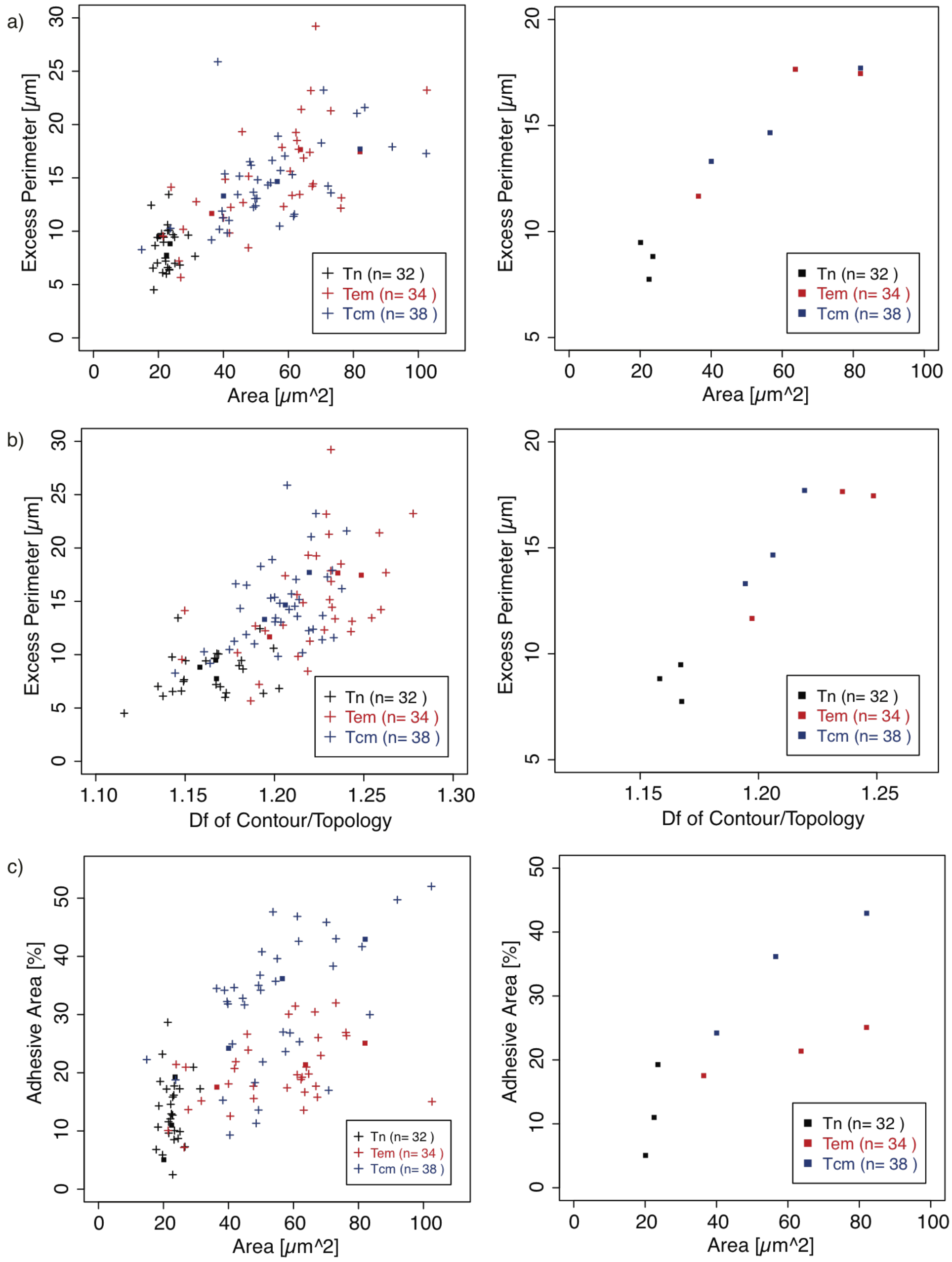

Figure 36 K-mean clustering of training data set (donor B) using area, excessive perimeter, Df of contour/topology and adhesive area. This clustering approach using three cluster centres showed best results for classification of T cell subpopulations from test data sets. The number of cells in each data set is given with n.

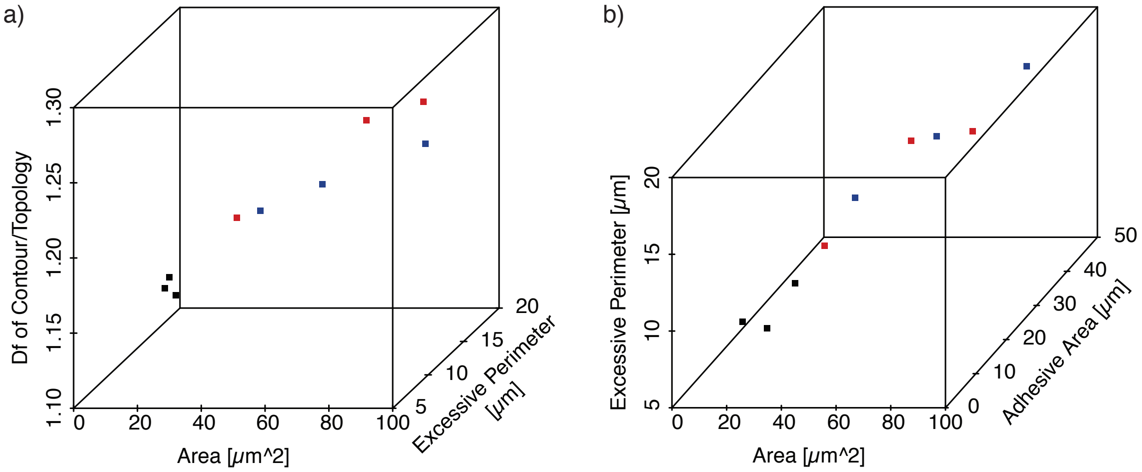

Figure 37 Centres of k-mean clustering used for T cell classification. These cluster points were derived by k-mean clustering of training data (donor B) using area, excess perimeter, Df of contour/topology and adhesive area.

For identifying T cell subsets from other test data sets, k-mean clustering of data from donor B was performed. Clustering was based on the parameters area, excess perimeter, Df of contour/topology and adhesive area, using one, two or three cluster centres. Test data from donor D, E and F were then classified as described above and the assigned subtypes compared to original subtypes. Again, 10 cells of each data set were randomly selected and the mean value of 10 iterations was determined (Table 6-6). For all test data sets, correctness of classification was lowest when using one cluster point. Best results were achieved when three clusters were used for k-mean clustering of the training data set. Here, results of correct cluster assignment were highly comparable between the used test data sets, and a classification accuracy of 80 % was obtained.

Table 6-6: T cell subtype classification using three independent test data sets. Data of donor B was chosen as training data. K-mean clustering was performed on area, excess perimeter, Df of contour/topology and adhesive area, using 1, 2 or 3 cluster points. Data from donor D, E and F were chosen as test data sets. For each donor, the correctness of classifications were determined by randomly selecting 10 cells and calculating the mean value of correct subtype assignment from 10 iterations.

test data set	**classification accuracy**		
	1 cluster	2 clusters	3 clusters
donor D	71 %	76 %	79 %
donor E	75 %	77 %	80 %
donor F	74 %	76 %	79 %

The obtained correctness of classifications show that the adhesion parameters area, adhesive area and excess perimeter together with the fractal dimension of contour/topology are highly suitable for assigning T cells to the correct subsets. These parameters were found to correlate with T cell differentiation. They have been extracted from RICM images of T cells, which is a marker-free, fast and low-cost method and therefore highly promising as a new approach for monitoring T cell subsets in peripheral blood.

In order to realize the application of this method in clinical settings, the accuracy of classification needs to be improved. Since correct classification of 80 % has been achieved by using only four parameters, it is very likely that adding one or more additional parameters could improve classification results to up to 100 %. Promising parameters are cells' elasticities that are reflected in their dynamics of adhesion area. Also, the fractal dimension of cells' inner topology will contribute to better classification results (see section 7.2).

Our results suggest that this marker-free approach of T cell subset identification is highly promising for generating "adhesion fingerprints" of CD4$^+$ T cell populations from peripheral blood. These fingerprints can reflect changes in the composition of T cell subsets and are therefore suitable for discriminating between healthy and diseased states.

6.5 *In vitro* homing routes for distinguishing migration characteristics of healthy and diseased CD4$^+$ T cells

Differentiation states of T cell subsets determine the expression of adhesion and homing receptors that enable them to migrate into inflamed tissue (Mora & Andrian, 2006). Changes in migration patterns of CD4$^+$ T cells are therefore expected to result from alterations in T cell differentiation and activation states, and therefore reflect changes in T cell subset compositions. To discriminate between a healthy CD4$^+$ T cell "fingerprint" and one in disease state, we here use a murine *in vitro* Graft-versus-Host-Disease (GVHD) model. In this approach, we evaluated T cell migration on surfaces that mimic native homing routes into the intestine. This organ is one of the most affected sites where symptoms of GVHD become manifested (Shlomchik, 2007).

This section describes the fabrication and characterisation of surfaces that present the gut-homing chemokine CCL25 (Zabel et al., 1999) with nanometre precise spacing, together with an adhesive background, using ICAM-1. Migration of mouse CD4$^+$ T cells in dependence on chemokine spacing and their ability to sense the chemokine gradient was then evaluated. Migration characteristics of these CD4$^+$ T cells were then compared to CD4$^+$ T cells with a GVHD phenotype.

6.5.1 Co-functionalization of nanopatterned surfaces

For fabricating *in vitro* intestinal homing routes, we developed a surface co-functionalization approach which combines Block Copolymer Micellar Nanolithography (BCML) and thiol chemistry with PEG-alkyne passivation and copper(I)-catalysed azide alkyne cycloaddition. This realizes site-specific presentation of NTA, which is a chelating agent for His$_6$-tagged proteins. The cation Co^{3+} was chosen as the complex-mediating ion between NTA and His$_6$-tagged CCL25 and ICAM-1, since the formed (NTA(Co^{3+})His$_6$) complex is highly stable and therefore allows orthogonal functionalization of presented NTAs on the surface

With a carefully chosen sequence of functionalization steps shown in Figure 38, we were able to functionalise gold nanoparticles with the chemokine CCL25 and ICAM-1 was anchored to the area between the particles.

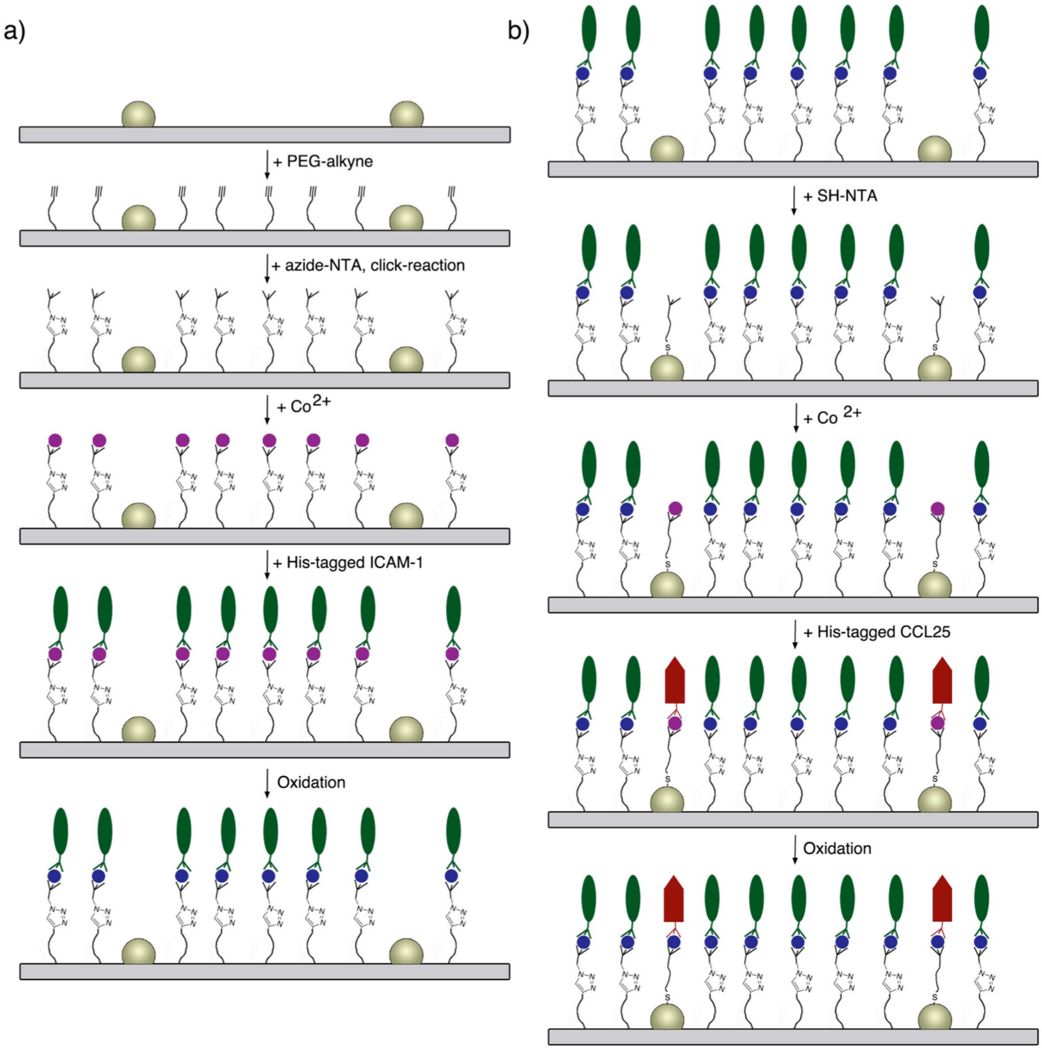

Figure 38 Scheme of the developed co-functionalization approach for generating in vitro homing routes. a) Gold nanoparticles were deposited on glass surfaces by using Block Copolymer Micellar Nanolithography (BCML). The area between the particles was passivated with PEG-alkyne that prevents unspecific protein and cell binding. It also provided alkyne groups to which NTA-azide was covalently linked by using the copper(I)-catalysed azide alkyne cycloaddition. Then, His_6-tagged ICAM-1 was bound. b) Gold nanoparticles were subsequently functionalized with NTA via a thiol linker, serving anchoring points for His_6-tagged CCL25. a) and b) Binding of His_6-tagged proteins to NTA was mediated by Co^{3+}, which was formed by incubating the formed $NTA(Co^{2+})His_6$ complex with H_2O_2 (Oxidation).

6.5.2 Characterization of co-functionalized surface

We determined whether anchorage of CCL25 and ICAM-1 to the surfaces is site-specific and stable, which is a requisite for using them as *in vitro* homing routes.

Binding of CCL25 to gold nanoparticles determined with AFM and immunogold labelling

For proving the presence of CCL25 on surfaces with AFM, nanopatterned surfaces were passivated with PEG and gold nanoparticles were functionalized with His_6-CCL25 through the NTA(Co^{3+})His_6 complex. AFM measurements showed that functionalized nanoparticles have a height of 6 - 8 nm relative to the passivated background (Figure 39a). Non-functionalized particles are 3 nm in height compared to the PEG layer (Figure 39b). Thus, binding of CCL25 was successful and site specific.

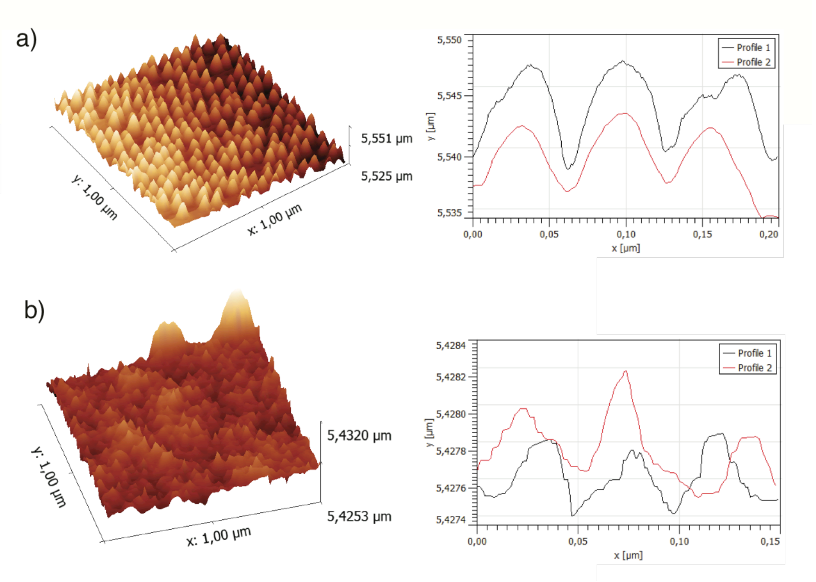

Figure 39 Proving CCL25 binding to gold nanoparticles with AFM. 3D profile and line profile of a) PEG-passivated nanopatterned surfaces functionalized with CCL25 on gold nanoparticles and b) PEG-passivated nanopatterned surfaces.

This was also shown using immunogold labelling of CCL25. Surfaces were prepared as described for AFM measurements, additionally incubated with gold-coupled IgG antibody and imaged with scanning electron microscopy (SEM). As shown in Figure 40, functionalized surfaces showed double dots, resulting from the nanopattern and the immunogold labelling. Negative control samples did not show these agglomerations. Therefore, binding of CCL25 to gold nanoparticles on glass surfaces was shown to be successful.

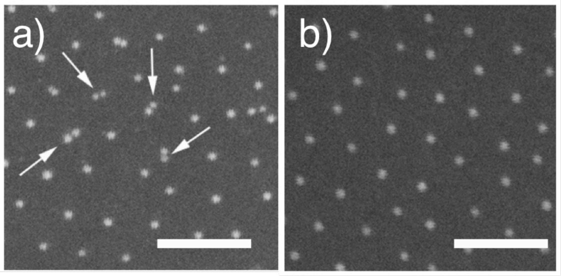

Figure 40 Immunogold-labelling of CCL25 on gold nanoparticles. a) PEG-passivated nanopatterned surfaces functionalized with CCL25 on gold nanoparticles and b) PEG-passivated nanopatterned surfaces were incubated with CCL25 antibody (rat) and anti-rat IgG (whole molecule)-gold antibody. Surfaces were then imaged with scanning electron microscopy. Scale bar: 200 μm

Characterization of ICAM-1 functionalization with quarz crystal microbalance (QCM)

For determining ICAM-1 binding to the surfaces, the success of the copper(I)-catalysed azide alkyne cycloaddition (click reaction) needed to be ensured.

The presence of PEG-coupled NTA on the surface was determined with QCM, measuring binding of His_6-tagged GFP on surfaces. Briefly, crystals were passivated with PEG-alkyne and azide-NTA was covalently linked by using the click reaction. During QCM measurements, crystals were incubated with Co^{2+} and His_6-tagged GFP (Figure 41a).

A shift in frequency of -45 Hz indicated protein binding to the surface. The formed $NTA(Co^{2+})His_6$ complex was subsequently oxidized by H_2O_2 incubation and the stability of the resulting $NTA(Co^{3+})His_6$ complex was determined by washing the crystals with the

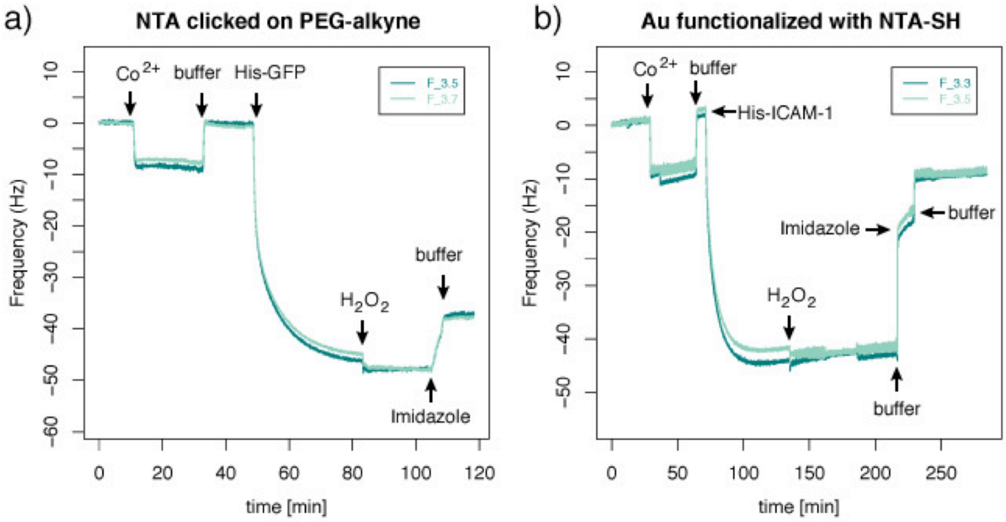

Figure 41 Protein binding to surfaces measured with QCM. a) Silica crystals were passivated with PEG-alkyne and coupled with azide-NTA using click reaction. Binding of His_6-GFP mediated by the $NTA(Co^{2+})His_6$ complex was monitored. b) Gold crystals were functionalized with NTA-SH and binding of His_6-ICAM-1 was monitored. In a) and b) the $NTA(Co^{2+})His_6$ complex was oxidized to $Co^{3+}(NTA)His_6$ by H_2O_2 incubation and its stability determined by washing with imidazole.

chelating reagent imidazole. After washing, the frequency difference compared to the baseline were -35 Hz. This showed that His_6-GFP was stably bound to the surface through the $NTA(Co^{3+})His_6$ complex. This confirmed the success of the oxidation reaction, also the presence of NTA on the crystal and therefore the success of the click reaction.

The functionality of His_6-ICAM-1 (Figure 41b) was also determined with QCM measurements (Figure 41b). Gold crystals were functionalized with NTA-SH. After formation of the $NTA(Co^{3+})His_6$ complex and washing with imidazole, a frequency shift of -10 Hz compared to the unfunctionalized surface was measured. Therefore, binding of His_6-ICAM-1 mediated by the $NTA(Co^{3+})His_6$ complex was successful and the His_6-tag of the protein was shown to be functional.

Effect of Oxidation on protein function

Since the $NTA(Co^{3+})His_6$ complex was formed by oxidizing the Co^{2+} containing complex ($NTA(Co^{2+})His_6$), it needed to be determined whether this oxidation step influences the biological function of CCL25 and ICAM-1.

Stability of ICAM-1 upon oxidation was tested using the murine T cell hybridoma cell line 3B11 (Figure 42). The adhesion of cells on surfaces that were functionalized with non-oxidized and oxidized ICAM-1 was compared using RICM imaging.

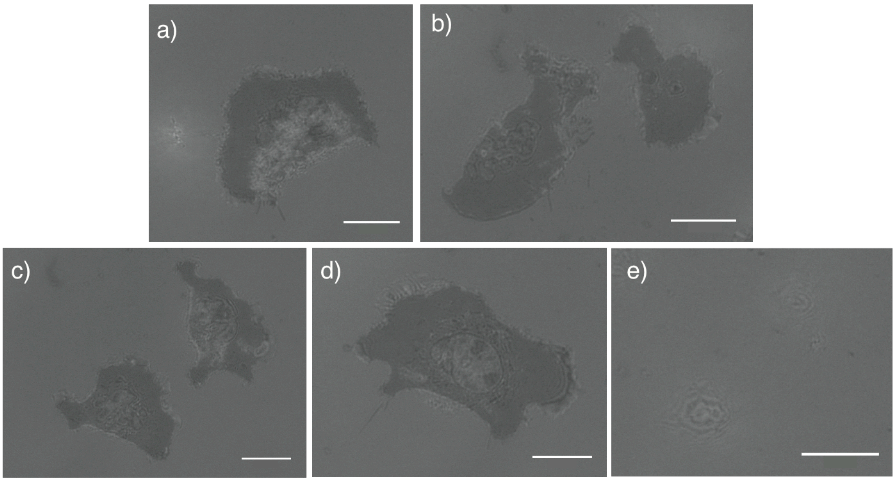

Figure 42 Effect of ICAM-1 oxidation on the adhesion of 3B11 T cells. Cells were seeded on surfaces and imaged with RICM. a) adsorbed ICAM-1; b) surfaces functionalized with PEG-alkyne, azide-NTA, Ni^{2+}, His_6-tagged ICAM-1; c) complex formation mediated by Co^{2+} and subsequent oxidation by H_2O_2 incubation; d) as in c) and followed by imidazole incubation; e) negative control: PEG. Scale bar: 10 μm.

Substrates were passivated with PEG-alkyne, coupled with azide-NTA and functionalized with His_6-ICAM-1. Cells that were seeded on substrates where Ni^{2+} was used as the complex-mediating ion showed very good adhesion, comparable to cells seeded on surfaces presenting adsorbed ICAM-1 (Figure 42a and b). For comparison, surfaces were functionalized with Co^{2+} and ICAM-1-His_6, followed by incubation with H_2O_2. By this, Co^{2+} was oxidized to Co^{3+}, and ICAM-1 was also exposed to the oxidizing reagent. Nonetheless, adhesion of cells maintained as observed before (Figure 42c). Next, the stability of the NTA(Co^{3+})His_6 complex was tested. For this, surfaces that presented this complex were washed with imidazole. Cells seeded on these surfaces showed same good adhesion as on the surfaces used before. Thus, the bioactivity of ICAM-1 was not influenced by incubation with H_2O_2, and Co^{3+} was proven to mediate complex formation in a highly stable manner.

In a second approach, protein functionality upon oxidation was determined by fluorescent labelling.

For determining ICAM-1 functionality after oxidation, glass surfaces were functionalized as shown in Figure 38a, followed by a second incubation with H_2O_2. Surfaces were then incubated with fluorescently labelled ICAM-1 antibody and the intensity value of the fluorescent signal was determined. Compared to non-oxidized surfaces, no difference in signal intensity was measured (Figure 43).

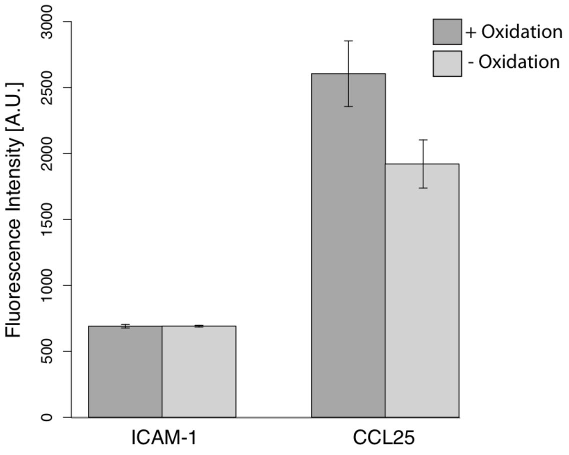

Figure 43 Effect of oxidation on ICAM-1 and CCL25 determined by fluorescent labelling. ICAM-1: Glass surfaces were passivated with PEG-alkyne/azide-NTA and the NTA(Co^{3+})His_6-ICAM-1 (+ oxidation) or NTA(Co^{2+})His_6-ICAM-1 (- oxidation) complex was formed. Surfaces were stained with fluorescently labelled ICAM-1 antibody and intensity values were measured. CCL25: Nanopatterned surfaces were co-functionalized with ICAM-1 and CCL25. Surfaces possessing the NTA(Co^{3+})His_6-CCL25 complex were stained with CCL25 antibody and compared with NTA(Co^{2+})His_6-CCL25 surfaces. Each bar represents mean values and standard errors of 8 measurements.

For determining whether oxidation influences the function of CCL25, nanopatterned glass surfaces were co-functionalized with ICAM-1 and CCL25 as described in section 5.1.3. Surfaces possessing the NTA(Co^{3+})His_6-CCL25 complex were stained with CCL25 antibody and compared with NTA(Co^{2+})His_6-CCL25 surfaces. Compared to non-oxidized surfaces, higher intensity values were measured on surfaces that underwent oxidation (Figure 43), which probably results in higher complex stability and thus less washing effects.

Co-functionalization determined with fluorescent labelling

For proving the co-functionalization of surfaces with CCL25 and ICAM-1 by fluorescent labelling (Figure 44), surfaces were functionalized as described before, and binding of both proteins was mediated by the NTA(Co^{3+})His_6 complex. Surfaces were then incubated with respective antibodies and fluorescently labelled.

In a first step, fluorescence intensities on single-functionalized surfaces were evaluated. ICAM-1 staining showed that nanopatterned areas exhibited less intensity values than plain areas. Staining of CCL25 showed that this protein is only present on nanopatterned areas of the surface.

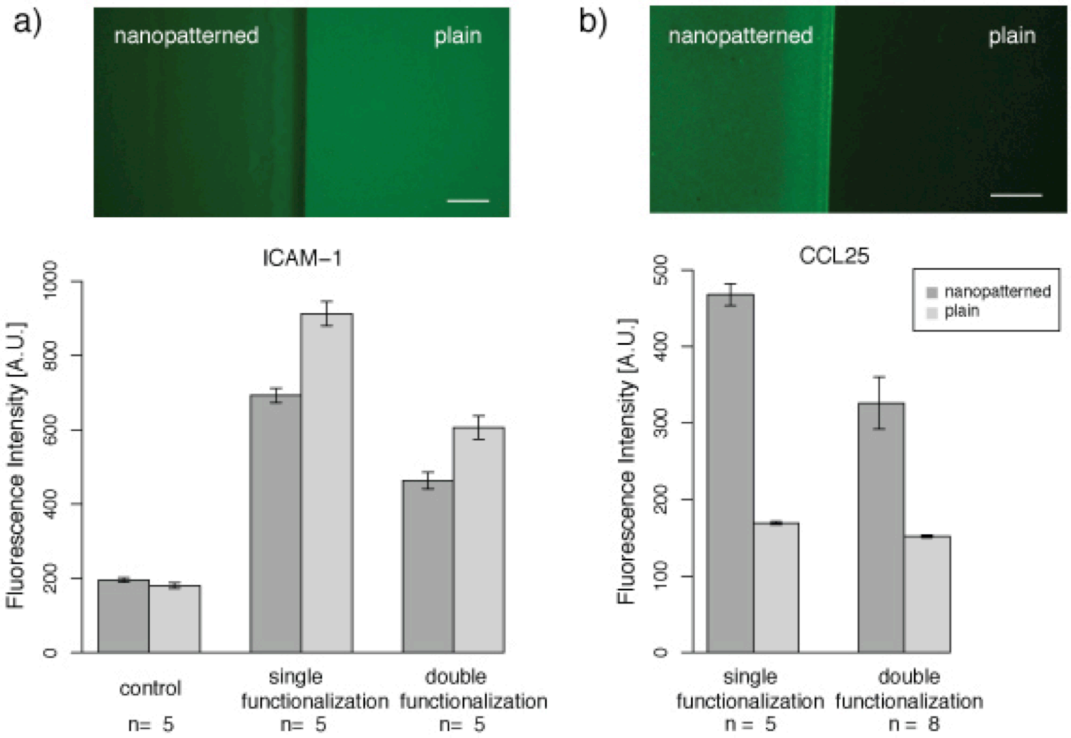

Figure 44 Fluorescence staining of functionalized nanopatterned surfaces. Surfaces were either single functionalized with ICAM-1 (anchored to glass) or CCL25 (anchored on gold nanoparticles), or double-functionalized with both proteins. Both proteins were separately labelled with respective fluorescent antibodies and imaged with fluorescent microscopy. Intensity values of areas with and without nanopatterns were determined (depicted as "nanopatterned" and "plain"). Microscopy images show dipping edges of labelled surfaces. Scale bar: 100 µm. a) Labelling of ICAM-1. control: not clicked. b) Labelling of CCL25. Shown are mean values and standard errors.

In a second step, surfaces were co-functionalized with both ICAM-1 and CCL25 and proteins were separately labelled through fluorescent antibody incubation. An overall decrease of fluorescence intensities for both proteins on respective areas was observed (Figure 44). Nonetheless, intensity signals of labelled ICAM-1 on plain areas were higher than on nanopatterned areas, as it has been observed for single-functionalized surfaces. Also, CCL25 was only present on nanopatterned areas of the co-functionalized surfaces.

Thus, this functionalization approach allows the anchorage of CCL25 and ICAM-1 with very high site specificity and stability. The method presented here is therefore highly suitable for generating surfaces that mimic native T cell homing routes.

These surfaces functionalized with the gut homing chemokine CCL25 and the adhesion promoting protein ICAM-1 were used for studying migration of healthy and diseased T lymphocytes in dependence on chemokine spacing. Also, surfaces were generated that presented CCL25 with gradient spacing over a defined distance and the ability of T cells to sense the gradient was evaluated.

Determining interparticle spacing of gradient surfaces with SEM

As described before, gold nanoparticles that served as anchoring points for His_6-tagged CCL25 were deposited on glass surfaces by using BCML. During the dip coating process, the retraction velocity of the glass substrate from the micellar solution was varied, which allowed controlling the distance between the particles. Here, the micellar solution of the diblock copolymer PS(1056)-b-P2VP(459) loaded with $AuCl_4^-$ at a loading rate of 0.3 was used. Interparticle distances were determined from SEM images of the surfaces.

Here, surfaces with homogeneous nanoparticle spacing of 55 nm, 69 nm and 94 nm were generated.

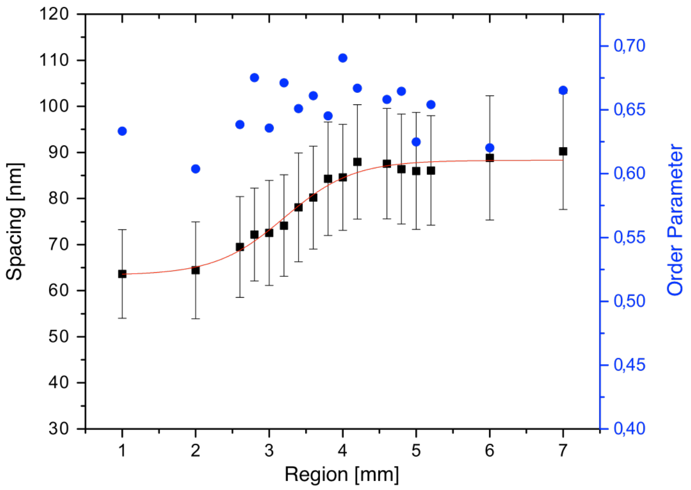

Figure 45 Interparticle spacing and order parameter of gradient nanopatterned surfaces. Glass surfaces were dip-coated with gold loaded micellar solution and the retraction velocity was decelerated over a defined distance. A representative surface was imaged with SEM and interparticle spacing in dependence on substrate position was determined, also the order parameter (0 – very low order; 1 – very high order).

For presenting CCL25 with gradient spacing on one substrate, gradient nanopatterned surfaces were generated by decelerating the retraction velocity during the dip coating process. A representative surface was imaged with SEM and interparticle spacing in dependence on substrate position was measured. As shown in Figure 45, nanoparticle spacing varied from 64 nm to 90 nm over a distance of 2 mm on the same substrate. The order parameter of gold nanoparticles was above 0.6 on all imaged substrate positions, which indicates high ordering. Substrates are therefore highly suitable for generating gradient presentation of CCL25 with high accuracy in interdistance spacing and high ordering.

6.5.3 Migration of healthy and GVHD-diseased mouse CD4$^+$ T cells on *in vitro* gut homing routes

Nanopatterned surfaces that were co-functionalized with CCL25 and ICAM-1 mimic gut homing routes of T cells. We seeded mouse CD4$^+$ T cells onto these substrates and evaluated their ability to respond to different chemokine spacings, also their efficiency to sense the presented CCL25 gradient. The migration characteristics of these cells were compared to GVHD-diseased CD4$^+$ T cells. The latter were derived by stimulating mouse CD4$^+$ T cells with retinoic acid (RA) *in vitro* in order to induce a GVHD phenotype (Iwata et al., 2004). FACS analysis of stimulated and unstimulated cells (Figure 46) confirmed that CCR9 and integrin α4β7 are up-regulated in stimulated cells; both express LFA-1 (experiments performed by K. Ottmüller, AG Beilhack, Würzburg University).

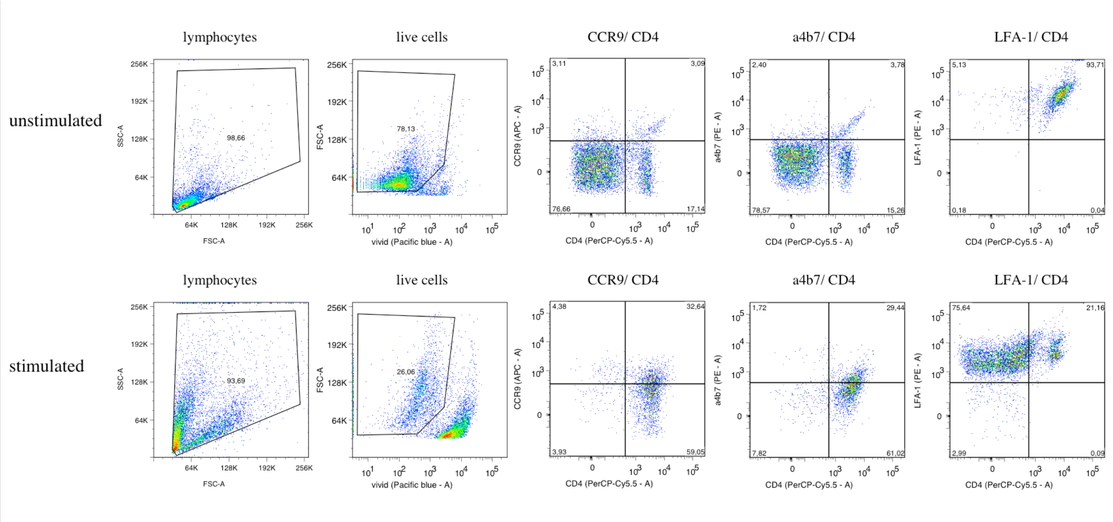

Figure 46 Expression of CCR9, α4β7 and LFA-1 of unstimulated and stimulated CD4$^+$ T cells. CD4+ T cells isolated from murine spleen were either not treated ("unstimulated") or "stimulated" in vitro with retinoic acid in order to introduce a GVHD phenotype. Expression of surface molecules was determined with FACS. (Data and plots: K. Ottmüller, AG Beilhack, Würzburg University)

Cell migration was determined on ICAM-1 presenting surfaces in order to evaluate migration induction by this adhesion-mediating protein. Unstimulated cells adhered very nicely to the surfaces, whereas GVHD phenotype cells exhibited less adhesion. As shown in Figure 47, unstimulated cells showed higher motility than stimulated cells.

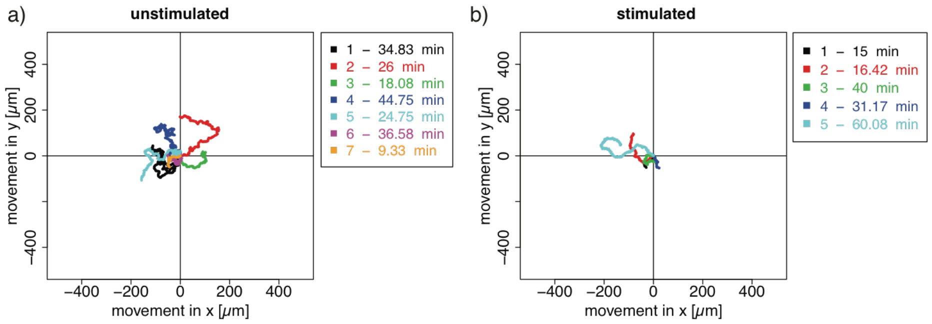

Figure 47 Migration trajectories of healthy (a) and RA-stimulated (b) CD4$^+$ mouse T cells on ICAM-1 functionalized surfaces. Mouse CD4$^+$ T cells were either unstimulated or stimulated in vitro with retinoic acid (RA) to induce the GVHD phenotype. Cells were seeded on ICAM-1-presenting surfaces and imaged with phase contrast microscopy at time intervals of 5 seconds. Migrating cells were manually tracked. Here, trajectories are shown and their respective time spans are given.

In order to evaluate T cell response to different chemokine densities, migration of healthy and diseased CD4$^+$ T cells was evaluated on surfaces presenting homogeneous ICAM-1 background and CCL25 with defined homogeneous interligand spacing (Figure 48). GVHD cells showed an increased motility on surfaces presenting low CCL25 spacing compared to higher spacing. On interligand spacing of 94 nm, unstimulated cells showed higher motility than stimulated T cells.

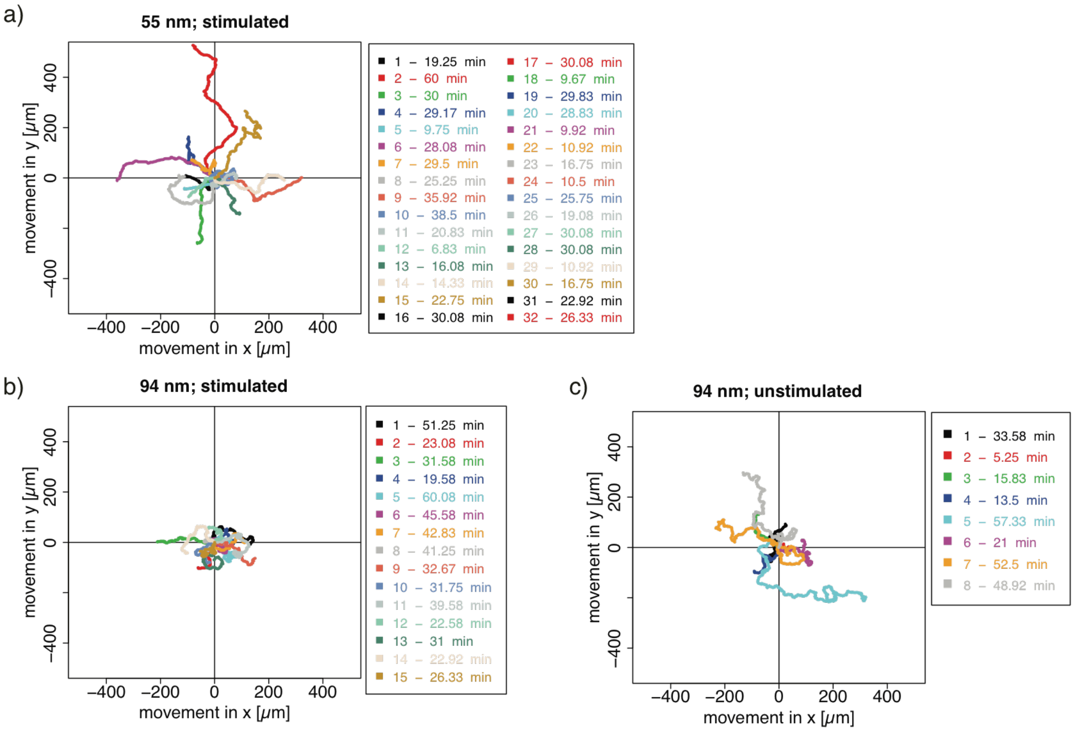

Figure 48 Trajectories of mouse CD4$^+$ T cells migrating on co-functionalized surfaces. Mouse CD4$^+$ T cells were either stimulated in vitro with retinoic acid (RA) to induce the GVHD phenotype (a and b) or unstimulated (c). Cells were seeded on surfaces presenting CCL25 with homogeneous spacing of 55 nm (a) or 94 nm (b and c) and ICAM-1 background. Migration trajectories are shown and their respective time spans are given.

These observations were also proven by evaluating mean cell velocities (Figure 49a). Stimulated cells exhibited decreasing velocities when seeded on substrates with increasing CCL25 spacing and thus decreasing CCL25 densities, whereas velocity of unstimulated cells was not dependent on chemokine spacing.

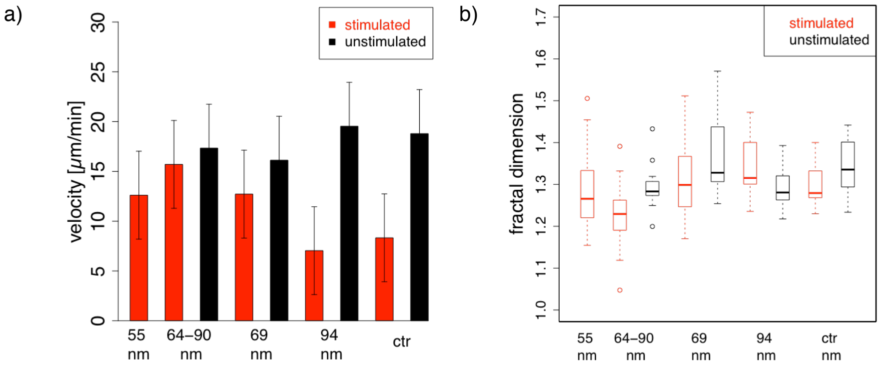

Figure 49 Velocity and fractal dimension of trajectories of stimulated and unstimulated cells migrating on co-functionalized surfaces. Mouse CD4$^+$ T cells were either unstimulated or RA stimulated to induce the GVHD phenotype. Cells were seeded on surfaces presenting ICAM-1 background and CCL25 with homogeneous or gradient spacing as indicated. ctr: ICAM-1 only. a) Velocity of cells on respective surfaces, shown are mean values and standard deviation. b) Fractal dimension of cells' trajectories on respective substrates.

The directness of cell migration on different conditions was quantified by determining the fractal dimension (Df) of trajectories (Figure 49b). Interestingly, trajectories of unstimulated cells exhibited higher Df values than unstimulated cells, especially on 69 nm chemokine spacing, indicating higher path tortuosity.

We next evaluated whether CD4$^+$ T cells are able to respond to the chemokine gradient. For this, healthy and diseased mouse CD4$^+$ T cell were seeded on surfaces presenting CCL25 with spacings ranging from 64 to 90 nm, together with ICAM-1 background. Unstimulated cells showed no directional migration towards the gradient direction, whereas a number of trajectories of RA-stimulated cells migrated in an angle towards the gradient direction, moving towards smaller interligand spacings (Figure 50).

On gradient surfaces, the fractal dimensions of cell's trajectories were found to be higher for unstimulated cells as compared to cells that exhibited the GVHD phenotype, which indicates more directed migration of stimulated cells.

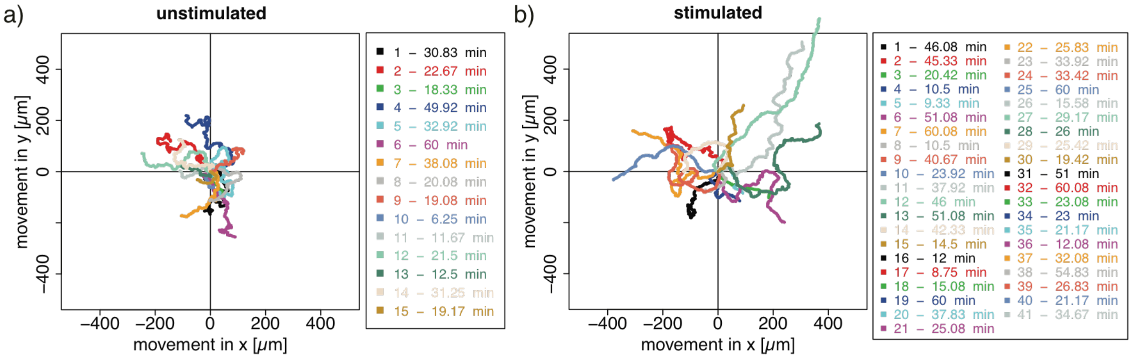

Figure 50 Migration trajectories of healthy (a) and RA-stimulated (b) CD4$^+$ mouse T cells on chemokine gradient surfaces. Mouse CD4$^+$ T cells were either unstimulated or stimulated in vitro with retinoic acid (RA) to induce the GVHD phenotype. Cells were seeded on surfaces presenting CCL25 gradient spacing ranging from 64 to 90 nm and ICAM-1 background. Trajectories of migrating cells are shown and their respective time spans are given. The x axis depicts the gradient direction.

Our results showed that healthy and GVHD CD4$^+$ T cells exhibited distinct migratory behaviours when seeded on surfaces that presented CCL25 with defined spacings. With increasing density of CCL25, motility of GVHD cells increases, whereas motility of non-stimulated cells was not found to be dependent on CCL25 presentation.

Thus, these co-functionalized surfaces were shown to be suitable for not only studying migration of T cells *in vitro*, but also for detecting migration parameters that can be correlated to diseases. This approach is marker-free and highly promising for detecting changes in T cell subset compositions that are related to diseases.

7 Discussion and Conclusion

7.1 *In vitro* T cell differentiation monitoring

T cells display various degrees of differentiation and functional properties. We postulated that these are reflected in their morphological characteristics, which can be determined from Reflection Interference Contrast Microscopy (RICM) images. Therefore, we investigated whether adhesion parameters and fractal dimensions of cell outline and topology correlate with differentiation *in vitro*. This will give first insight about the suitability of our approach for distinguishing T cell subsets that have differentiated *in vivo*. For monitoring differentiation of human CD4$^+$ T cell populations *in vitro*, PBMCs were isolated from peripheral blood and CD4$^+$ T cells were extracted, using the CD4$^+$ T cell isolation kit purchased from Miltenyi GmbH. Hereby, non-CD4$^+$ cells were magnetically labelled in a two-step process and separated from the non-labelled CD4$^+$ T cells. This technique is very advantageous since extracted T helper cells are untouched and therefore not influenced by ligand binding signals. FACS analysis determining CD4 and CD3 expression revealed very high purity of the isolated cell populations. Therefore, this approach is highly suitable for extracting CD4$^+$ T cells for further differentiation experiments.

Initial number of memory T cells in peripheral blood is donor dependent

For determining the initial amount of naïve and memory T cells within isolated CD4$^+$ T cell populations, cells were analysed towards their expression of the differentiation markers CD45RA and CD45RO on day 1 after isolation. Naïve T cells are positive for CD45RA and negative for CD45RO, whereas memory T cells show a reciprocal expression of these surface proteins (Michie et al., 1992). Also, expression of these CD45 isoforms depends on age. At young age, the amount of naïve T cells in peripheral blood is very high and decreases with age in response to exposure to divers antigens, whereas the amount of CD45RO$^+$ T cells increases (Gabriel et al., 1993) (Salvioli et al., 2003) (Cossarizza et al., n.d.). Besides the aging aspect, another reason for an increased number of blood-circulating memory T cells is acute pathogen exposure that results in clonal expansion of activated T lymphocytes (Pepper & Jenkins, 2011).

In our study, expression of the memory marker CD45RO varied between 30 % and 80 %. Since all donors were anonymous, the determined percentage of memory T cells cannot be correlated with donors' age or health state, but both aspects are possible explanations for the variety that has been observed.

Activation beads induce varying differentiation kinetics

In vitro differentiation of isolated T lymphocytes was induced by culturing cells in media supplemented with beads coated with anti-CD3 and anti-CD28 antibodies. Beads from two companies were compared: Dynabeads® from Invitrogen and MACSiBeads from Miltenyi. Differentiation of T cells was monitored over a time period of 7 days by analysing expression of the differentiation markers CD45RA and CD45RO. Within the examined time frame, different activation kinetics of these beads were observed. Dynabeads® induced strongest differentiation between day 1 and day 3, whereas cells incubated with MACSiBeads showed strongest differentiation between day 3 and day 7. Furthermore, Dynabeads® induced the expression of the memory marker CD45RA to almost 100 % in all experiments, whereas MACSiBeads achieved only 91 and 84 % memory marker expression of T cell populations.

The beads used differ in two main aspects: First, antibodies on Dynabeads® are already bound to the beads upon purchase, whereas MACSiBeads need to be loaded by the user. Second, Dynabeads® are covalently coated with anti-CD3 and anti-CD28 antibodies, MACSiBeads additionally present anti-CD2. It could therefore be expected that MACSiBeads lead to stronger T cell differentiation since CD2 provides co-stimulatory signalling (Green, Karpitskiy, Kimzey, & Shaw, 2000). Since this was not observed, it can be assumed that the density of activating ligands on the beads is different. Proving this would need further investigation, but increasing the density of ligands on MACSiBeads could most probably improve activation results.

Loading of MACSiBeads displays an additional source for variability, which should be avoided in the following experiments. Also, *in vitro* differentiation using Dynabeads® showed best results in inducing memory T cell marker expression. Due to these reasons, these beads were chosen for following experiments, which aimed to determine the change of adhesion parameters of whole CD4$^+$ T cell population in dependence on differentiation.

Ability of CD4$^+$ T cells to adhere to ICAM-1 coated surfaces depends on differentiation

T lymphocyte populations differentiated *in vitro* using Dynabeads® were seeded on ICAM-1 coated surfaces and imaged with RICM. ICAM-1 has been identified in preceding experiments as the protein that mediated adhesion of T cells best (see section 6.1.2). Also, ICAM-1 displays physiological relevance in trespassing of T lymphocytes from blood circulation into peripheral tissue. It therefore plays a general role in T cell trafficking (Woodland & Kohlmeier, 2009) and was therefore expected to mediate adhesion of T cells with a wide spectrum of differentiation states.

We found that the ability of T lymphocytes to adhere to ICAM-1 coated surfaces increased with differentiation. Expression of ICAM-1 receptor, LFA-1, is known to correlate with expression of memory T cell markers (Sanders et al., 1988). CD4$^+$ CD45RA^{high} cells were found to be LFA-1^{low}; but a small proportion of 10 % of these CD4$^+$ CD45RA^{high} was found to be LFA-1^{high}. Within CD4$^+$ CD45RA$^-$ cells, the percentage of cells being LFA^{high} was reported to be 56 % and increased with age (Hviid, Odum, & Theander, 1993; Okumura, Fujii, Takeuchi, & Inada, 1993). In contrast to that, Hviid et al. suggested that LFA-1 expression level is not tightly associated with CD45 isotype expression, but rather with the degree of cellular activation. According to his study, LFA-1^{high} cells possess higher levels of several activation markers than LFA-1^{low} cells. Here therefore suggested LFA-1^{high} cells mainly represent *in vivo* activated cells (Hviid et al., 1993).

Transferring this suggestion to our study, it can be assumed that T cells adhering to ICAM-1 coated surfaces on day 1 after isolation were mainly *in vivo* activated T cells, whereas non-activated T cells and thus naïve T cells were possibly less adherent and therefore under-represented in the obtained data. One way to enhance T cell adhesion despite their differentiation state is by exposing them to divalent cations (Mn^{2+} or Mg^{2+}), which are reported to alter LFA-1 conformation to its ligand binding state (Dransfield, Cabanas, & Craig, 1992). It is also necessary to determine the percentage of differentiated and non-differentiated cells that adhere to the surface, since this is of special interest for future applications, e.g. for determining the frequencies of subpopulations in peripheral blood of patients.

Fractal dimension of contour/topology of whole CD4$^+$ T cell populations correlate with differentiation

In vitro differentiated T lymphocytes were seeded on ICAM-1 coated surfaces and imaged with RICM. Obtained images were analysed and the fractal dimension (Df) of contour, Df of contour/topology and several adhesion parameters were determined.

Df values of contour did not vary in the course of *in vitro* differentiation and remained constant around values of ~ 1.15. Comparable results were found in a previous study by Losa et al. who determined the Df of whole CD4$^+$ T cell populations to be 1.16, using the box counting method also (Losa, 2002).

In contrast, Df of contour/topology increased from ~ 1.23 to ~ 1.29 within the first three days of differentiation, indicating an increase in membrane roughness (Behar, 2001; Klein et al., 2013; Losa, 2002). This parameter showed high dependency upon differentiation for all donors tested.

The observed increase in membrane roughness could result from enhanced cytokine release that is correlated with differentiation and thus effector state of T cells (see section 4.1.2). For example, T_{CM} have only little effector function and secrete IL-2, whereas T_{EM} have immediate effector functions and secrete several cytokines, such as IFN-γ, IL-4 and IL-5 (Sallusto et al., 2004). Cytokines are secreted through extracellular vesicles, which are released from the plasma membrane by shedding or budding (Robbins & Morelli, 2014). This perturbs the plasma membrane and increases its roughness. Another factor that alters membrane roughness is the configuration and composition of membrane lipids (Losa, 2002). It was reported that higher ordering of lipids in membrane micro-domains increases the ability of CD4$^+$ T cells to respond to TCR stimulation (Miguel et al., 2011). Thus, responsiveness to external stimuli correlates with membrane roughness. We were able to show that this can be quantified by fractal dimension of contour/topology, since effector and memory T cells display higher responsiveness to TCR triggering than naïve cells (Sallusto et al., 2004).

Adhesion parameters of whole CD4$^+$ T cell populations correlate with differentiation

To evaluate the dependence of T cell morphology on differentiation further, adhesion parameters of *in vitro* differentiated CD4$^+$ T cell populations were determined from RICM images, namely adhesion area, percentage of adhesive area, eccentricity and excess perimeter.

Both projected cell area and adhesive area significantly increased upon increased memory marker expression. This showed that differentiated T cells displayed improved adhesion capacities. This is in agreement with previous studies that correlate LFA-1 expression with memory T cell marker expression (Sanders et al., 1988).

The eccentricity of T cells increased upon differentiation, which could be attributed to increased migratory properties that are correlated with increased effector state, as reviewed by Mora et al. (Mora & Andrian, 2006)

The excess perimeter increased significantly upon differentiation, which reflects an increased membrane roughness. This could result from the formation of membrane protrusions, e.g. lamellipodia or filopodia. These membrane structures aid cells to probe their environment and form adhesion sites to the surface that enables them to migrate (Lauffenburger & Horwith, 1997). The observed increase in membrane roughness is in alignment with the increase of Df of contour/topology that was discussed before.

Concluding, for the first time T-cell adhesion parameters were derived from RICM images and a clear correlation between T cell differentiation state and several adhesion characteristics could be shown. Due to this high sensitivity, this approach can be applied for characterising *in vivo* differentiated T cells by their adhesion properties and fractal dimensions in order to deduce an adhesion “fingerprint” of T cell subsets.

7.2 Characterisation and classification of *in vivo* differentiated T cell subpopulations

Naïve, central memory and effector memory T cells have distinct functional properties and display different stages of *in vivo* differentiation (Sallusto et al., 2004). Here, we isolated these subpopulations from $CD4^+$ T cells from human peripheral blood, according to CD45RA and CD62L expression, and analysed them in regard to their adhesion properties and fractal dimensions. From this, a characteristic adhesion fingerprint of each subpopulation could be determined, which were further used for T cell subpopulation identification.

Percentage of in vivo differentiated T cell subpopulations in peripheral blood is donor dependent

The frequencies of subpopulations from peripheral blood of 6 donors were evaluated. The percentage of T_N was > 50 % for 4 donors. They exhibited low amounts of T_{CM}, and even less T_{EM}. For 2 donors, the percentage of T_N was < 32 %, and they displayed an elevated amount of memory subsets.

This preponderance of $CD4^+$ central memory to effector memory T cells in peripheral blood has been reported before (Campbell et al., 2001). The amount of naïve T cells in peripheral blood is dependent on age (Gabriel et al., 1993) (Salvioli et al., 2003) (Cossarizza et al., n.d.), and elevated numbers of memory T cells could be caused by acute pathogen exposure (Pepper & Jenkins, 2011). In our study, the determined percentage of T cell subsets cannot be correlated with donors' age or infection history, since all donors were anonymous. Nonetheless, it can be assumed that 4 donors were healthy and middle-aged, whereas 2 donors were probably of older age and infected by some pathogens, indicated by an increased amount of memory cells.

Fractal dimension of contour/topology and adhesion parameters are distinct for T cell subpopulations

T cell subpopulations were characterised by their morphologic characteristics. For parameter determination, isolated T cell subpopulations were seeded on ICAM-1 coated surfaces and imaged with RICM.

In these experiments a lower Df of contour/topology for undifferentiated naïve T cells than for differentiated memory cells was measured, increasing from T_{CM} to T_{EM}. This reflects a more complex adhesion topology of the cells and thus rougher plasma membrane, which can be attributed to alterations in expression patterns of adhesion molecules and cytokine release upon differentiation. Our findings are in alignment with several T cell differentiation models that propose the differentiation of naïve, non-differentiated T cells into T_{CM} and T_{EM} (see section 4.1.2), whereby T_{CM} are less differentiated than T_{EM} (Lanzavecchia & Sallusto, 2000) (Abrignani, 2015).

An increase from naïve to effector and to central memory T cells was also observed for the adhesion parameters cell area and percentage of adhesive area. This increase in cell adhesion can be correlated to the increase in LFA-1 expression upon T cell differentiation and memory T cell marker expression (see section 7.1) (Sanders et al., 1988). Interestingly, T_{CM} displayed higher values for adhesive area compared to T_{EM}. The high adhesiveness of

T_{CM} could be attributed to their property to circulate and home to T cell areas of SLOs (Cyster, 1999), which requires optimal adhesion capacities in order to exit the circulation (Murphy, 2011). In contrast, T_{EM} home to inflamed tissues, and their extravasion from the circulation is guided by several chemokine receptors and adhesion molecules (Sallusto et al., 2004). It can therefore be assumed that LFA-1 mediated adhesion to ICAM-1 is not as predominant for T_{EM} than for T_{CM}, resulting in less adhesion on ICAM-1 coated surfaces.

The excess perimeter also increased from naïve to memory T cells, which indicates enhanced cell membrane roughness, resulting from the formation of lamellipodia or filopodia (Lauffenburger & Horwith, 1997).

Compared to naïve T cells, memory T cells also exhibited an increase in eccentricity. This can be attributed to an increased migratory behaviour of memory T cells

Concluding, T_N showed significant lower values compared to memory cells for all determined parameters, and some parameters showed additional significant differences between central memory and effector memory T cells.

Thus, this method allows characterising T cell subpopulations based on their morphological features that reflect their functional properties.

It needs to be considered that the characterisation was carried out on T cell subpopulations that have been sorted with FACS by analysing an incomplete set of expressed surface receptors. Thus, we claim that each evaluated subpopulation displays a great heterogeneity within itself. We base this statement on several differentiation models that suggest the inter-conversion between T cell subsets and the existence T cell subpopulations with intermediate differentiation states that possess mixed phenotypes, migration characteristics and effector function (Mueller et al., 2013). Since the novel phenotyping method presented here employs morphological parameters that are closely linked to their functional properties, it has high potential to better resolve subpopulations than standard FACS-sorting. Our approach is therefore promising for adequately categorising subpopulations within subpopulations based on their respective differentiation states and cell functions.

Parameters of in vivo differentiated T cell subpopulations can be correlated to in vitro differentiated $CD4^+$ T cells

The observed increases in Df of contour/topology and in the adhesion parameters (area, adhesive area, eccentricity and excess perimeter) from naïve to memory T cells are in alignment with result *in vitro* differentiation experiment. Here, these parameters were also elevated upon increased CD45RO expression. Nonetheless, the absolute parameter values differ between *in vitro* and *in vivo* differentiated T cells. This can be attributed to the fact that *in vitro* differentiated CD4$^+$ T cells contained a much greater variety of T cell subsets. Also, *in vitro* stimulation of CD4$^+$ T cells induces their differentiation and effector T cell proliferation, which depends on their antigen exposure history (Kishimoto & Jutila, 1990; Sallusto et al., 2004). Thus, increased values measured in *in vitro* differentiation experiments most probably result from a preponderance of effector T cells within the CD4$^+$ T cell populations. Since effector T cells were not evaluated when analysing *in vivo* differentiated T cell subpopulations, it can only be assumed that these cells exhibit highly increased values of fractal dimensions and adhesion parameters compared to the analysed T cell subsets.

Adhesion parameters and fractal dimension of contour/topology are highly suitable for T cell subset identification

The parameters that describe *in vivo* differentiated T cell subpopulations best were determined to be area, excess perimeter, adhesion area and DF of contour/topology. These four parameters were used for T cell subset identification; and a correctness of T cell subpopulation classification of 80 % was obtained. Since RICM is a marker-free imaging method and image evaluation algorithms for extracting these parameters are fast and of low cost, this approach is highly promising for monitoring T cell subsets in human peripheral blood in clinical settings.

As discussed before, the parameters used for T cell subset identification are based on FACS-sorted subpopulations that are very heterogeneous. Thus, the incorrect subset assignment of 20 % could result from this heterogeneity of the evaluated T cell subpopulations. For example, a cell that has been defined as T_{CM} according to its CD45RA and CD62L expression could have not been classified as such, since it belongs from a further subpopulation that could not be characterized by this combination of surface markers. Therefore, including more parameters in the classification process is promising for leading to a more precise T cell subset characterisation and thus improved results for classification.

A promising parameter is the fractal dimension of cells' inner topology. In this study, Df of contour and Df of contour/topology have been evaluated, and only the latter parameter displayed significant differences for T cell subsets. Since it contains information about both contour and topology, it can be expected that Df of topology is even more explicit. Also, fractal analysis of adhesive patches could give information about membrane flexibility and membrane ordering and is therefore promising for improving characterisation. Furthermore, determining the dynamics of cells' adhesion areas is expected to improve our method, since height fluctuations of small membrane patches indicate membrane tension and bending elasticities (Sackmann & Smith, 2014) which are associated with membrane composition and therefore differentiation (Miguel et al., 2011).

The dependence of adhesion parameters and Df of contour/topology on T cell differentiation state that has been found in our study suggests that all differentiation states of T cells may be continuously represented with these parameters. Visualising the distribution of T cell subsets e.g. in an adhesion map will therefore include T cells that cannot be considered by determining expression of conventional surface markers. By interpreting the pattern of T cells in these maps, one can obtain information about the immune state of a person, and pattern changes will reveal the presence of an infection or disease that is associated with changes in the composition of T cell subsets in peripheral blood.

7.3 *In vitro* intestinal homing routes to distinguish migration characteristics of healthy and diseased CD4$^+$ T cells

To apply the concept of marker-free adhesion-based assay to distinguish CD4$^+$ T cell "fingerprints" of healthy from diseased state, we here employed an *in vitro* Graft-versus-Host-Disease (GVHD) murine model.

One of the main manifestation sites for tissue damage in GVHD is the small intestine (Shlomchik, 2007). Therefore, surfaces were generated that mimic native intestinal homing routes of CD4$^+$ T cells. The chemokine CCL25 that is expressed in the intestinal mucosa (Kunkel & Butcher, 2002) was anchored to the surface with nanometre precise spacing, together with an ICAM-1 background to mediate adhesion. These migration chips were then used to identify differences in the migratory behaviour between *in vitro* stimulated CD4$^+$ T cells that possess a GVHD phenotype and unstimulated CD4$^+$ T cells.

Functionalization approach allows orthogonal, site-specific and stable binding of CCL25 and ICAM-1

The developed surface co-functionalization approach combines Block Copolymer Micellar Nanolithography (BCML) and thiol chemistry with PEG-alkyne passivation and copper(I)-catalysed azide alkyne cycloaddition for site-specific presentation of NTA. Co^{3+} was chosen as the complex-mediating ion between NTA and His_6-tagged CCL25 and ICAM-1, since the formed $NTA(Co^{3+})His_6$ complex is highly stable (Wegner & Spatz, 2013). The developed approach presented here allows orthogonal functionalization of gold nanoparticles with CCL25 and of PEG-alkyne areas with ICAM-1.

Site specificity and stability of the functionalization was proven with AFM, QCM and fluorescent labelling. Intensity values of surfaces fluorescently labelled with ICAM-1 were lower on nanopatterned areas than on plain areas. This can be explained by ICAM-1 being coupled to the area between the gold-dots, and more protein could bind to areas without gold nanoparticles. Surfaces that were co-functionalized with both ICAM-1 and CCL25 showed an overall decrease of fluorescence intensities compared to single-functionalized surfaces. This can be explained by steric hindrance of protein and/or antibody binding. Also, double functionalized surfaces underwent more washing steps than single functionalized surfaces.

Thus, the developed functionalization approach allows the anchorage of CCL25 and ICAM-1 with very high site specificity and stability. Additionally, it allows the generation of CCL25 gradients in a highly producible and controllable manner. Our approach is therefore very advantageous compared to conventional migration assays that study T cell migration upon chemokine signalling, which mostly employ soluble chemokines.

Here, these *in vitro* migration chips that mimic native gut homing routes were used for analysing the migration behaviour healthy and diseased $CD4^+$ T cells. Here, we employed a murine *in vitro* GVHD model and compared the migration behaviour of these cells with that of healthy $CD4^+$ T cells.

To induce the GVHD phenotype, $CD4^+$ T cells were stimulated *in vitro* with retinoic acid (RA) (Iwata et al., 2004). RA is a vitamin A metabolite and has an imprinting effect on T cells for homing to the small intestine (Aoyama, Saha, Tolar, Riddle, & Veenstra, 2013; Mora & Andrian, 2006). FACS analysis of stimulated and unstimulated cells confirmed that CCR9 and integrin $\alpha4\beta7$ are upregulated in stimulated cells. Thus, RA stimulation induced a GVHD phenotype of T cells

ICAM-1 induces migration of unstimulated CD4$^+$ T cells but not of CD4$^+$ T cells with a GVHD phenotype

In order to evaluate migration induction by the adhesive background, CD4$^+$ T cells were seeded on surfaces presenting ICAM-1 and migration trajectories of unstimulated and RA-stimulated cells were compared. Previous FACS analysis of stimulated and unstimulated cells showed that > 94 % express LFA-1, which is the cognate receptor for ICAM-1 (Warnock et al., 1998). Nonetheless, it was found that stimulated cells exhibited only very low migration, whereas migration of unstimulated cells was elevated (~ 20 μm/min). This indicates that RA signalling induced arrest of T cells on ICAM-1 coated surfaces. The underlying molecular mechanisms are currently not known, but an activation of the receptor LFA-1 is possible since its binding to ICAM-1 and downstream signalling leads to F-actin cytoskeleton remodelling and therefore strengthens T cell adhesion (Porter et al., 2002).

Migration of CD4$^+$ T cells with GVHD phenotype increases due to lower CCL25 spacings

Stimulated and unstimulated CD4$^+$ T cells were seeded on surfaces presenting CCL25 with homogeneous spacings of 55 nm, 69 nm and 94 nm, together with an ICAM-1 background. The overall adhesion of stimulated and unstimulated T cells was very heterogeneous. For future experiments, adhesion could be improved by e.g. lowering the concentration of ICAM-1 in order to prevent overwhelming LFA-1 signalling that suppresses chemokine responsiveness (Dominguez & Hammer, 2014).

We found that unstimulated cell were not responsive to differences in CCL25 density, but displayed high motility rates over the determined range of CLL25 spacing. In contrast, RA-stimulated cells were less motile, but responded to lower chemokine spacings with increased migration. This could be due to their increased expression of CCR9 which mediates migration (Papadakis et al., 2000).

Here, we measured higher migration velocities than those recorded for T cells *in vivo*. For example, CD4$^+$ effector T cells migrate through the interstitial space at a speed of 5 – 10 μm/min (Weninger, Biro, & Jain, 2014), whereas naïve CD4$^+$ T cells in lymph nodes have an average velocity of ~ 11 μm/min (Miller et al., 2003). Cells *in vivo* face environmental obstacles and are therefore restricted in their migration behaviour, which does not apply for *in vitro* studies. Therefore, our results are not directly comparable with *in vivo* experiments.

In this study, we were able to show that healthy and GVHD CD4$^+$ T cells have distinct abilities to respond to CCL25 densities. The migration chips we developed here are therefore highly promising for distinguishing CD4$^+$ T cells of healthy from disease states.

In future experiments, it should be evaluated whether cells with a GVHD phenotype also differ in their *in vivo* migration characteristics. One aspect that should be paid special attention to is the migration patterns of cells. *In vivo*, naïve T cells migrate in random patterns (Brownian motion) (Miller et al., 2003), and effector cells show migration patterns that are described as Lévy walks (see section 4.1.4), which enables them to cover more territory when searching for antigenic stimulation (Harris et al., 2013; Masopust & Schenkel, 2013; Weninger et al., 2014). Analysing the migration patterns of T cells on *in vitro* migration chips could therefore serve as an additional parameter for label-free T cell subset identification. This could also give indications about an intrinsic migratory program that enables efficient T cell immune response.

A subset of CD4$^+$ T cells with GVHD phenotype is able to sense the CCL25 gradient

To evaluate cells' ability to respond to a gradient of CCL25, we performed a preliminary experiment and seeded stimulated and unstimulated CD4$^+$ T cell on surfaces presenting an ICAM-1 background and a gradient of CCL25, ranging from 64 to 90 nm over a distance of 2 mm.

Unstimulated cells showed no directional migration towards the gradient direction. In contrast, some RA-stimulated cells migrated towards smaller interligand spacings. Our results indicate that *in vitro* stimulation of CD4$^+$ T cells with RA leads to a population of cells that have various capacities to sense the CCL25 gradient.

In summary, our results showed that healthy and GVHD CD4$^+$ T cells exhibited distinct abilities to respond to varying CCL25 densities. Our *in vitro* gut homing routes are therefore suitable for identifying migration characteristics that reveal alterations in the distribution of T cell subsets that can be correlated with GVHD.

8 Outlook

In this thesis, new approaches for marker-free T cell subset identification are presented that employ imaging of T cell adhesion and/or *in vitro* homing. They are highly promising for characterising and identifying T cell subpopulations with much higher accuracy than conventional phenotyping methods, since they do not rely on analysing a complex set of surface markers, but correlate adhesion and migration characteristics with T cell differentiation. The presented work has therefore great potential for future immunodiagnostics for a variety of diseases that are associated with changes in T cell subset compositions in peripheral blood.

The first approach presented in this thesis employs Reflection Interference Contrast microscopy (RICM) imaging of T cells. From these images, characteristic adhesion and fractalic parameters are extracted, which reflect T cell differentiation states. Using this method, we are able to classify naïve, central memory and effector memory CD4$^+$ T cells with a correctness of 80%.

In contrast to conventional phenotyping methods, this method allows detecting states of intermediate differentiation since adhesion parameters and fractal dimension monitor T cell differentiation continuously. This is of great advantage when subpopulations that are highly heterogeneous need to be resolved. One of these complex subsets that are also of great interest for disease monitoring are regulatory T cells (Tregs). They are important for maintaining self-tolerance (Magenau et al., 2010), and many different Treg subtypes exist that vary in their expression of Foxp3, which is essential for their generation and function (Hori, 2003), are either of thymic or peripheral origin (Hoffmann et al., 2006) or secrete different types of effector cytokines (Abrignani, 2015). Due to this high heterogeneity, resolving Tregs with conventional marker-based phenotyping methods is very challenging.

Our results suggest that all differentiation states that are correlated with cells' functional properties can be continuously represented in adhesion maps. This will allow determining the constitution of T cell subpopulations in peripheral blood, and T cells of intermediate differentiation states can be included that have great implications for determining the immune competence states of patients or the severity of diseases (Peguillet et al., 2014).

Also, changes in T cell distribution patterns within these adhesion maps can be used for monitoring T cell subset compositions during disease therapy.

In the second part of this thesis, we apply a marker-free adhesion-based assay to distinguish healthy and diseased $CD4^+$ T cell characteristics. For this, we fabricate *in vitro* homing routes and show that $CD4^+$ T cells with a normal and a GVHD phenotype differ in their response to the gut-homing chemokine CCL25.

Concluding, imaging of T cell adhesion and/or *in vitro* homing has great potential for being applied in clinical settings for marker-free diagnosis and therapy monitoring of a variety of diseases that are associated with changes in T cell subset composition in peripheral blood, e.g. atherosclerosis and coronary artery disease (Ammirati et al., 2012), GVHD (Magenau et al., 2010; Yamashita, 2004) or chemotherapy (Peguillet et al., 2014). It has also the capability of discriminating between an activated and an exhausted immune response, which can be used as a predictive test that quantifies the immune status of a patient and estimates the course of an infection or disease.

9 References

Abercrombie, M., & Ambrose, E. J. (1958). Interference microscope studies of cell contacts in tissue culture. *Experimental Cell Research*, *15*(2), 332–345.

Abrignani, J. G. A. S. (2015). Plasticity of human CD4 T cell subsets, 1–10. doi:10.3389/fimmu.2014.00630/abstract

Ammirati, E., Cianflone, D., Vecchio, V., Banfi, M., Vermi, A. C., De Metrio, M., et al. (2012). Effector Memory T cells Are Associated With Atherosclerosis in Humans and Animal Models. *Journal of the American Heart Association*, *1*(1), 27–41. doi:10.1161/JAHA.111.000125

Aoyama, K., Saha, A., Tolar, J., Riddle, M. J., & Veenstra, R. G. (2013). Inhibiting retinoic acid signaling ameliorates graft-versus-host disease by modifying T-cell differentiation and intestinal migration. *Blood*. doi:10.1182/blood-2012-11

Aw, D., Silva, A. B., & Palmer, D. B. (2007). Immunosenescence: emerging challenges for an ageing population. *Immunology*, *120*(4), 435–446. doi:10.1111/j.1365-2567.2007.02555.x

Aydin, D., Schwieder, M., Louban, I., Knoppe, S., Ulmer, J., Haas, T. L., et al. (2009). Micro-Nanostructured Protein Arrays: A Tool for Geometrically Controlled Ligand Presentation. *Small*, *5*(9), 1014–1018. doi:10.1002/smll.200801219

Baecher-Allan, C., Brown, J. A., Freeman, G. J., & Hafler, D. A. (2001). CD4+CD25high Regulatory Cells in Human Peripheral Blood. *The Journal of Immunology*, *167*(3), 1245–1253. doi:10.4049/jimmunol.167.3.1245

Behar, T. N. (2001). Analysis of Fractal Dimension of O2A Glial Cells Differentiating in Vitro. *Methods*, *24*(4), 331–339. doi:10.1006/meth.2001.1203

Block, H., Maertens, B., Spriestersbach, A., Brinker, N., Kubicek, J., Fabis, R., et al. (2009). *Chapter 27 - Immobilized-Metal Affinity Chromatography (IMAC): A Review*. *Methods in Enzymology* (1st ed., Vol. 463, pp. 439–473). Elsevier Inc. doi:10.1016/S0076-6879(09)63027-5

Blümmel, J., Perschmann, N., Aydin, D., Drinjakovic, J., Surrey, T., López-García, M., et al. (2007). Protein repellent properties of covalently attached PEG coatings on nanostructured SiO2-based interfaces. *Biomaterials*, *28*(32), 4739–4747. doi:10.1016/j.biomaterials.2007.07.038

Bono, M. R., Elgueta, R., Sauma, D., Pino, K., Osorio, F., Michea, P., et al. (2007). The essential role of chemokines in the selective regulation of lymphocyte homing. *Cytokine & Growth Factor Reviews*, *18*(1-2), 33–43. doi:10.1016/j.cytogfr.2007.01.004

Brede, C., Friedrich, M., Jordán-Garrote, A.-L., Riedel, S. S., Bäuerlein, C. A., Heinze, K. G., et al. (2012). Mapping immune processes in intact tissues at cellular resolution. *Journal of Clinical Investigation*, *122*(12), 4439–4446. doi:10.1172/JCI65100DS1

Butcher, E. C., & Picker, L. J. (1996). Lymphocyte homing and homeostasis. *Science*.

Campbell, J. J., Murphy, K. E., Kunkel, E. J., Brightling, C. E., Soler, D., Shen, Z., et al. (2001). CCR7 Expression and Memory T Cell Diversity in Humans. *The Journal of Immunology*, *166*(2), 877–884. doi:10.4049/jimmunol.166.2.877

Chao, C. C., Jensen, R., & Dailey, M. O. (1997). Mechanisms of L-selectin regulation by activated T cells. *Journal of immunology (Baltimore, Md. : 1950)*, *159*(4), 1686–1694.

Cossarizza, A., Ortolani, C., Paganelli, R., Barbieri, D., Monti, D., Sansoni, P., et al. (n.d.). CD45 isoforms expression on CD4+ and CD8+ T cells throughout life, from newborns to centenarians: Implications for T cell memory. *Mechanisms of Ageing and Development*, *86*(3), 173–195. doi:10.1016/0047-6374(95)01691-0

Cyster, J. G. (1999). Chemokines and Cell Migration in Secondary Lymphoid Organs. *Science*, *286*(5447), 2098–2102. doi:10.1126/science.286.5447.2098

Cyster, J. G. (2005). CHEMOKINES, SPHINGOSINE-1-PHOSPHATE, AND CELL MIGRATION IN SECONDARY LYMPHOID ORGANS. *Annual Review of Immunology*, *23*(1), 127–159. doi:10.1146/annurev.immunol.23.021704.115628

Davies, P. F., Robotewskyj, A., & Griem, M. L. (1993). Endothelial cell adhesion in real time. Measurements in vitro by tandem scanning confocal image analysis. *Journal of Clinical …*.

Dominguez, G. A., & Hammer, D. A. (2014). Effect of adhesion and chemokine presentation on T-lymphocyte haptokinesis. *Integrative Biology*, *6*(9), 862. doi:10.1039/C4IB00094C

Dransfield, I., Cabanas, C., & Craig, A. (1992). Divalent cation regulation of the function of the leukocyte integrin LFA-1. *The Journal of Cell Biology, 116(1),219-226*.

Gabriel, H., Schmitt, B., & Kindermann, W. (1993). Age-related increase of CD45RO+ lymphocytes in physically active adults. *European journal of immunology*, *23*(10), 2704–2706. doi:10.1002/eji.1830231049

Gingell, D., & Todd, I. (1979). Interference reflection microscopy. A quantitative theory for image interpretation and its application to cell-substratum separation measurement. *Biophysj*, *26*(3), 507–526. doi:10.1016/S0006-3495(79)85268-6

Goronzy, J. J., & Weyand, C. M. (2013). Understanding immunosenescence to improve responses to vaccines. *Nature Publishing Group*, *14*(5), 428–436. doi:10.1038/ni.2588

Green, J. M., Karpitskiy, V., Kimzey, S. L., & Shaw, A. S. (2000). Coordinate Regulation of T Cell Activation by CD2 and CD28. *The Journal of Immunology*, *164*(7), 3591–3595. doi:10.4049/jimmunol.164.7.3591

Gutcher, I., & Becher, B. (2007). APC-derived cytokines and T cell polarization in autoimmune inflammation. *Journal of Clinical Investigation*, *117*(5), 1119–1127. doi:10.1172/JCI31720

Harris, T. H., Banigan, E. J., Christian, D. A., Konradt, C., Wojno, E. D. T., Norose, K., et al. (2013). Generalized Lévy walks and the role of chemokines in migration of effector CD8+ T cells. *Nature*, *486*(7404), 545–548. doi:10.1038/nature11098

Haubner, R., Gratias, R., & Diefenbach, B. (1996). Structural and functional aspects of RGD-containing cyclic pentapeptides as highly potent and selective integrin αvβ3 antagonists. *Journal of the …*.

Hirschfeld-Warneken, V. C. (2009). Induction of cell posarization and directed migration by nanonoscale gradients of adhesive ligands. PhD Thesis, Heidelberg University

Hirschfeld-Warneken, V. C., Arnold, M., Cavalcanti-Adam, A., López-García, M., Kessler, H., & Spatz, J. P. (2008). Cell adhesion and polarisation on molecularly defined spacing gradient surfaces of cyclic RGDfK peptide patches. *European journal of cell biology*, *87*(8-9), 743–750. doi:10.1016/j.ejcb.2008.03.011

Hoffmann, P., Eder, R., Boeld, T. J., Doser, K., Piseshka, B., Andreesen, R., & Edinger, M. (2006). Only the CD45RA+ subpopulation of CD4+CD25high T cells gives rise to homogeneous regulatory T-cell lines upon in vitro expansion. *Blood*, *108*(13), 4260–4267. doi:10.1182/blood-2006-06-027409

Hori, S. (2003). Control of Regulatory T Cell Development by the Transcription Factor Foxp3. *Science*, *299*(5609), 1057–1061. doi:10.1126/science.1079490

Hosseini, B. H., Louban, I., Djandji, D., Wabnitz, G. H., Deeg, J., Bulbuc, N., et al. (2009). Immune synapse formation determines interaction forces between T cells and antigen-presenting cells measured by atomic force microscopy. *Proceedings of the National Academy of Sciences*, *106*(42), 17852–17857. doi:10.1073/pnas.0905384106

Hviid, L., Odum, N., & Theander, T. G. (1993). The relation between T-cell expression of LFA-1 and immunological memory. *Immunology*, *78*(2), 237–243.

Iwata, M., Hirakiyama, A., Eshima, Y., Kagechika, H., Kato, C., & Song, S.-Y. (2004). Retinoic acid imprints gut-homing specificity on T cells. *Immunity*, *21*(4), 527–538.

Jacobi, A., Otto, O., Kräter, M., Wobus, M., Herold, C., Klaue, D., et al. (n.d.). Marker-free characterization of human hematopoietic stem and progenitor cells by high-throughput mechanical phenotyping. *ISCCR Stockholm Conference Paper*

Kaech, S. M., & Cui, W. (2012). Transcriptional control of effector and memory CD8+ T cell differentiation. *Nature Reviews Immunology*, *12*(11), 749–761. doi:10.1038/nri3307

Kansal, A. R., Truskett, T. M., & Torquato, S. (2000). Nonequilibrium hard-disk packings with controlled orientational order. *The Journal of Chemical Physics*, *113*(12), 4844. doi:10.1063/1.1289238

Karabacak, N. M., Spuhler, P. S., Fachin, F., Lim, E. J., Pai, V., Ozkumur, E., et al. (2014). Microfluidic, marker-free isolation of circulating tumor cells from blood samples. *Nature Protocols*, *9*(3), 694–710. doi:10.1038/nprot.2014.044

Keenan, T. M., & Folch, A. (2008). Biomolecular gradients in cell culture systems. *Lab on a chip*, *8*(1), 34–57. doi:10.1039/B711887B

Kishimoto, T. K., & Jutila, M. A. (1990). Identification of a human peripheral lymph node homing receptor: a rapidly down-regulated adhesion molecule. *Proc. Natl. Acad. Sci. USA*, 87, 2244-2248

Klein, K., Maier, T., Hirschfeld-Warneken, V. C., & Spatz, J. P. (2013). Marker-Free Phenotyping of Tumor Cells by Fractal Analysis of Reflection Interference Contrast Microscopy Images. *Nano Letters*, *13*(11), 5474–5479. doi:10.1021/nl4030402

Koch, S., Walles, H., Krause, K. H., Baquié, M., Hansmann, M. L., & Schuetze, K. (2013). Novel cell identification: markerfree and suitable for living cells. In V. Deckert & N. Ramanujam (Eds.), (Vol. 8798, p. 87980J). Presented at the European Conferences on Biomedical Optics, SPIE. doi:10.1117/12.2033542

Krafft, C., Salzer, R., Soff, G., & Meyer-Hermann, M. (2005). Identification of B and T cells in human spleen sections by infrared microspectroscopic imaging. *Cytometry Part A*, *64A*(2), 53–61. doi:10.1002/cyto.a.20117

Kunkel, E. J., & Butcher, E. C. (2002). Chemokines and the tissue-specific migration of lymphocytes. *Immunity*, *16*(1), 1–4.

Lagunas, A., Comelles, J., Martínez, E., Prats-Alfonso, E., Acosta, G. A., Albericio, F., & Samitier, J. (2012). Cell adhesion and focal contact formation on linear RGD molecular gradients: study of non-linear concentration dependence effects. *Nanomedicine : nanotechnology, biology, and medicine*, *8*(4), 432–439. doi:10.1016/j.nano.2011.08.001

Lanzavecchia, A., & Sallusto, F. (2000). Dynamics of T lymphocyte responses: intermediates, effectors, and memory cells. *Science,* 290, 92-96. doi:10.1016/j.vaccine.2015.04.051

Lauffenburger, D. A., & Horwith, A. F. (1997). Cell Migration:A Physically Integrated Molecular Process, *Cell,* 84, 359-369.

Leisenring, W. M. (2006). An acute graft-versus-host disease activity index to predict survival after hematopoietic cell transplantation with myeloablative conditioning regimens. *Blood*, *108*(2), 749–755. doi:10.1182/blood-2006-01-0254

Limozin, L., & Sengupta, K. (2009). Quantitative Reflection Interference Contrast Microscopy (RICM) in Soft Matter and Cell Adhesion. *ChemPhysChem*, *10*(16), 2752–2768. doi:10.1002/cphc.200900601

Lin, F., & Butcher, E. C. (2006). T cell chemotaxis in a simple microfluidic device. *Lab on a chip*, *6*(11), 1462–1469. doi:10.1039/b607071j

Lohmüller, T., Aydin, D., Schwieder, M., Morhard, C., Louban, I., Pacholski, C., & Spatz, J. P. (2011). Nanopatterning by block copolymer micelle nanolithography and bioinspired applications. *Biointerphases*, *6*(1), MR1. doi:10.1116/1.3536839

Lopes, R., & Betrouni, N. (2009). Fractal and multifractal analysis: A review. *Medical Image Analysis*, *13*(4), 634–649. doi:10.1016/j.media.2009.05.003

Losa, G. A. (2002). Fractal morphometry of cell complexity. *Rivista di biologia*, *95*(2), 239–258.

Losa, G. A. (2011). Fractals in biology and medicine. *Encyclopedia of Molecular Cell Biology and Molecular Medicine*.

Luster, A. D., Alon, R., & Andrian, von, U. H. (2005). Immune cell migration in inflammation: present and future therapeutic targets. *Nature Immunology*, *6*(12), 1182–1190. doi:10.1038/ni1275

Magenau, J. M., Qin, X., Tawara, I., Rogers, C. E., Kitko, C., Schlough, M., et al. (2010). Frequency of CD4+CD25hiFOXP3+ Regulatory T Cells Has Diagnostic and Prognostic Value as a Biomarker for Acute Graft-versus-Host-Disease. *Biology of Blood and Marrow Transplantation*, *16*(7), 907–914. doi:10.1016/j.bbmt.2010.02.026

Mandelbrot, B. (1967). How long is the coast of britain? Statistical self-similarity and fractional dimension. *Science*, *156*(3775), 636–638. doi:10.1126/science.156.3775.636

Mandelbrot, B. B. (1983). *The Fractal Geometry of Nature*. Macmillan.

Mashiah, A., Wolach, O., Sandbank, J., Uziel, O., Raanani, P., & Lahav, M. (2008). Lymphoma and Leukemia Cells Possess Fractal Dimensions That Correlate with Their Biological Features. *Acta Haematologica*, *119*(3), 142–150. doi:10.1159/000125551

Masopust, D., & Schenkel, J. M. (2013). The integration of T cell migration, differentiation and function. *Nature Publishing Group*, *13*(5), 309–320. doi:10.1038/nri3442

Meier, J., Roberts, C., Avent, K., Hazlett, A., Berrie, J., Payne, K., et al. (2013). Fractal Organization of the Human T Cell Repertoire in Health and after Stem Cell Transplantation. *Biology of Blood and Marrow Transplantation*, *19*(3), 366–377. doi:10.1016/j.bbmt.2012.12.004

Michie, C. A., McLean, A., Alcock, C., & Beverley, P. C. (1992). Lifespan of human lymphocyte subsets defined by CD45 isoforms. *Nature*, *360*(6401), 264–265. doi:10.1038/360264a0

Miguel, L., Owen, D. M., Lim, C., Liebig, C., Evans, J., Magee, A. I., & Jury, E. C. (2011). Primary Human CD4+ T Cells Have Diverse Levels of Membrane Lipid Order That Correlate with Their Function. *The Journal of Immunology*, *186*(6), 3505–3516. doi:10.4049/jimmunol.1002980

Miller, M. J., Wei, S. H., Cahalan, M. D., & Parker, I. (2003). Autonomous T cell trafficking examined in vivo with intravital two-photon microscopy. *Proceedings of the National Academy of Sciences of the United States of America*, *100*(5), 2604–2609. doi:10.1073/pnas.2628040100

Momburg, F., Fuchs, S., Drexler, J., Busch, R., Post, M., Hämmerling, G. J., & Adorini, L. (1993). Epitope-specific enhancement of antigen presentation by invariant chain. *The Journal of experimental medicine*, *178*(4), 1453–1458.

Mora, J. R., & Andrian, von, U. H. (2006). T-cell homing specificity and plasticity: new concepts and future challenges. *Trends in Immunology*, *27*(5), 235–243. doi:10.1016/j.it.2006.03.007

Mueller, S. N., Gebhardt, T., Carbone, F. R., & Heath, W. R. (2013). Memory T Cell Subsets, Migration Patterns, and Tissue Residence. *Annual Review of Immunology*, *31*(1), 137–161. doi:10.1146/annurev-immunol-032712-095954

Murphy, K. (2011). *Janeway's Immunobiology, Eighth Edition*. Garland Science.

Naeim, F., Moatamed, F., & Sahimi, M. (1996). Morphogenesis of the bone marrow: fractal structures and diffusion-limited growth. *Blood*, *87*(12), 5027–5031.

Nair, S., Bayer, W., Ploquin, M. J., Kassiotis, G., Hasenkrug, K. J., & Dittmer, U. (2011). Distinct roles of CD4+ T cell subpopulations in retroviral immunity: lessons from the Friend virus mouse model. *Retrovirology*, *8*(1), 76. doi:10.1186/1742-4690-8-76

Nelson, J., McFerran, N. V., Pivato, G., Chambers, E., Doherty, C., Steele, D., & Timson, D. J. (2008). The 67 kDa laminin receptor: structure, function and role in disease. *Bioscience Reports*, *28*(1), 33. doi:10.1042/BSR20070004

Nolte, D. D. (2012). *Optical Interfoerometry for Biology and Medicine*. (T. Vo-Dinh, Ed.). New York: Springer Science and Business Media.

Nomizu, M., Weeks, B. S., Weston, C. A., Kim, W. H., Kleinman, H. K., & Yamada, Y. (1995). Structure-activity study of a laminin alpha 1 chain active peptide segment Ile-Lys-Val-Ala-Val (IKVAV). *FEBS letters*, *365*(2-3), 227–231.

Okada, R., Kondo, T., Matsuki, F., Takata, H., & Takiguchi, M. (2008). Phenotypic classification of human CD4+ T cell subsets and their differentiation. *International Immunology*, *20*(9), 1189–1199. doi:10.1093/intimm/dxn075

Okumura, M., Fujii, Y., Takeuchi, Y., & Inada, K. (1993). Age-related accumulation of LFA-1high cells in a CD8+ CD45RAhigh T cell population. *European journal of Immunology,* 23, 1057-1063.

Otto, O., Rosendahl, P., Mietke, A., Golfier, S., Herold, C., Klaue, D., et al. (2015). Real-time deformability cytometry: on-the-fly cell mechanical phenotyping. *Nature Methods*, *12*(3), 199–202. doi:10.1038/nmeth.3281

Paczesny, S. (2013). Discovery and validation of graft-versus-host disease biomarkers. *Blood*, *121*(4), 585–594. doi:10.1182/blood-2012-08-355990

Papadakis, K. A., Prehn, J., Nelson, V., Cheng, L., Binder, S. W., Ponath, P. D., et al. (2000). The Role of Thymus-Expressed Chemokine and Its Receptor CCR9 on Lymphocytes in the Regional Specialization of the Mucosal Immune System. *The Journal of Immunology*, *165*(9), 5069–5076. doi:10.4049/jimmunol.165.9.5069

Patel, D. D., Koopmann, W., Imai, T., Whichard, L. P., Yoshie, O., & Krangel, M. S. (2001). Chemokines Have Diverse Abilities to Form Solid Phase Gradients. *Clinical Immunology*, *99*(1), 43–52. doi:10.1006/clim.2000.4997

Peguillet, I., Milder, M., Louis, D., Vincent-Salomon, A., Dorval, T., Piperno-Neumann, S., et al. (2014). High Numbers of Differentiated Effector CD4 T Cells Are Found in Patients with Cancer and Correlate with Clinical Response after Neoadjuvant Therapy of Breast Cancer. *Cancer Research*, *74*(8), 2204–2216. doi:10.1158/0008-5472.CAN-13-2269

Pepper, M., & Jenkins, M. K. (2011). Origins of CD4+ effector and central memory T cells. *Nature Immunology*, *131*(6), 467–471. doi:10.1038/ni.2038

Pfaff, M. (1997). Recognition Sites of RGD-Dependent Integrins. In *link.springer.com* (pp. 101–121). Boston, MA: Springer US. doi:10.1007/978-1-4757-4064-6_4

Pierres, A., Benoliel, A. M., & Bongrand, P. (2002). Cell fitting to adhesive surfaces: a prerequisite to firm attachment and subsequent events. *Eur Cell Mater,* 3, 31-45.

Porter, J. C., Bracke, M., Smith, A., Davies, D., & Hogg, N. (2002). Signaling through integrin LFA-1 leads to filamentous actin polymerization and remodeling, resulting in enhanced T cell adhesion. *Journal of immunology (Baltimore, Md. : 1950)*, *168*(12), 6330–6335.

Rädler, J., & Sackmann, E. (1993). Imaging optical thicknesses and separation distances of phospholipid vesicles at solid surfaces. *J. Phys. II France*, *3*(5), 727–748.

Reinhardt, R. L., Khoruts, A., Merica, R., Zell, T., & Jenkins, M. K. (2001). Visualizing the generation of memory CD4 T cells in the whole body. *Nature*, 410, 101-105

Robbins, P. D., & Morelli, A. E. (2014). Regulation of immune responses by extracellular vesicles. *Nature Publishing Group*, *14*(3), 195–208. doi:10.1038/nri3622

Rose, D. M., Han, J., & Ginsberg, M. H. (2002). α4 integrins and the immune response. *Immunological reviews*, *186,* 118-124

Russ, B. E., Prier, J. E., Rao, S., & Turner, S. J. (2013). T cell immunity as a tool for studying epigenetic regulation of cellular differentiation. *Frontiers in genetics*, *4*, 218. doi:10.3389/fgene.2013.00218

Russell, D. A., Hanson, J. D., & Ott, E. (1980). Dimension of strange attractors. *Physical Review Letters,* 45(14), 1175-1178

Sackmann, E., & Smith, A.-S. (2014). Physics of cell adhesion: some lessons from cell-mimetic systems. *Soft Matter*, *10*(11), 1644. doi:10.1039/c3sm51910d

Sallusto, F., Geginat, J., & Lanzavecchia, A. (2004). Central memory and effector memory T cell subsets: function, generation, and maintenance. *Annual Review of Immunology*. doi:10.1146/annurev.immunol.22.012703.104702

Sallusto, F., Lenig, D., Förster, R., Lipp, M., & Lanzavecchia, A. (1999). Two subsets of memory T lymphocytes with distinct homing potentials and effector functions. *Nature*, *401*(6754), 708–712. doi:10.1038/44385

Salvioli, S., Capri, M., Scarcella, E., Mangherini, S., Faranca, I., Volterra, V., et al. (2003). Age-dependent changes in the susceptibility to apoptosis of peripheral blood CD4+ and CD8+ T lymphocytes with virgin or memory phenotype. *Mechanisms of Ageing and Development*, *124*(4), 409–418. doi:10.1016/S0047-6374(03)00016-2

Sanders, M. E., Makgoba, M. W., & Sharrow, S. O. (1988). Human memory T lymphocytes express increased levels of three cell adhesion molecules (LFA-3, CD2, and LFA-1) and three other molecules (UCHL1, CDw29, and …. *The Journal of Immunology,* 140(5), 1401-1407.

Schenk, F. C., Boehm, H., Spatz, J. P., & Wegner, S. V. (2014). Dual-Functionalized Nanostructured Biointerfaces by Click Chemistry. *Langmuir*, *30*(23), 6897–6905. doi:10.1021/la500766t

Schilling, J., Sengupta, K., Goennenwein, S., Bausch, A. R., & Sackmann, E. (2004). Absolute interfacial distance measurements by dual-wavelength reflection interference contrast microscopy. *Physical Review E*, *69*(2), 021901. doi:10.1103/PhysRevE.69.021901

Schindelin, J., Arganda-Carreras, I., Frise, E., & Kaynig, V. (2012). Fiji: an open-source platform for biological-image analysis. *Nature*. doi:10.1038/nmeth.1985

Seder, R. A., & Ahmed, R. (2003). Similarities and differences in CD4+ and CD8+ effector and memory T cell generation. *Nature Immunology*. 4(9), 835-842

Segundo, D. S., Fernández-Fresnedo, G., Gago, M., Beares, I., Ruiz-Criado, J., González, M., et al. (2010). Kidney Transplant Recipients Show an Increase in the Ratio of T-Cell Effector Memory/Central Memory as Compared to Nontransplant Recipients on the Waiting List. *TPS*, *42*(8), 2877–2879. doi:10.1016/j.transproceed.2010.07.072

Sekhavati, F., Endele, M., Rappl, S., Marel, A.-K., Schroeder, T., & dler, J. O. R. X. (2015). Marker-free detection of progenitor cell differentiation by analysis of Brownian motion in micro-wells. *Integrative Biology*, *7*, 178–183.

doi:10.1039/C4IB00158C

Shlomchik, W. D. (2007). Graft-versus-host disease. *Nature Publishing Group*, *7*(5), 340–352. doi:10.1038/nri2000

Smith, K. A. (1988). Interleukin-2: inception, impact, and implications. *Science*, *240*(4856), 1169–1176.

Smith, T. G., Lange, G. D., & Marks, W. B. (1996). Fractal methods and results in cellular morphology--dimensions, lacunarity and multifractals. *Journal of neuroscience methods*, *69*(2), 123–136. doi:10.1016/S0165-0270(96)00080-5

Spatz, J. P., Mössmer, S., Hartmann, C., Möller, M., Herzog, T., Krieger, M., et al. (2000). Ordered deposition of inorganic clusters from micellar block copolymer films. *Langmuir*, *16*(2), 407–415. doi:10.1021/la990070n

Springer, T. A. (1990). Adhesion receptors of the immune system. *Nature*, *346*(6283), 425–434. doi:10.1038/346425a0

Stachowiak, A. N., Wang, Y., Huang, Y. C., & Irvine, D. J. (2006). Homeostatic Lymphoid Chemokines Synergize with Adhesion Ligands to Trigger T and B Lymphocyte Chemokinesis. *The Journal of Immunology*, *177*(4), 2340–2348. doi:10.4049/jimmunol.177.4.2340

Stewart, M. P., Cabanas, C., & Hogg, N. (1996). T cell adhesion to intercellular adhesion molecule-1 (ICAM-1) is controlled by cell spreading and the activation of integrin LFA-1. *Journal of immunology (Baltimore, Md. : 1950)*, *156*(5), 1810–1817.

Takagi, J. (2004). Structural basis for ligand recognition by RGD (Arg-Gly-Asp)-dependent integrins. *Biochemical Society transactions*, *32*(Pt3), 403–406. doi:10.1042/BST0320403

Tashiro, K., Sephel, G. C., Weeks, B., Sasaki, M., Martin, G. R., Kleinman, H. K., & Yamada, Y. (1989). A synthetic peptide containing the IKVAV sequence from the A chain of laminin mediates cell attachment, migration, and neurite outgrowth. *The Journal of biological chemistry*, *264*(27), 16174–16182.

Triplett, T. A., Curti, B. D., Bonafede, P. R., Miller, W. L., Walker, E. B., & Weinberg, A. D. (2012). Defining a functionally distinct subset of human memory CD4+ T cells that are CD25POS and FOXP3NEG. *European journal of immunology*, *42*(7), 1893–1905. doi:10.1002/eji.201242444

Verschueren, H. (1985). Interference reflection microscopy in cell biology: methodology and applications. *Journal of Cell Science*, *75*, 279–301.

Wagner, C., Kotsougiani, D., Pioch, M., Prior, B., Wentzensen, A., & Hänsch, G. M. (2008). T lymphocytes in acute bacterial infection: increased prevalence of CD11b +cells in the peripheral blood and recruitment to the infected site. *Immunology*, *125*(4), 503–509. doi:10.1111/j.1365-2567.2008.02863.x

Warnock, R. A., Askari, S., Butcher, E. C., & Andrian, von, U. H. (1998). Molecular mechanisms of lymphocyte homing to peripheral lymph nodes. *The Journal of experimental medicine*, *187*(2), 205–216.

Weeks, B. S., Holloway, E., Klotman, P. E., Akiyama, S. K., Schnaper, H. W., & Kleinman, H. K. (1994). 12-O-tetradecanoylphorbol 13-acetate stimulates human T-lymphocyte adherence to the fibronectin RGD domain and the laminin IKVAV domain. *Cellular immunology*, *153*(1), 94–104. doi:10.1006/cimm.1994.1008

Wegner, S. V., & Spatz, J. P. (2013). Cobalt(III) as a Stable and Inert Mediator Ion between NTA and His6-Tagged Proteins. *Angewandte Chemie International Edition*, *52*(29), 7593–7596. doi:10.1002/anie.201210317

Weninger, W., Biro, M., & Jain, R. (2014). Leukocyte migration in the interstitial space of non-lymphoid organs. *Nature Publishing Group*, *14*(4), 232–246. doi:10.1038/nri3641

Wherry, E. J. (2011). T cell exhaustion. *Nature Publishing Group*, *131*(6), 492–499.

doi:10.1038/ni.2035

Wood, B. R., Tait, B., & McNaughton, D. (2000). Fourier-transform infrared spectroscopy as a tool for detecting early lymphocyte activation: a new approach to histocompatibility matching. *Human immunology*, *61*(12), 1307–1314.

Woodland, D. L., & Kohlmeier, J. E. (2009). Migration, maintenance and recall of memory T cells in peripheral tissues. *Nature Publishing Group*, *9*(3), 153–161. doi:10.1038/nri2496

Woolf, E., Grigorova, I., Sagiv, A., Grabovsky, V., Feigelson, S. W., Shulman, Z., et al. (2007). Lymph node chemokines promote sustained T lymphocyte motility without triggering stable integrin adhesiveness in the absence of shear forces. *Nature Immunology*, *8*(10), 1076–1085. doi:10.1038/ni1499

Wu, X., Wu, J., Li, H., Legler, D. F., Marshall, A. J., & Lin, F. (2015). Analysis of CCR7 mediated T cell transfectant migration using a microfluidic gradient generator. *Journal of Immunological Methods*, *419*(C), 9–17. doi:10.1016/j.jim.2015.02.008

Yamashita, K. (2004). Severe chronic graft-versus-host disease is characterized by a preponderance of CD4+ effector memory cells relative to central memory cells. *Blood*, *103*(10), 3986–3988. doi:10.1182/blood-2003-09-3286

Yang, Y., Jun, C.-D., Liu, J.-H., Zhang, R., Joachimiak, A., Springer, T. A., & Wang, J.-H. (2004). Structural basis for dimerization of ICAM-1 on the cell surface. *Molecular cell*, *14*(2), 269–276.

Yi, J. S., Cox, M. A., & Zajac, A. J. (2010). T-cell exhaustion: characteristics, causes and conversion. *Immunology*, *129*(4), 474–481. doi:10.1111/j.1365-2567.2010.03255.x

Zabel, B. A., Agace, W. W., & Campbell, J. J. (1999). Human G protein–coupled receptor GPR-9-6/CC chemokine receptor 9 is selectively expressed on intestinal homing T lymphocytes, mucosal lymphocytes, and tymocytes is required for thymus-expressed chemokine-mediated chemotaxis. *The Journal of Experimental Medicine,* 190(9), 1241-1255.

10 Appendix

a) *MATLAB script for image processing*

```
22.07.15 16:41  /Users/mariahamme.../RICM_evaluation_md.m   1 of 6

% Image Processing for images of phase contrast and RICM

% Author: Maria Danner
% script based on evaluation from Christine Selhuber-Unkel, Heidelberg University,
% 2005 and Katharina Klein, Heidelberg University 2009


% enter path names and image names
pathname_outlines=↙
['/Users/mariahammer/Documents/Doktorarbeit/evaluation/fractal_analysis/150528_subpopu↙
lations/Tn/outlines/'];
pathname_results =↙
['/Users/mariahammer/Documents/Doktorarbeit/evaluation/fractal_analysis/150528_subpopu↙
lations/Tn/results/'];
pathname_fraclac =↙
['/Users/mariahammer/Documents/Doktorarbeit/evaluation/fractal_analysis/150528_subpopu↙
lations/Tn/fraclac/'];


basisfilename='Tn_';

    i=025
        % set image number to be calculated
    fudgeFactor = 0.75
        % set sensitivity for edge detection
    small_size=2000;
        % define object size for deletion

    filename=[basisfilename,sprintf('%.3d',i),'.tif']
        %NUM2STR Convert numbers to a string. and sprintf('%.2d',i) creates
        %two-digit-numbers (in case of 1-9 it puts 0 in front of it!)

    I=imread↙
(['/Users/mariahammer/Documents/Doktorarbeit/evaluation/fractal_analysis/150528_subpop↙
ulations/Tn/images','/',filename]);
        % read image

    nametxt=[pathname_fraclac basisfilename 'results.txt'];
    nametxt2=[pathname_results basisfilename sprintf('%.3d',i) 'pixel_height.txt'];
    nametxt3 = [pathname_results basisfilename sprintf('%.3d',i) 'matrix_height.txt'];
    nametxt4 = [pathname_results basisfilename sprintf('%.3d',i) 'matrix_intensities.↙
txt'];
        % creates file names to save data in

    % if results_tab exists from evaluation before: delete results_tab
    exist results_tab
    if ans == 1
        if length(results_tab) > i
            clear results_tab;
        end
    end


    % read result file if it exists
    exist results_tab
    if ans == 0
       exist (nametxt, 'file')
        % if results table does not exist and file exists, read table from
        % file
       if ans == 2
           test = readtable(nametxt, 'Delimiter', '\t');
           Ttab = table2cell(test);
```

```
        Ttab = cell2mat(Ttab);
        results_tab = Ttab;
    end
end


%%%%%%%%%%%%%%%%%%%%%%%%%
%%% OUTLINE DETECTION %%%
%%%%%%%%%%%%%%%%%%%%%%%%%

I=I(:,:,1);
    % take first image from stack; here: I=(images(:,:,1,i));
figure(1), imshow(I), title('original image');

% Cell detection: find edges via intensity gradients and

% define threshold for creating a binary mask
[junk threshold] = edge(I, 'sobel');  % specifies sobel method

% DEFINE FUDGEFACTOR FOR CELL EDGE DETECTION
BWs = edge(I,'sobel', threshold * fudgeFactor);
    % BW = edge (I) takes intensities, returns BW-image of same size,
    % with 1 for edges found and 0 elsewhere
    % all edges that are stronger than (threshold*fudgeFactor) are ignored

figure(2), imshow(BWs), title('binary gradient mask');

% Fill Gaps: create masks
se90 = strel('line', 3, 90);
se0 = strel('line', 3, 0);
    % strel creates morphological structuring elements
    % se90: mask to dilate vertical structure elements
    % se0: mask to dilate horizontal elements
    % 3: length of baseline; 0: angle

% Dilate the Image by mask application
BWsdil = imdilate(BWs, [se90 se0]);
figure(3), imshow(BWsdil), title('dilated gradient mask');

% Fill Interior Gaps
BWdfill = imfill(BWsdil, 'holes');
figure(4), imshow(BWdfill), title('binary image with filled holes');

% Remove objects that are connected with the border
BWnobord = imclearborder(BWdfill, 4);
    % 4 specifies connectivity: diagonal connections are cleared also
    % figure(5), imshow(BWnobord), title('cleared border image');

% Smooth the Object using Diamant-Structur-Element twice
seD = strel('diamond',2);
    % 2: half-width of diamon-shaped matrix of Ones
BWfinal = imerode(BWnobord,seD);
BWfinal = imerode(BWfinal,seD);
figure(6), imshow(BWfinal), title('segmented image');

% removing of small particles smaller than small_size
BWfinal=bwareaopen(BWfinal,small_size);
    % bwareaopen removes small objects from binary image
figure(7), imshow(BWfinal), title('final black/white image');

% Outline the Cell in Original Image
BWoutline = bwperim(BWfinal);
```

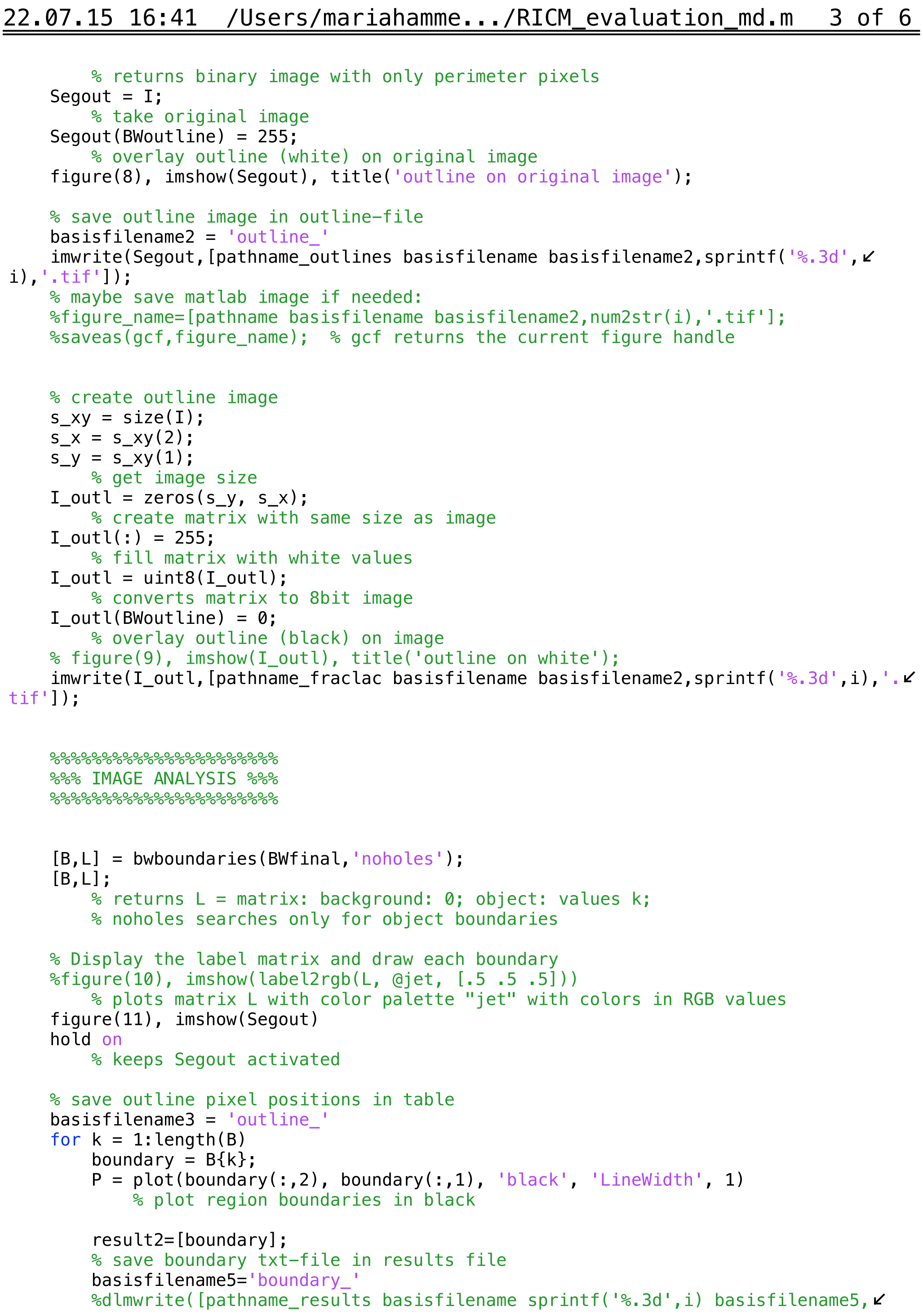

```
22.07.15 16:41  /Users/mariahamme.../RICM_evaluation_md.m   3 of 6

        % returns binary image with only perimeter pixels
    Segout = I;
        % take original image
    Segout(BWoutline) = 255;
        % overlay outline (white) on original image
    figure(8), imshow(Segout), title('outline on original image');

    % save outline image in outline-file
    basisfilename2 = 'outline_'
    imwrite(Segout,[pathname_outlines basisfilename basisfilename2,sprintf('%.3d',↙
i),'.tif']);
    % maybe save matlab image if needed:
    %figure_name=[pathname basisfilename basisfilename2,num2str(i),'.tif'];
    %saveas(gcf,figure_name);  % gcf returns the current figure handle


    % create outline image
    s_xy = size(I);
    s_x = s_xy(2);
    s_y = s_xy(1);
        % get image size
    I_outl = zeros(s_y, s_x);
        % create matrix with same size as image
    I_outl(:) = 255;
        % fill matrix with white values
    I_outl = uint8(I_outl);
        % converts matrix to 8bit image
    I_outl(BWoutline) = 0;
        % overlay outline (black) on image
    % figure(9), imshow(I_outl), title('outline on white');
    imwrite(I_outl,[pathname_fraclac basisfilename basisfilename2,sprintf('%.3d',i),'.↙
tif']);


    %%%%%%%%%%%%%%%%%%%%%%
    %%% IMAGE ANALYSIS %%%
    %%%%%%%%%%%%%%%%%%%%%%


    [B,L] = bwboundaries(BWfinal,'noholes');
    [B,L];
        % returns L = matrix: background: 0; object: values k;
        % noholes searches only for object boundaries

    % Display the label matrix and draw each boundary
    %figure(10), imshow(label2rgb(L, @jet, [.5 .5 .5]))
        % plots matrix L with color palette "jet" with colors in RGB values
    figure(11), imshow(Segout)
    hold on
        % keeps Segout activated

    % save outline pixel positions in table
    basisfilename3 = 'outline_'
    for k = 1:length(B)
        boundary = B{k};
        P = plot(boundary(:,2), boundary(:,1), 'black', 'LineWidth', 1)
            % plot region boundaries in black

        result2=[boundary];
        % save boundary txt-file in results file
        basisfilename5='boundary_'
        %dlmwrite([pathname_results basisfilename sprintf('%.3d',i) basisfilename5,↙
```

22.07.15 16:41 /Users/mariahamme.../RICM_evaluation_md.m   4 of 6

```
num2str(i),'.txt'],result2,'newline','pc','delimiter','\t');

    end

    % save first pixel position of outline for FIJI selection
    if i == 1
        pixel_outlines = ones(10,2);
    end
    px = result2(10,:);
    pixel_outlines(i,:) = px;
        % take 10th entry from boundary and save it in pixel_outlines table
    dlmwrite([pathname_outlines basisfilename, 'pixels.txt'], pixel_outlines,↙
'newline','pc','delimiter','\t');

    % calculate properties of region of regionmatrix L
    stats = regionprops↙
(L,'Centroid','Orientation','Area','Eccentricity','MajorAxisLength','MinorAxisLength',↙
'Perimeter', 'EulerNumber', 'Extrema', 'PixelList','PixelIdxList', 'Image' );

    % loop over the boundaries
    for k = 1:length(B)

    % obtain (X,Y) boundary coordinates corresponding to label 'k'
    boundary = B{k};

    % obtain the area calculation corresponding to label 'k'
    area = stats(k).Area;
    orientation= stats(k).Orientation;
    eccentricity = stats(k).Eccentricity;
    ma_ax_length=stats(k).MajorAxisLength;
    mi_ax_length=stats(k).MinorAxisLength;
    centroid=stats(k).Centroid;
    orientation=stats(k).Orientation;
    perimeter=stats(k).Perimeter;
    eulernumber=stats(k).EulerNumber;
    extrema=stats(k).Extrema;
    pixelList=stats(k).PixelList;  %all pixels within boundary (in xy coordinates)
    linearIndices = stats(k).PixelIdxList;   % all pixels with linear indices

    % Get intensities within boundaries and calculate height

    C=pixelList(:,1);  %write first row of pixelList in C
    R=pixelList(:,2);  %write second row of pixelList in R
    Int=impixel(I,C,R);
        % impixel gets intensity values of original image I for pixels with↙
coordinates from C and R
        % Int has three columns for RGD coding
        % here: just gray values (all entries in same row with same value)
    Int=Int(:,1);
        % - take only first column
    IntM=max(Int);
    Intm=min(Int);
        % get minimum and maximum intensity values
    nw = 1.3321;
        % diffraction index of medium
    lambda = 593;
        % wavelength
    h=(lambda/(4*pi*nw))*acos((2*Int(1:length(Int))-Intm-IntM)/(IntM-Intm));
        % calulate height for each pixel using min and max intensities
    % save pixel coordinates, intensities and heights in one matrix
    M=[C,R,Int,h];
```

22.07.15 16:41 /Users/mariahamme.../RICM_evaluation_md.m 5 of 6

```
    % Calculate the area above a certain threshold 'thresh'
    hmin = 40;
        % set height threshold
    Cth = cos(4*pi*hmin*nw/lambda);
    thresh = (1-Cth)/2*IntM+(1+Cth)/2*Intm;
    %tresh = 0;
    pixels_bigger = 0;

    % create vectors for segmentation indices that are later overwritten
    % take linear indices, otherwise rows or columns are just counted once!
    indicesForSegmentation = zeros(length(linearIndices), 1);
    j = 1;
    s_xy = size(I);
    s_x = s_xy(2);
    s_y = s_xy(1);

    % save all pixel indices with intensity values above thresh in vector
    for v = linearIndices'
        if I(v) > thresh
            pixels_bigger = pixels_bigger + 1;
            indicesForSegmentation(j) = v;
            j = j + 1;
        end
    end

    % remove zero-values indices
    indicesForSegmentation = indicesForSegmentation(find(indicesForSegmentation > 0));
        % create vector with only non-zero-values indices
    I_seg = zeros(s_y, s_x);
        % create matrix with same size as image
    I_seg(:) = 100;
        % fill matrix with grey values
    I_seg(linearIndices) = 0;
        % fill matrix on linear indices position of outline with black color
    I_seg(indicesForSegmentation) = 255;
        % fill matrix on linear indices position of segmentation with white
    I_seg = uint8(I_seg);
        % converts matrix to 8bit image

    %figure (12), imshow(I_seg), title('Pixels higher than threshold');

    assignin('base', 'biggerPixelsPercent', pixels_bigger/area*100);
        % percent of pixels higher than tresh is calculated and saved in
        % biggerPixelsPercent

    % save threshold image in results file
    basisfilename4= 'tresh_'
    imwrite(I_seg,[pathname_results basisfilename basisfilename4,sprintf('%.3d',i),'.↙
tif']);

    % save results
    result=[i, area, centroid, orientation, eccentricity, ma_ax_length, mi_ax_length,↙
fudgeFactor, perimeter, eulernumber,IntM,Intm, pixels_bigger, biggerPixelsPercent];
        % write parameters to vector
    results_tab(i,:) = result;
        % append vector to matrix


    colnames =  {'Number  ' '   Area   ' '  Centroid1    ' '  Centroid2    ' '↙
Orientation    '  '   Eccentricity   ' '   MajorAxisLength    ' '   MinorAxisLength' '↙
FudgeFactor    ' '  Perimeter     '  '   EulerNumber    '  '   MaxInt    ' '   MinInt    '↙
```

22.07.15 16:41 /Users/mariahamme.../RICM_evaluation_md.m 6 of 6

```
' PixelsBigger' '   BiggerPixelsPercent'};
    colnames_txt = sprintf('%s\t',colnames{:});
        % define column names of matrix and convert them into tab-seperated
        % strings
    colnames_txt(end) ='';
    dlmwrite(nametxt, colnames_txt, '');
    dlmwrite(nametxt, results_tab, 'newline', 'pc', '-append', 'delimiter', '\t');

    % save Matrix M (pixel XY position with intensities and calculated height)
    pixel_height=[M];
    dlmwrite(nametxt2,pixel_height,'newline', 'pc', '-append','delimiter', '\t');


    end



   % create surface plot
    Lc = L;
    Li = L;
        % copy matrix L
    [m,n] = size(M);
        % get matrix dimensions [rows, columns]

    for z = 1:m
        %xv = M(z,1);
        %yv = M(z,2);
        Lc(M(z,2),M(z,1))= M(z,4);
        Li(M(z,2),M(z,1))= M(z,3);
    end
        % replace 1-values with height values from matrix M

    Lc = Lc(min(M(:,2)):max(M(:,2)),min(M(:,1)):max(M(:,1)));
    Li = Li(min(M(:,2)):max(M(:,2)),min(M(:,1)):max(M(:,1)));
        % cut off matrix from maximum to minimum xy-positions

    matrix_height=[Lc];
    dlmwrite(nametxt3,matrix_height,'newline', 'pc', '-append','delimiter', '\t');

    matrix_intensities=[Li];
    dlmwrite(nametxt4,matrix_intensities,'newline', 'pc', '-append','delimiter',↙
'\t');

    % create topography image

    I_topo = zeros(s_y, s_x);
        % create matrix with same size as image
    I_topo(:) = 100;
        % fill matrix with grey values
    for t =1:m
        I_topo(M(t,2),M(t,1)) = M(t,3);
        % go through matrix M
        % replace value in I_topo with grey value if in matrix M
    end

    I_topo = uint8(I_topo);
    % figure(14), imshow(I_topo), title('topology');
    basisfilename6 = 'topology_';
    imwrite(I_topo,[pathname_fraclac basisfilename basisfilename6,sprintf('%.3d',i),'.↙
tif']);
```

b) *Overview T cell subpopulations*

For each experiment, mean values between naïve (Tn), central memory (Tcm) and effector memory (Tem) T cells are compared and the p-value was determined with Mann-Whitney-U-Test

donor	donation day	subpopulation comparison	Df of contour	Df of contour/topology	area [µm^2]	eccentricity	adhesive area [%]	circularity	excess perimeter [µm]
donor A	day before	Tn -> Tcm	↓ 0.74424135	↓ 0.0270712	↓ 0.00000018	↓ 0.0034585	↓ 0.00000105	↑ 0.22615833	↓ 0.00181282
		Tn -> Tem	↑ 0.25049631	↓ 0.82036002	↓ 0.16777014	↓ 0.48971929	↓ 0.03057019	↓ 0.57975302	↓ 0.39231959
		Tem -> Tcm	↓ 0.10627812	↓ 0.07538344	↓ 0.00008335	↓ 0.01034374	↓ 0.00021728	↑ 0.06411456	↓ 0.0082044
donor B	day before	Tn -> Tcm	↓ 0.8419152	↑ 0.00007323	↑ 0.00000059	↑ 0.00000596	↑ 0.00000001	↓ 0.30015149	↑ 0.00378274
		Tn -> Tem	↑ 0.45290319	↑ 0.00000102	↑ 0.00000028	↑ 0.02206	↑ 0.00322727	↓ 0.16104597	↑ 0.00002574
		Tem -> Tcm	↓ 0.25819973	↓ 0.00510713	↓ 0.77888784	↑ 0.01706092	↑ 0.0000055	↑ 0.73874562	↓ 0.51274868
donor C	fresh	Tn -> Tcm	↓ 0.95804958	↓ 0.80485641	↓ 0.21210221	↓ 0.02841743	↓ 0.05979642	↑ 0.29014108	↓ 0.09860956
		Tn -> Tem	↓ 0.07871914	↑ 0.94348226	↑ 0.00165602	↓ 0.06697477	↑ 0.44028354	↑ 0.022829	↑ 0.87763582
		Tem -> Tcm	↑ 0.05029519	↓ 0.60084419	↓ 0.00000004	↓ 0.36300027	↓ 0.00049802	↓ 0.0789043	↓ 0.01092788
donor D	fresh	Tn -> Tcm	↓ 0.72321313	↓ 0.4380958	↓ 0.27302412	↑ 0.49735594	↓ 0.64556953	↓ 0.91446227	↓ 0.85183528
		Tn -> Tem	↑ 0.70637974	↓ 0.86644642	↑ 0.85688408	↓ 0.28091922	↑ 0.11128155	↑ 0.46605861	↑ 0.89901763
		Tem -> Tcm	↓ 0.71322525	↓ 0.56858098	↓ 0.08428579	↑ 0.12378027	↓ 0.06416296	↓ 0.71099266	↓ 0.51288747
donor E	day before	Tn -> Tcm	↑ 0.41856181	↑ 0.5648445	↑ 0.00001072	↓ 0.72247083	↑ 0.24591954	↓ 0.2273159	↑ 0.01100198
		Tn -> Tem	↑ 0.02989356	↑ 0.21537091	↑ 0,000000	↑ 0.08528518	↑ 0.01985207	↓ 0.01141306	↑ 0.0000005
		Tem -> Tcm	↓ 0.25539315	↓ 0.63116235	↓ 0.06884155	↓ 0.06333833	↓ 0.7454987	↑ 0.1849576	↓ 0.02732268
donor F	day before	Tn -> Tcm	↑ 0.59248442	↑ 0.00892082	↑ 0.03159758	↑ 0.77435673	↓ 0.25197516	↓ 0.58007786	↑ 0.13907302
		Tn -> Tem	↑ 0.93030054	↑ 0.00011465	↑ 0.00009418	↓ 0.33016541	↓ 0.33160779	↑ 0.76808553	↑ 0.21620126
		Tem -> Tcm	↑ 0.52441077	↓ 0.10260719	↓ 0.03153087	↑ 0.1363288	↓ 0.86389653	↓ 0.26170483	↓ 0.98650052